Studies on the Efficiency and Durability Control of Quasi-2D Perovskite Light-Emitting Diodes and Related Mechanisms

程, 泰

2020

Doctoral Thesis

Studies on the Efficiency and Durability Control of Quasi-2D Perovskite Light-Emitting Diodes and Related Mechanisms

Tai Cheng

Department of Chemistry and Biochemistry

Graduate School of Engineering

Kyushu University

Table of Contents

Chapter 1

Introduction

In recent several years, the fields of optoelectronics and material science have witnessed the remarkable development of metal halide perovskites. Metal halide perovskites exhibited excellent device performances in solar cells and field-effect transistors.[1–6] Since the first solar cells with the $CH_3NH_3PbI_3$ ($MAPbI_3$) perovskite as the light absorber were reported by Miyasaka et al.,[7] power conversion efficiencies of perovskite solar cells have rapidly increased from 3.8% to over 25%,[8] because of great efforts of optimizing perovskite film morphologies and device architectures. The efficiency of 25% is comparable to those of other semiconductor solar cells, such as solar cells based on copper indium gallium selenium, gallium arsenide, cadmium telluride, and silicon.[9] The fast progress on perovskite solar cells triggered a research boom and also attracted a lot of attention and resources from global energy companies. Since that, in the fields of light emission,[10] photoelectric detection,[11] X-ray detection imaging,[12] and so on, researchers also began to explore the application of perovskites.

These significant achievements can be attributed to the excellent optoelectronic properties of perovskites. These properties include the high absorption coefficient, the relative benign internal defects, the long carrier diffusion length, the bipolar charge transport ability, the narrow width of the luminescence spectra, and etc. Therefore, the performances of halide perovskite devices can be rapidly improved, forming a prospect that they can replace the existing mature technologies. There are many types of halide perovskite materials, with adjustable bandgaps and adjustable functions, and their applications need more exploration.

The application of perovskites on light emitting was inspired from their potential of high emitting efficiencies in electroluminescence (EL) process. The triplet excitons, which are a limit factor on the emitting efficiency in organic light-emitting diodes (OLEDs), do not restrict the emitting efficiency of perovskite light emitting diodes (PeLEDs). Besides, the bandgaps of perovskites can be continuously tuned by changing compositions, especially halogen atoms. In 2014, Tan et al. first demonstrated room temperature green and red EL from $MAPbBr_3$ and

$MAPbI_{3-x}Cl_x$ PeLEDs.[10] Since then, consistent researches have been done to expand the range of emitting colors, as well as to modify the perovskite crystallinity and device architectures to improve the LED performances. As a result, multicolor emissions covering a full visible spectral region[13] have been developed. Recent reports have demonstrated green, red, and near-infrared PeLEDs with external quantum efficiencies (EQEs) surpassing 20%,[14–18] rendering the performances comparable to those of organic or quantum-dot LEDs. Moreover, perovskites exhibit outstanding performance as the charge transport layers in OLEDs.[19]

Even though high-performing PeLEDs have been demonstrated, a better understanding of their operational mechanisms behind has been required for future practical applications such as displays and lighting.

1.1 Metal Halide Perovskite Materials

1.1.1 Crystalline Structures

General perovskite solid is well known for its crystal structure of an extended network of PbX_6 octahedra intercalated with organic ammonium (or Cs) cations to keep the charge neutrality (Figure 1-1a). Typical metal halide "3D" perovskites have a chemical formula of ABX_3, where A represents the organic or Cs cation that fits in the cavity delimited by the corner-sharing octahedra, B represents the metal cation, and X represents the halogen anion. Simple perovskites have a cubic close-packed lattice. The close-packed layer is parallel to the (111) crystal plane and is composed of A^+ and X^-. The B ions are filled in the voids between octahedra formed in two closely packed layers of X^-. Therefore, an A^+ has 12 X ions to coordinate with, and a B ion have 6 X ions to coordinate with. It can be seen from the structure of the perovskite lattice that A^+ participates in close packing, which is very important for stabilizing the perovskite structure. Since B ions are filled in the voids, the requirements for their radius and

valence state are not strict, and there are a variety of selections. However, experience exhibits that B ions are usually important elements that determine many physical properties of perovskite materials. Perovskites that currently exhibit excellent performances in optoelectronic devices usually have lead ion as the B ion.

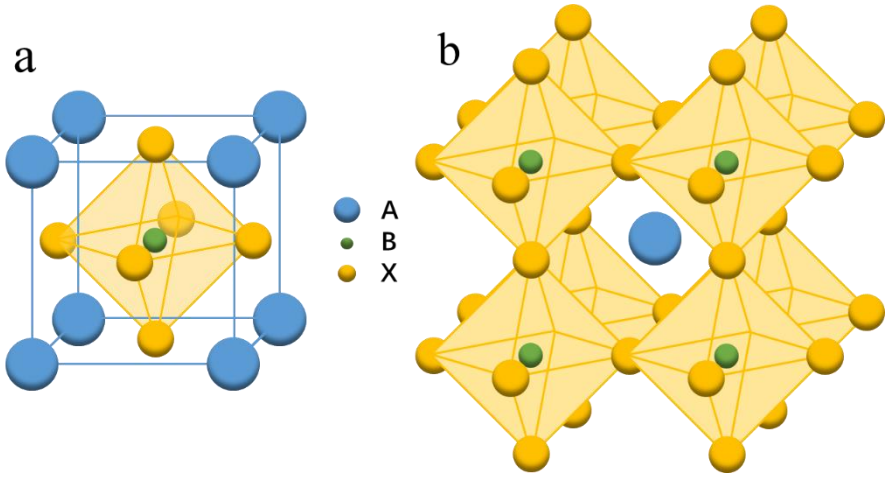

Figure 1-1. (a) Unit cell of a typical perovskite lattice. (b) Perovskite crystal structure in the term of corner-sharing octahedra.

There is another description of the perovskite lattice (Figure 1-1b). According to the description of the unit cell, a B^{2+} and 6 X^- form an octahedral coordination unit of BX_6. The alignment of BX_6 octahedra sharing X^- apexes forms the framework of the perovskite lattice, and A ions are filled in the voids formed by the above arrangement. The perovskite crystal structure is characterized by repeating BX_6 octahedral units. Some non-ABX_3 structural materials with this feature are also called perovskites.[20]

In order to obtain a stable and photoelectrically active perovskite phase, the radius of A^+ has a certain range, which can be judged by a tolerance factor *t*:[21]

$$t = \frac{r_A + r_X}{\sqrt{2}(r_B + r_X)} \qquad (1-1)$$

Experience has shown that the radius of A^+ must meet $0.8 < t < 1.0$,[9] otherwise the lattice distortion will cause a phase transfer. Taking $APbI_3$ perovskites as an example, only limited sorts of A^+ support $APbI_3$ perovskites to obtain photoelectric activity,[9] as shown in Figure 1-2.

The sodium, potassium, and rubidium ions are too small, and the organic ions such as imidazole, ethylamine, and guanidine ions are too large, inducing that they do not meet the requirements of the tolerance factor. Even the perovskite lattices of $FAPbI_3$ ($t \approx 1$) and $CsPbI_3$ ($t \approx 0.8$) are easily distorted, but they can be stabilized by multi-ion mixing.

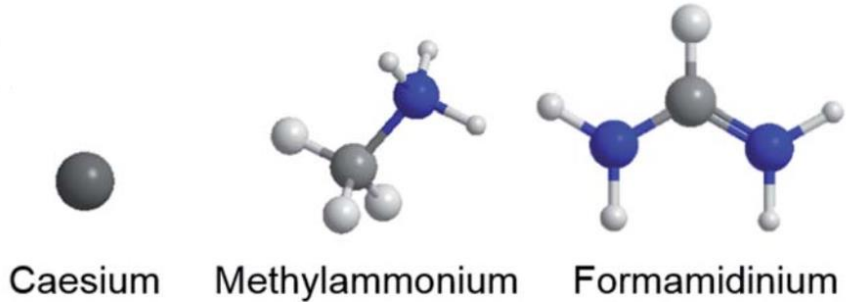

Figure 1-2. Cesium (Cs), methylammonium (MA), and formamidinium (FA) ions. Blue, dark gray, and light gray spheres are nitrogen, carbon, and hydrogen atoms, respectively. This figure is reproduced from ref. 22.

At present, the lead halide perovskites have the highest photoelectric conversion efficiencies in devices. But lead-free perovskites avoiding using toxic lead and all-inorganic perovskites with better stability are also hot research spots. Among the halide perovskite materials, there is also a sub-category of quasi-2D perovskites that have received much attention in luminescence applications. The quasi-2D perovskites inherit and expand the excellent properties of the three-dimensional halide perovskites. Quasi-2D perovskites have higher emission efficiency, thanks to their self-organizing quantum well structures. In this thesis, the quasi-2D perovskites will be introduced in detail in the section 1.2.2.

1.1.2 Optical and Electronic Properties

Many methods have been developed for the preparation of halide perovskite thin films.[23] The solution deposition methods are most commonly used. Perovskite films can be prepared from a simple precursor ion solution by spin-coating and follow-up annealing, or they can be prepared from a nanocrystal colloid solution readily synthesized from a solution chemical reaction.[24]

Halide perovskites are direct bandgap semiconductors with good photoelectric properties. Since halogen is a group of elements with strong electronegativity, halide perovskite crystals have many ionic bonds, which is similar to the II-VI compound semiconductors. At the same time, halide perovskite materials are also a kind of semiconductors that can be processed at low temperature. The bandgaps of halide perovskite semiconductors are in the range of visible light to near infrared light, and they can be adjusted by the chemical composition. Holes and electrons generated in perovskites are mostly excited or injected externally, which is similar to the case in organic semiconductors. Solution processed perovskite films have high carrier mobilities (greater than 20 $cm^2\ V^{-1}\ s^{-1}$)[25] and large diffusion lengths (greater than 1 μm)[26]. The carrier lifetimes of halide perovskite materials are generally in the range of hundreds of nanoseconds to one microsecond, which is much smaller than the tens of milliseconds of silicon.[9] In order to improve the performances of photovoltaic and emission devices, carrier loss by non-radiative recombination should be suppressed.

The intrinsic point defect states of halide perovskites are generally very close to the conduction band and the valence band (which is determined by the bonding properties). These defect states are shallow traps for carriers and thus are not particularly harmful for most of the properties of perovskites, which is described as the insensitivity to intrinsic defects. However, the defects on the grain boundaries of halide perovskites can work as efficient non-radiative recombination centers. Larger grain size, with micrometer size being possible, should be helpful for suppressing this sort of non-radiative recombination. The energy loss on the grain boundaries was proved smaller than that of other polycrystalline solar cell materials.[27]

The photoluminescence quantum yield (PLQY) was found to be limited by the effect of carrier or exciton trapping by grain-boundary defects at low excitation intensities.[10] At high excitation intensities or at low temperatures, these trap states are easier to fulfill, and photo-generated carriers/excitons recombine mainly through the radiative process. Both theory and

experiments exhibit that the PLQYs of halide perovskites can approach 100% at high excitation intensities or low temperatures. Therefore, the application of halide perovskites to emitting devices usually involves the study of removing or filling[28] the trap states in order to obtain high emission efficiencies even at a lower excitation intensities or at room temperature. Methods to fill the trap states are called "passivation".

Previous researchers have made accurate and direct measurements of the exciton binding energy (E_B) of halide perovskites. Some perovskites have an E_B of only 16 meV at low temperature, which further drops to 5 meV at room temperature, while the effective exciton mass is only 0.1 m_e (m_e is the electron mass).[29] Therefore, at room temperature, the free carrier behavior dominates in halide perovskites, which explains the excellent device performances of perovskite solar cells.

An inherent disadvantage of halide perovskite materials is the ion migration. Many direct or indirect experiments proved that ion migration is the source or important factor of many unusual phenomena in halide perovskite materials and their devices, such as photocurrent hysteresis, photo-induced giant dielectric constant, photo-induced phase separation, and a rapid decline of device performances.[27,30] Thankfully, the ion migration mainly occurs through the grain boundaries, and is mainly based on the migration of A^+ ions such as MA^+.[27] If the ion migration in a bulk perovskite is also serious, the modified perovskite structure may take away its wonderful photoelectric properties. However, the ion migration properties also make the halide perovskites possible as lithium storage materials in batteries.[30]

1.2 Quasi-2D Perovskite

1.2.1 Quantum Confinement Effect

E_B is an important parameter that characterizes the property of excitons and refers to the

energy required for excitons to return to free electrons and holes. E_B is generally tens to hundreds of eV. Because the strong dielectric screening effect in halide perovskite materials weakens the Coulombic interaction of the electron-hole pair, E_B in perovskites is relatively small. This phenomenon is particularly obvious for I-based perovskites, since they typically have low E_B of no more than 20 meV[31] and exhibit no excitonic character under room temperature.

This very low E_B[32,33] results in slow bi-molecular recombination and long charge-carrier diffusion.[34,35] Also, as mentioned above, when the grain size of a perovskite film is large, the recombination sites and traps of the carriers are fewer, the mobility is excellent, and the carriers are free at room temperature. These features render 3D perovskites excellent materials for photovoltaic applications, which requires charge carrier-pair separation. However, in emitting devices, the low E_B makes obtaining efficient photoluminescence (PL) and EL difficult since the slow radiative recombination may be susceptible to trap-assisted quenching. Also, the excellent mobility increases the probability of non-radiative defect sites to capture carriers, resulting in an increase in non-radiative recombination rate. Therefore, for emission applications, increasing E_B and reducing exciton diffusion length are necessary for engineering perovskites.[36] An important method to achieve this aim is the utilizing of the quantum confinement effect.

The quantum confinement effect can be described as follows. By reducing the crystal size of various dimensions to the order of the exciton Bohr radius, the electron motion is restricted, resulting in a discontinuous electron energy level structure similar to atoms. The increased semiconductor bandgap and E_B, and decreased exciton diffusion length are the results of this effect. Electrons are easier to form excitons with holes under the limitation of the average free path of small-sized crystals, so the quantum confinement effect is one of the methods to increase the concentration of excitons and thus improve the emission efficiency. As shown in Figure 1-

3, the quantum confinement effect on perovskites can be generated through size reducing in one direction (2D/quasi 2D structure formed), two directions (1D linear structure formed), and three directions (0D dot-like structure formed). Low-dimensional perovskite structures such as polymer-perovskite composites,[16] alumina-pinned nanocrystals,[37] quantum dot colloids[24], and quasi-2D perovskites [also referred to multi-quantum well (MQW) structures] all adopt the idea of this quantum confinement effect.

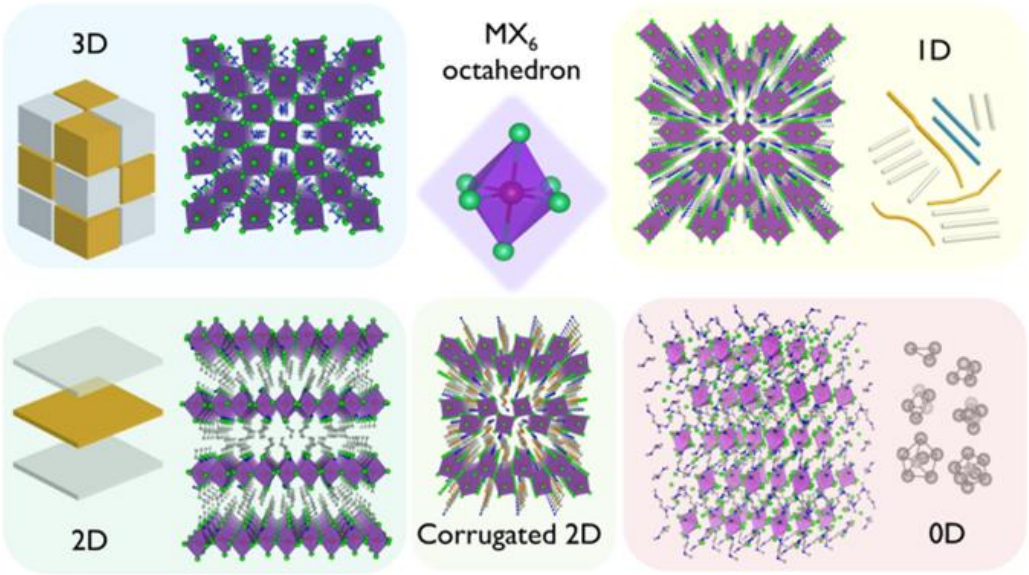

Figure 1-3. Scheme of the structures of 3D and low dimensional perovskites. This figure is reproduced from ref. 38.

1.2.2 Concept and Properties of Quasi-2D Perovskite

The cubic structure of 3D perovskites can be broken in some specific directions to form a low-dimensional material. As shown in Figure 1-4, the direction of these breaks or tears is usually along the (100), (110), and (111) crystal planes of the 3D perovskites (Figure 1-4). Perovskites torn along three directions have different chemical formulas and different properties.[39] By introducing large organic cations, the breaks along the (100) crystal planes of perovskites are the easiest to form, and most quasi-2D perovskites used for emission and photovoltaic devices are formed through this way, which can always be confirmed by a strong

characteristic peak of the (100) crystal plane in X-ray diffraction (XRD) patterns. The 2D and quasi-2D perovskites mentioned in the following contents are from the cuts along (100) direction.

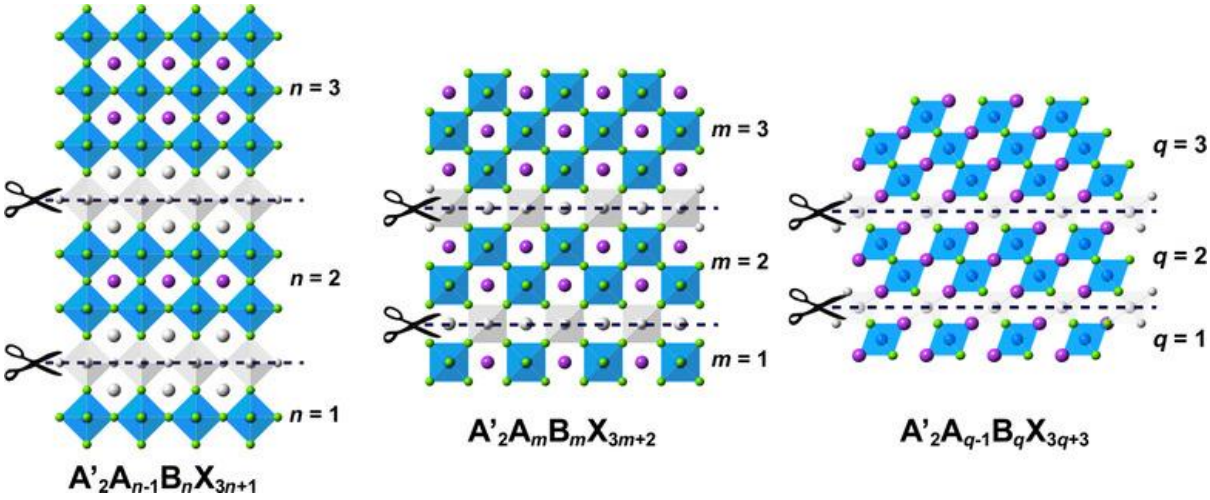

Figure 1-4. Cuts along (100), (110), and (111) directions and the quasi-2D perovskites that result from such cuts. This figure is reproduced from ref. 39.

2D perovskites formed from the (100) cuts are described with the formula L_2PbX_4, where L^+ is the large organic ammonium cation oversized to fit in the cavity formed by corner sharing PbX_6 octahedra, making the 3D perovskites collapse into PbX_6 tabs (n = 1 case in Figure 1-5). There are so-called quasi-2D perovskite configurations between 2D and 3D structures, with the formula of $L_2A_{n-1}Pb_nX_{3n+1}$ (Figure 1-5). The large organic cations divide the perovskite crystals into two-dimensional platelets of different thicknesses and intercalate between layers to act as spacers. Here, n represents the number of stacked PbX_6 sheets (the **order** of quasi-2D perovskites) in one platelet. For example, n = 1 platelets (belonging to the n = 1 domain) contain one layer of PbX_6 octahedra, n = 2 platelets (belonging to the n = 2 domain) contain two layers of PbX_6 octahedra, and so on. Accordingly, the $n = \infty$ platelets correspond to 3D perovskite crystals. The large organic cations interact with the surface of the platelets through ionic bonds, and the stacking between the platelets depends on the van der Waals force between the large organic cations. If the organic spacer cation has a π system, the π interaction also becomes a

binding force. A group of platelets with the same thickness is of a single phase. Generally, the prepared quasi-2D perovskite films contain many domains with various phases (various *n*).

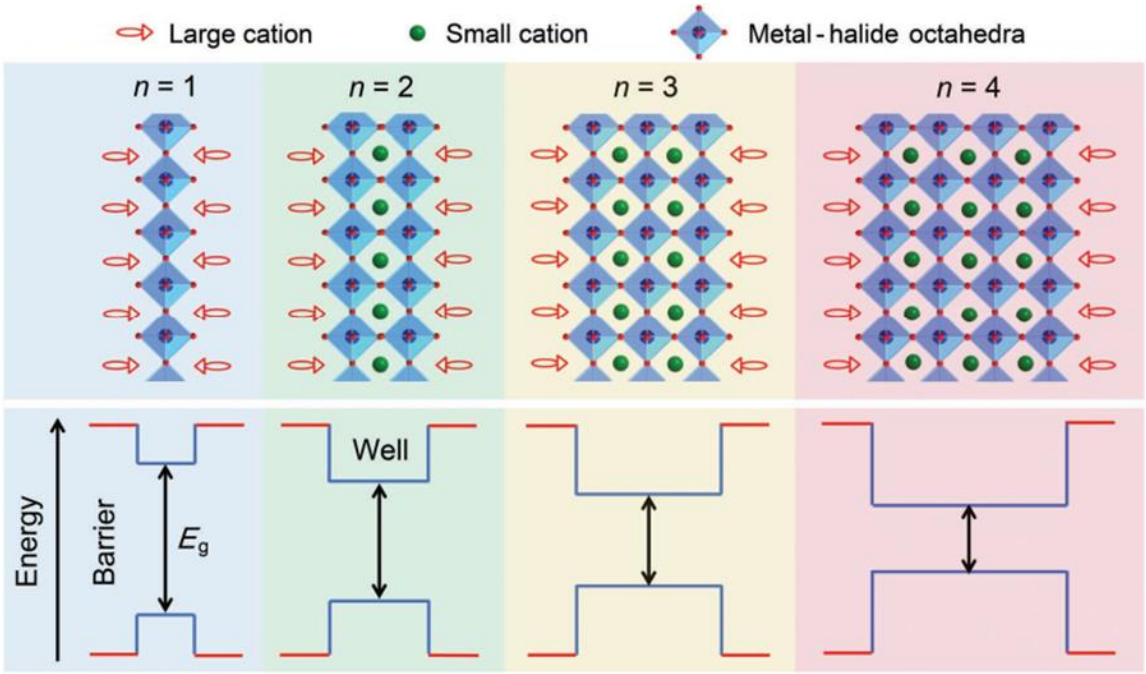

Figure 1-5. Diagrams of quasi-2D perovskite phases with various *n* and the energy level structures of the quantum wells. This figure is reproduced from ref. 13.

The quasi-2D perovskites formed with L^+ cations are referred as the Ruddlesden–Popper (RP) type. Besides, quasi-2D perovskites were also reported formed with L^{2+} cations, referred as the Dion-Jacobson (DJ) type (Figure 1-6).[39] The DJ type avoids the van der Waals force between two adjacent L^+ in the RP type. In this way, DJ type should have better structural stability on a lattice level, but also requires higher formation energy.

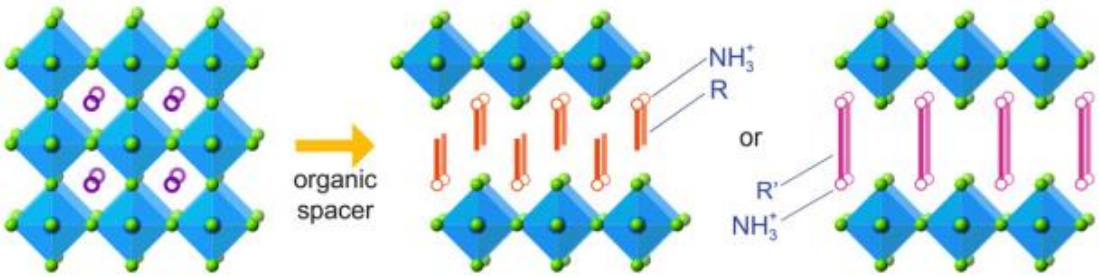

Figure 1-6. Crystal structures of a 3D perovskite (left), a RP-type 2D perovskite (middle), and a DJ-type 2D perovskite (right). This figure is reproduced from ref. 39.

By adjusting the ratio between large space cations and small cations, the thickness of the generated platelets can be controlled to a certain extent. However, besides some low-*n* domains, generating pure phases is still a very challenging topic.[40] In most cases, there is no necessity to obtain a pure phase, and adjusting the domain distribution is sufficient.

Generally, the layered structures of 2D and quasi-2D perovskites can be considered as natural quantum-well structures (Figure 1-5). The inorganic layers act as "wells" and the organic cations as "barriers", which are supposed to induce strongly bound excitons and intense PL. This is because of the much higher dielectric constants and narrower bandgaps of the PL "well" layers than the "barrier" layers, for mostly used L cations of aliphatic or aromatic substituents (Figure 1-7a).[41,42] With a decrease of n from ∞ to 1, both the dielectric and quantum confinements arise, resulting in significantly enhanced E_B (Figure 1-7b)[43], larger bandgap, narrower PL emission, and smaller Stokes shift.[44] In general, the difference between the bandgaps of $n = 1$ and $n = 2$ domains is the largest. As n increases, the bandgap difference of domains with different n becomes smaller and smaller. Every domain in films has a quantum well structure, meaning that quasi-2D perovskite films correspond to a multi-quantum well structure. From a macro perspective, in quasi-2D perovskite films, the wide bandgap domains can act as carrier confinement domains, while the small bandgap domains are responsible for the radiative recombination.

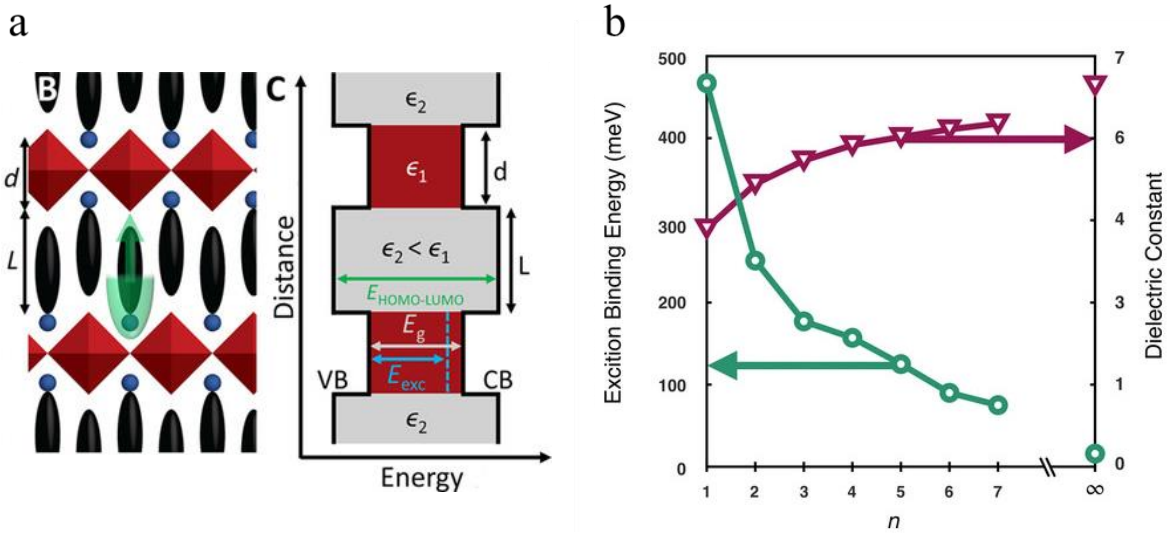

Figure 1-7 (a) Scheme of dielectric confinement in 2D perovskites. (b) E_B and the high frequency dielectric constant of the $(BA)_2(MA)_nPb_nI_{3n+1}$ perovskites with various *n*, where the BA is benzylammonium. This figure is reproduced from ref. 39.

The quasi-2D perovskites inherit and expand the excellent properties of the 3D perovskites,[40] such as direct bandgap nature, high absorption coefficients, and small effective masses of electrons and holes. This extends the functional adjustment approaches of perovskites. Besides being used as the effective light-absorbing material for solar cells,[39] quasi-2D perovskites exhibit efficient PL at room temperature, indicating that a large density of stable excitons can be generated with higher E_B at room temperature, making the radiative recombination from excitons dominant.[13]

1.3 LEDs Based on Quasi-2D Perovskites

1.3.1 Electroluminescence from Metal Halide Perovskites

As a solid-state lighting technology, LED is based on semiconductors which convert electrical energy into light. As a new generation of light source, LEDs have been widely used in various fields of modern society, including daily civilian lighting, industrial lighting, medical equipment, and etc.[45] With the advent of the information age, LED technology has shown strong

vitality in the display field in recent decades,[46] driving the rapid development of the LED industry.

In order to obtain a more convenient and comfortable life, people's demand for display devices is also increasing. This puts more and more stringent requirements on the power consumption, brightness, color saturation (wide color gamut), resolution, thinness, and flexibility of LED devices. In LEDs, traditional III-V or II-VI inorganic semiconductor materials are mainly prepared by crystallization or epitaxial growth on rigid substrates such as sapphire or silicon, and it is not easy to form smaller light-emitting units (pixels) with these materials. OLED materials can be formed on a rigid or flexible substrate by evaporation or solution processing, and it is easier to prepare high-resolution, thin, and flexible LED devices. After the development of more than 30 years, OLED technology has become one of the most advanced display technologies at present and is still evolving. In the field of light sources, OLEDs can be used as a true surface light source to provide soft diffuse light. In some application scenarios OLEDs have significant advantages over inorganic LEDs.[47]

However, it is also necessary to achieve the largest possible display color gamut to achieve a high saturation, vivid, and natural display effect. This requires the red, green, and blue (RGB) display units of the LED display device to achieve as narrow emission spectra as possible. However, general OLED materials have PL peaks of large full widths at half maximum (FWHM) of over 40 nm.[48] This is particularly notable in the high-efficiency thermally activated delayed fluorescence (TADF)-based OLEDs At the same time, the synthesis cost of OLED materials is relatively high, and a large part of them still rely on vacuum evaporation technology to form films. This leads to higher production cost of OLEDs.[46]

Inorganic quantum dot LED (QLED) and PeLEDs have become important candidates for new LED display. They can reach the FWHM of PL and EL below 25 nm, and both support the low-temperature solution processes for film formation. However, the grain size of inorganic

quantum dots has a great influence on the position of its emission spectrum. In order to achieve a narrow emission peak, the particle size distribution of quantum dots must be very concentrated. Together with the requirements for dispersibility and stability, the production process of quantum dot colloid solutions is still expensive.[49] In contrast, the exciton Bohr radius of perovskite materials is generally very small (below 3 nm),[50] so the requirements for particle size are not strict. Because of the existence of long-chain organic ligands, quantum dots generally have the problem of inefficient charge transport. At this point, perovskite's excellent carrier mobilities also became an advantage. In summary, perovskites are a strong competitor for the new-generation of LED luminescent materials.

Back in 1994, Saito et al. from Kyushu University pioneered the LED devices with the perovskite emitter.[51] However, because of the low E_B of the perovskite materials at that time, the PeLED devices only emitted light normally under liquid nitrogen temperature. Because of the low efficiency of the devices and the strict working conditions, this work did not attract much attention at that time, and there have been few reports on this field in following 20 years. In 2014, there was a new breakthrough in the research of PeLEDs. For the first time, Tan et al. demonstrated PeLEDs performing EL at room temperature and obtained devices with brightness greater than 100 cd/m^2, and EQEs of about 0.1%.[10] This new breakthrough ignited people's enthusiasm for perovskites as luminescent materials. After that, researchers improved the performances of PeLEDs through various methods. Recent reports have demonstrated green, red, and near-infrared PeLEDs with EQEs surpassing 20%,[14–18] rendering the performances comparable to those of OLEDs or QLEDs.

1.3.2 Progresses on Quasi-2D Perovskites LEDs

With the theoretically high E_B and PLQY under room temperature because of the quantum well structures, researches on quasi-2D perovskite-based PeLEDs started from 2016.

In 2016, Sargent et al. firstly developed quasi-2D PeLEDs showing near infrared (NIR) emission (Figure 1-8).[36] The quasi-2D perovskite structure with the formula of $PEA_2(MA)_{n-1}Pb_nI_{3n+1}$ (where PEA^+ is phenylethyl ammonium cation) dramatically increased the E_B of iodine-based perovskites, resulting in a high EQE of 8.8%, which was the highest value among PeLED reported at that time. In this report, some basic principles of quasi-2D PeLEDs that following researchers always referred to were discovered, such as multi-domain configuration (Figure 1-8c and 1-8d), energy funneling (Figure 1-8e), dependence of PLQY on excitation fluence, and etc. Tuned bandgaps by *n* was evidenced by steady-state PL (Figure 1-8a), and the charge/ energy transfer process between domains was confirmed by transient absorbance spectra (Figure 1-8b) for the first time.

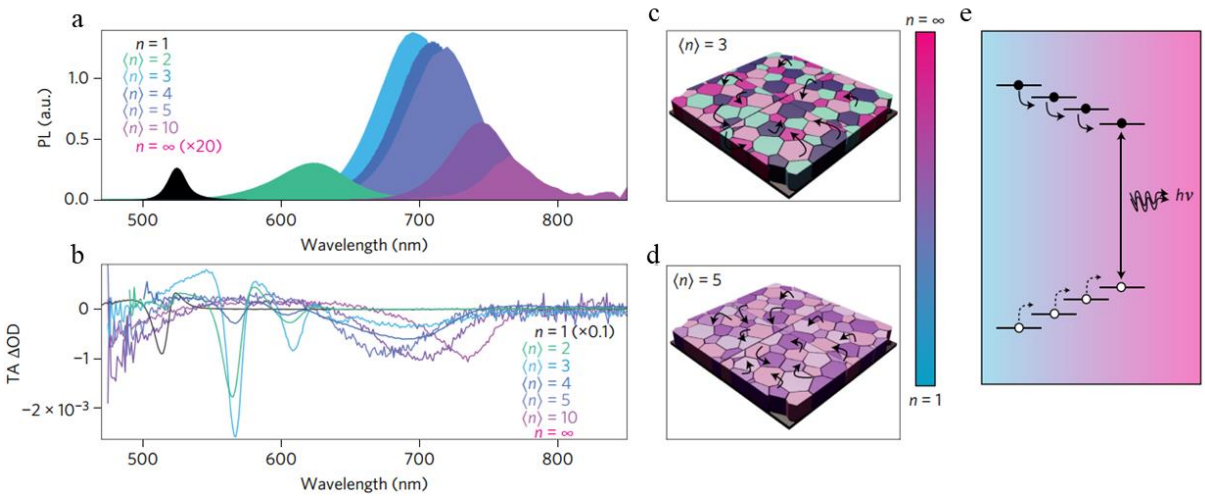

Figure 1-8. Photophysics of perovskites in ref. 36. (a) Steady-state PL spectra for perovskites. The gradually blue-shifted peak position with reduced recipe *n* value indicates the increased quantum confinement effect. (b) Transient absorbance spectra for perovskites with different recipe *n* values. The multiple bleach peaks on one spectrum indicate the excitons from domains with multi-*n* configuration. (c) Carrier transfer process between multi-*n* domains in (c) $n = 3$ and (d) $n = 5$ perovskites. (e) Carrier funneling in a quasi-2D perovskite. This figure is reproduced from ref. 36.

The excellent performance of the first quasi-2D PeLEDs attracted the attention of more researchers. W. Huang et al. then raised the EQEs of NIR PeLEDs with the quasi-2D perovskite emitter to 11.7 %.[52] In following research works, Sargent's team and Huang's team deeply studied the formation process and optoelectronic mechanisms of the quasi-2D perovskite

emitter. W. Huang et al. investigated the exciton behavior in multi-domain quasi-2D perovskites in detail, and deduced the rates of different exciton releasing processes, including trap-assisted quenching, bi-molecular radiative recombination, excitonic radiative recombination, Auger recombination, energy transfer, and etc.[35] Sargent et al. analyzed the formation mechanism of a quasi-2D perovskite, and found that the intermediate compounds produced by the combination of the precursor and the solvent would serve as a "scaffold" for crystal growth. The stoichiometric ratio of large organic cations to intermediate compounds was found to have an important effect on the phase distribution.[53]

Besides using a precursor solution with perfect stoichiometry of the ideal quasi-2D structure, i.e., the formula of $L_2A_{n-1}Pb_nX_{3n+1}$, quasi-2D perovskites can also be obtained by simply mixing two solutions of LX (halide salt of large organic cation) and $APbX_3$ (3D perovskite). B. Rand et al. first adopted this strategy and prepared red and green PeLEDs with EQEs of 10.4% and 9.3%, respectively.[54] The quasi-2D perovskite film using this strategy contains a large number of crystallites with LX as the ligand and has good defect passivation and low roughness. Also, with this strategy, B. Sun et al. fabricated green quasi-2D PeLEDs with an EQE of 15.5 %. By adding crown ether to the precursor solution, they avoided the aggregation and crystallization of LX and tuned the domain distribution.[55]

As the key to form quasi-2D structures, the large organic cations of different sorts have large influence on the properties of perovskites. B. Rand et al. analyzed the defect passivation effect with various L^+, and discovered the influence of the chain length and steric hindrance of L^+ to the perovskite structure.[56] Recently, it was discovered in our laboratory that the energy levels of the triplet excitons of L^+ have much effect on the perovskite emitting process (Figure 1-9). Efficient triplet–triplet Dexter energy transfer was found from triplet excitons of perovskites to T_1 (the lowest excited triplet state) of NMA^+ (1-naphthylmethylamine cation) because of the low T_1 of NMA^+. However, PEA^+, which has high T_1, would not quench triplet

excitons of perovskites, allowing for full utilization of singlets and triplets for efficient emission (Figure 1-9b). It explained why quasi-2D perovskites with similar structural properties but different L cations have distinct emission efficiencies.[57]

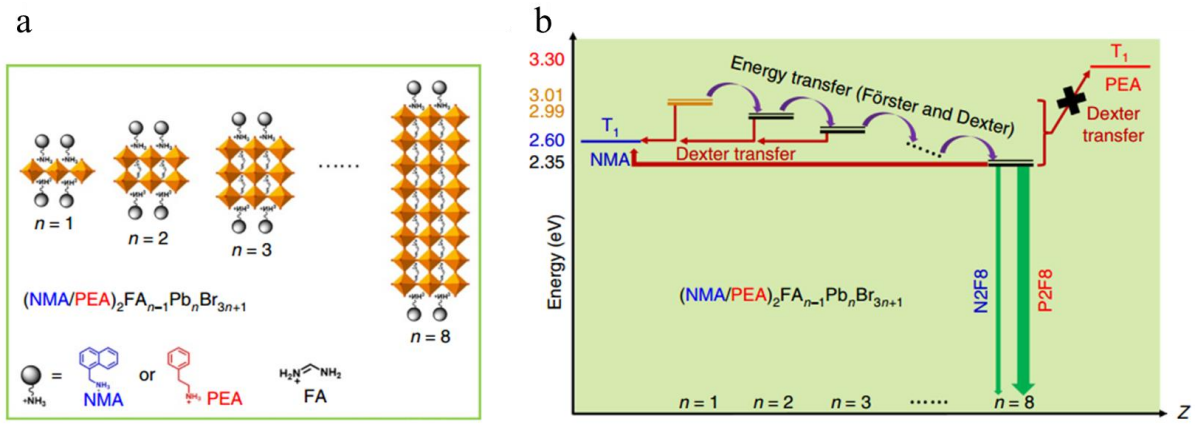

Figure 1-9. (a) Chemical and unit cell structures of quasi-2D perovskites. (b) Proposed energy transfer mechanism considering the triplet energy levels of L^+. This figure is reproduced from ref. 57.

The modifying methods commonly used in 3D perovskites, such as passivation by doping, morphology control, crystallization control, and etc., are still applicable in quasi-2D perovskites. With sufficient optimizing with the approaches mentioned above, the EQEs of quasi-2D PeLEDs have achieved 20.1, 15.5, 11.7, and 5.7% for infrared, green, sky blue, and blue emissions, respectively.[16,55,58,59]

1.3.3 Open Issues on Quasi-2D Perovskite LEDs

Despite the attractive performance in PeLEDs, there are still unclear issues about the film formation, emission mechanisms, and device performances. By now, how the structural factors of quasi-2D perovskite films affect the emission properties remains controversial. Solution-processed quasi-2D perovskite films always contain domains with various *n* and thus various bandgaps, as shown in Figure 1-10a,[36] which should be a result of different reaction speeds between PbX_2 and SX or LX.[54] In such quasi-2D systems, it is known that the energy[36] and

charge[60] transfer occur between domains, which results in exciton confinement within high-*n* domains, as shown in Figure 1-10b, which is the energy funneling effect mentioned above. However, in other cases, it was reported that the energy transfer can be insufficient between the exciton confining domains with small *n* and the emitting domains with large *n*,[55] which could cause many excitons in the confining domains being quenched through non-radiative pathways and make the order-mixing unfavorable for efficient emission.[61] Furthermore, use of large organic ammonium cations can also passivate defects around domains or grains[62,63] besides forming quasi-2D structures (Figure 1-10c), making the compositional control over perovskites even more complex.

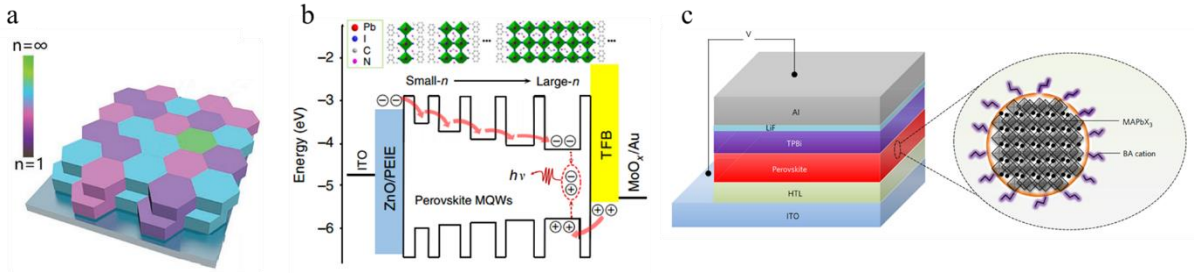

Figure 1-10. (a) Multi-domain structure of a quasi-2D perovskite film.[64] (b) Exciton confinement caused by the energy level funnel effect.[65] (c) Large organic ammonium cations as ligands passivating defect states around grains.[54]

Despite the high PL and EL efficiencies, quasi-2D PeLEDs, especially green- and blue-emitting PeLEDs, still suffer from low operational durability.[13] The device lifetimes of high-efficiency quasi-2D PeLEDs reported so far are only in the timescale of minutes,[55,59,61,66] which seriously impede the practical applications in industry. The factors, such as defect-assisted decomposition[67] and imbalanced charge injection,[68] were found to lower the operational durability. Besides, quasi-2D PeLEDs are also known to have strong EQE roll-off at high current densities.[18,63,65,68] One source of the EQE roll-off is Auger recombination.[65] However, other convincing explanations to understand the PeLEDs' degradation and EQE roll-off would exist, which I found should be the migration of organic cations as introduced in Chapter 3.

Exploring the source of the short working lifetimes and severe roll-off would be meaningful for developing PeLEDs to the demands of industry.

1.4 Aim and Outline of This Thesis

The aim of this thesis is to explore the essential factors impacting the emission efficiencies and working lifetimes of quasi-2D PeLEDs, and the mechanisms of how the aforementioned factors work. I will discuss from the aspects of perovskite forming, exciton and charge carrier behaviors, and ion migration process during device preparation.

Chapter 2 reports the impact of precursor solution engineering on the emitting efficiencies of quasi-2D perovskites. The stoichiometry control over precursors was found effective for the tuning of grain passivation and domain distribution. **Chapter 3** reports the impact of ion migration on the working lifetimes of quasi-2D PeLEDs. The organic cations attached on the perovskite domain boundaries were discovered migrating under the application of external bias. The interaction of the mobile cations with the electron-transporting layer determines the working lifetimes of quasi-2D PeLEDs. **Chapter 4** summarizes this thesis and discuss future perspectives.

1.5 References

(1) Correa-Baena, J.-P.; Abate, A.; Saliba, M.; Tress, W.; Jesper Jacobsson, T.; Grätzel, M.; Hagfeldt, A., *Energ. Environ. Sci.* **2017,** *10*, 710.

(2) Ummadisingu, A.; Steier, L.; Seo, J. Y.; Matsui, T.; Abate, A.; Tress, W.; Gratzel, M., *Nature* **2017,** *545*, 208.

(3) Matsushima, T.; Hwang, S.; Sandanayaka, A. S.; Qin, C.; Terakawa, S.; Fujihara, T., . . . Adachi, C., *Adv. Mater.* **2016,** *28*, 10275.

(4) Yang, R.; Li, R.; Cao, Y.; Wei, Y.; Miao, Y.; Tan, W. L., . . . Huang, W., *Adv. Mater.* **2018,** *30*, e1804771.

(5) Zheng, H.; Liu, G.; Zhu, L.; Ye, J.; Zhang, X.; Alsaedi, A., . . . Dai, S., *Adv. Energy Mater.* **2018,** *8*, 1800051.

(6) Liu, C.; Yang, Y.; Xia, X.; Ding, Y.; Arain, Z.; An, S., . . . Nazeeruddin, M. K., *Adv. Energy Mater.* **2020,** *10*, 1903751.

(7) Kojima, A.; Teshima, K.; Shirai, Y.; Miyasaka, T., *J. Am. Chem. Soc.* **2009,** *131*, 6050.

(8) https://www.nrel.gov/pv/cell-efficiency.html.

(9) Correa-Baena, J. P.; Saliba, M.; Buonassisi, T.; Gratzel, M.; Abate, A.; Tress, W.; Hagfeldt, A., *Science* **2017,** *358*, 739.

(10) Tan, Z. K.; Moghaddam, R. S.; Lai, M. L.; Docampo, P.; Higler, R.; Deschler, F., . . . Friend, R. H., *Nat. Nanotechnol.* **2014,** *9*, 687.

(11) Garc á de Arquer, F. P.; Armin, A.; Meredith, P.; Sargent, E. H., *Nat. Rev. Mater.* **2017,** *2*, 1.

(12) Kim, Y. C.; Kim, K. H.; Son, D. Y.; Jeong, D. N.; Seo, J. Y.; Choi, Y. S., . . . Park, N. G., *Nature* **2017,** *550*, 87.

(13) Cheng, L.; Jiang, T.; Cao, Y.; Yi, C.; Wang, N.; Huang, W.; Wang, J., *Adv. Mater.* **2020,** *32*, e1904163.

(14) Cao, Y.; Wang, N.; Tian, H.; Guo, J.; Wei, Y.; Chen, H., . . . Huang, W., *Nature* **2018,** *562*, 249.

(15) Lin, K.; Xing, J.; Quan, L. N.; de Arquer, F. P. G.; Gong, X.; Lu, J., . . . Wei, Z., *Nature* **2018,** *562*, 245.

(16) Zhao, B.; Bai, S.; Kim, V.; Lamboll, R.; Shivanna, R.; Auras, F., . . . Di, D., *Nat. Photonics* **2018,** *12*, 783.

(17) Xu, W.; Hu, Q.; Bai, S.; Bao, C.; Miao, Y.; Yuan, Z., . . . Gao, F., *Nat. Photonics* **2019,** *13*, 418.

(18) Chiba, T.; Hayashi, Y.; Ebe, H.; Hoshi, K.; Sato, J.; Sato, S., . . . Kido, J., *Nat. Photonics* **2018,** *12*, 681.

(19) Matsushima, T.; Bencheikh, F.; Komino, T.; Leyden, M. R.; Sandanayaka, A. S. D.; Qin, C.; Adachi, C., *Nature* **2019,** *572*, 502.

(20) Yuan, Z.; Zhou, C.; Tian, Y.; Shu, Y.; Messier, J.; Wang, J. C., . . . Ma, B., *Nat. Commun.* **2017,** *8*, 14051.

(21) Ramadass, N., *Mat. Sci. Eng.* **1978,** *36*, 231-239.

(22) Eperon, G. E.; Stranks, S. D.; Menelaou, C.; Johnston, M. B.; Herz, L. M.; Snaith, H. J., *Energ. Environ. Sci.* **2014,** *7*, 982.

(23) Chen, Y.; He, M.; Peng, J.; Sun, Y.; Liang, Z., *Advanced science* **2016,** *3*, 1500392.

(24) Protesescu, L.; Yakunin, S.; Bodnarchuk, M. I.; Krieg, F.; Caputo, R.; Hendon, C. H., . . . Kovalenko, M. V., *Nano Lett.* **2015,** *15*, 3692.

(25) Leijtens, T.; Stranks, S. D.; Eperon, G. E.; Lindblad, R.; Johansson, E. M.; McPherson, I. J., . . . Snaith, H. J., *ACS Nano* **2014,** *8*, 7147.

(26) Stranks, S. D.; Eperon, G. E.; Grancini, G.; Menelaou, C.; Alcocer, M. J.; Leijtens, T., . . . Snaith, H. J., *Science* **2013,** *342*, 341.

(27) Shao, Y.; Fang, Y.; Li, T.; Wang, Q.; Dong, Q.; Deng, Y., . . . Huang, J., *Energ. Environ. Sci.* **2016,** *9*, 1752.

(28) Shao, Y.; Xiao, Z.; Bi, C.; Yuan, Y.; Huang, J., *Nat. Commun.* **2014,** *5*, 5784.

(29) Miyata, A.; Mitioglu, A.; Plochocka, P.; Portugall, O.; Wang, J. T.-W.; Stranks, S. D., . . . Nicholas, R. J., *Nature Physics* **2015,** *11*, 582.

(30) Yuan, Y.; Huang, J., *Acc. Chem. Res.* **2016,** *49*, 286.

(31) Sun, S.; Salim, T.; Mathews, N.; Duchamp, M.; Boothroyd, C.; Xing, G., . . . Lam, Y. M., *Energy Environ. Sci.* **2014,** *7*, 399.

(32) Savenije, T. J.; Ponseca, C. S., Jr.; Kunneman, L.; Abdellah, M.; Zheng, K.; Tian, Y., . . . Sundstrom, V., *J. Phys. Chem. Lett.* **2014,** *5*, 2189.

(33) Yang, Y.; Ostrowski, D. P.; France, R. M.; Zhu, K.; van de Lagemaat, J.; Luther, J. M.; Beard, M. C., *Nat. Photonics* **2015,** *10*, 53.

(34) Wehrenfennig, C.; Eperon, G. E.; Johnston, M. B.; Snaith, H. J.; Herz, L. M., *Adv. Mater.* **2014,** *26*, 1584.

(35) Xing, G.; Wu, B.; Wu, X.; Li, M.; Du, B.; Wei, Q., . . . Huang, W., *Nat. Commun.* **2017,** *8*, 14558.

(36) Yuan, M.; Quan, L. N.; Comin, R.; Walters, G.; Sabatini, R.; Voznyy, O., . . . Sargent, E. H., *Nat. Nanotechnol.* **2016,** *11*, 872.

(37) Kojima, A.; Ikegami, M.; Teshima, K.; Miyasaka, T., *Chem. Lett.* **2012,** *41*, 397.

(38) Lin, H.; Zhou, C.; Tian, Y.; Siegrist, T.; Ma, B., *ACS Energy Lett.* **2017,** *3*, 54.

(39) Ortiz-Cervantes, C.; Carmona-Monroy, P.; Solis-Ibarra, D., *ChemSusChem* **2019,** *12*, 1560.

(40) Stoumpos, C. C.; Cao, D. H.; Clark, D. J.; Young, J.; Rondinelli, J. M.; Jang, J. I., . . . Kanatzidis, M. G., *Chem. Mater.* **2016,** *28*, 2852.

(41) Katan, C.; Mercier, N.; Even, J., *Chem. Rev.* **2019,** *119*, 3140.

(42) Gauthron, K.; Lauret, J. S.; Doyennette, L.; Lanty, G.; Al Choueiry, A.; Zhang, S. J., . . . Deleporte, E., *Opt. Express* **2010,** *18*, 5912.

(43) Saparov, B.; Mitzi, D. B., *Chem. Rev.* **2016,** *116*, 4558.

(44) Mitzi, D. B.; Chondroudis, K.; Kagan, C. R., *IBM J. Res. Dev.* **2001,** *45*, 29.

(45) Cho, J.; Park, J. H.; Kim, J. K.; Schubert, E. F., *Laser Photonics Rev.* **2017,** *11*, 1600147.

(46) Adachi, C.; Lee, S.; Nakagawa, T.; Shizu, K.; Goushi, K.; Yasuda, T.; Potscavage, W. J., Organic Light-Emitting Diodes (OLEDs): Materials, Photophysics, and Device Physics. In *Organic Electronics Materials and Devices*, Springer: 2015; pp 43-73.

(47) Bender, V. C.; Marchesan, T. B.; Alonso, J. M., *IEEE Ind. Electron. Mag.* **2015,** *9*, 6.

(48) Lu, M.; Zhang, Y.; Wang, S.; Guo, J.; Yu, W. W.; Rogach, A. L., *Adv. Funct. Mater.* **2019,** *29*, 1902008.

(49) Dai, X.; Deng, Y.; Peng, X.; Jin, Y., *Adv. Mater.* **2017,** *29*, 1607022.

(50) Levchuk, I.; Osvet, A.; Tang, X.; Brandl, M.; Perea, J. D.; Hoegl, F., . . . Brabec, C. J., *Nano Lett.* **2017,** *17*, 2765.

(51) Era, M.; Morimoto, S.; Tsutsui, T.; Saito, S., *Appl. Phys. Lett.* **1994,** *65*, 676.

(52) Wang, N.; Cheng, L.; Ge, R.; Zhang, S.; Miao, Y.; Zou, W., . . . Huang, W., *Nat. Photonics* **2016,** *10*, 699.

(53) Quintero-Bermudez, R.; Gold-Parker, A.; Proppe, A. H.; Munir, R.; Yang, Z.; Kelley, S. O., . . . Sargent, E. H., *Nat. Mater.* **2018,** *17*, 900.

(54) Xiao, Z.; Kerner, R. A.; Zhao, L.; Tran, N. L.; Lee, K. M.; Koh, T.-W., . . . Rand, B. P., *Nat. Photonics* **2017,** *11*, 108.

(55) Ban, M.; Zou, Y.; Rivett, J. P. H.; Yang, Y.; Thomas, T. H.; Tan, Y., . . . Sun, B., *Nat. Commun.* **2018,** *9*, 3892.

(56) Zhao, L.; Rolston, N.; Lee, K. M.; Zhao, X.; Reyes-Martinez, M. A.; Tran, N. L., . . . Rand, B. P., *Adv. Funct. Mater.* **2018,** *28*, 1802060.

(57) Qin, C.; Matsushima, T.; Potscavage, W. J.; Sandanayaka, A. S. D.; Leyden, M. R.; Bencheikh, F., . . . Adachi, C., *Nat. Photonics* **2019,** *14*, 70.

(58) Wang, Q.; Wang, X.; Yang, Z.; Zhou, N.; Deng, Y.; Zhao, J., . . . Huang, J., *Nat. Commun.* **2019,** *10*, 5633.

(59) Li, Z.; Chen, Z.; Yang, Y.; Xue, Q.; Yip, H. L.; Cao, Y., *Nat. Commun.* **2019,** *10*, 1027.

(60) Yu, M.; Yi, C.; Wang, N.; Zhang, L.; Zou, R.; Tong, Y., . . . Wang, J., *Adv. Opt. Mater.* **2018,** *7*, 1801575.

(61) Yang, X.; Zhang, X.; Deng, J.; Chu, Z.; Jiang, Q.; Meng, J., . . . You, J., *Nat. Commun.* **2018,** *9*, 570.

(62) Lee, J. W.; Dai, Z.; Han, T. H.; Choi, C.; Chang, S. Y.; Lee, S. J., . . . Yang, Y., *Nat. Commun.* **2018,** *9*, 3021.

(63) Xiao, Z.; Kerner, R. A.; Tran, N.; Zhao, L.; Scholes, G. D.; Rand, B. P., *Adv. Funct. Mater.* **2019,** *29*, 1807284.

(64) Wang, Z.; Wang, F.; Sun, W.; Ni, R.; Hu, S.; Liu, J., . . . Tan, Z. a., *Adv. Funct. Mater.* **2018,** *28*, 1804187.

(65) Zou, W.; Li, R.; Zhang, S.; Liu, Y.; Wang, N.; Cao, Y., . . . Huang, W., *Nat. Commun.* **2018,** *9*, 608.

(66) Jiang, Y.; Qin, C.; Cui, M.; He, T.; Liu, K.; Huang, Y., . . . Chen, J., *Nat. Commun.* **2019,** *10*, 1868.

(67) Watanabe, S.; Cheng, T.; Tumen-Ulzii, G.; Qin, C.; Matsushima, T.; Adachi, C., *Appl. Phys. Lett.* **2019,** *115*, 233502.

(68) Fakharuddin, A.; Qiu, W.; Croes, G.; Devižis, A.; Gegevičius, R.; Vakhnin, A., . . . Heremans, P., *Adv. Funct. Mater.* **2019,** *29*, 1904101

Chapter 2

Stoichiometry Control for the Tuning of Grain Passivation and Domain Distribution in Green Quasi-2D Metal Halide Perovskite Films and Light-Emitting Diodes

2.1 Introduction

As introduced in Chapter 1, even though high-performing PeLEDs have been demonstrated with quasi-2D perovskites, a better understanding of their operational mechanisms behind has been required for future practical applications such as displays and lighting.

For example, it was commonly reported that the naturally formed multi-*n* configuration of quasi-2D perovskites induces the energy-level funnel effect, because the energy[1] and charge[2] transfer occur between domains. The energy-level funnel results in exciton confinement within high-*n* domains with low bandgaps, leading to higher E_B and thus higher emitting efficiency. However, in some reports, the energy-level funnel effect can be insufficient between domains with various *n*.[3] Besides, the interaction between excitons and the perovskite lattice in the confining domains might rapidly quench excitons through ultrafast non-radiative pathways[4] and make the order-mixing unfavorable for efficient emission.[5] Therefore, how the multi-*n* configuration influences the emitting efficiencies under different cases of *n* distribution requires comprehensive investigation. Furthermore, use of large organic ammonium cations can also passivate defects around domains or grains[6,7] besides forming quasi-2D structures (Figure 1-2c), and induce the dielectric confinement,[8] making the compositional control over perovskite even more complex.

Quasi-2D perovskite films are generally fabricated using spin-coating precursor solutions, in which pure 2D and 3D perovskite precursors are perfectly mixed at the stoichiometric ratio in terms of the molecular formula. This precursor composition is hereafter termed as the stoichiometric (ST**)** composition. On the other hand, quasi-2D perovskite films can also be obtained by simply adding a large organic halide salt into a 3D perovskite precursor. This precursor composition is hereafter termed as the large organic cation-doped (LOD**)**

composition.[9,10] Because of the difference in precursor ratio, LOD perovskite films should have different properties compared with ST ones. Although both the precursor composition strategies were reported to achieve high performance from quasi-2D PeLEDs, it is necessary to systematically investigate how the ST and LOD precursor compositions affect the defect passivation, *n* distribution, and thus the PL and EL performance of resulting quasi-2D perovskite films to avoid confusing interpretation.

In this Chapter, I studied the quasi-2D perovskite based on the 3D perovskite $FAPbBr_3$ and the large organic cation (PEA^+). From systematic analyses of the structural and optical properties of quasi-2D perovskite films, I investigated the role of PEA^+ under different ST and LOD composition conditions, which leads to a better understanding of the impact on defect passivation and domain distribution. I discuss reasons why low-*n* domains worse the emitting properties in films. Furthermore, while PEA^+ in ST perovskite films mainly functions as a passivator, PEA^+ contributes to not only the defect passivation but also the effective formation of the quasi-2D perovskite structures in LOD films, which results in high PL and EL efficiencies. Quasi-2D perovskite films fabricated with a well-designed LOD precursor composition achieved a high PLQY of 95.3% and showed green EL, with a maximum EQE and luminance of 14.7% and 37,477 cd m^{-2}, respectively.

2.2 Results and Discussion

The chemical formula of the ideal quasi-2D perovskite is $PEA_2FA_{n-1}Pb_nBr_{3n+1}$. However, in actual perovskite films, there are many domains with different orders *n*. Here I define the order used to prepare a precursor solution as the precursor recipe order n_r to distinguish from the aforementioned domain order *n* in films. As shown in Figure A-1 of the Appendix part, ST films were spin-coated from a precursor solution, in which the pure 2D PEA_2PbBr_4 and 3D $FAPbBr_3$ perovskites are dissolved. On the other hand, LOD films were spin-coated from a

precursor solution, in which the 3D $FAPbBr_3$ perovskite and PEABr are dissolved. In the perovskite precursor solutions, all the dissolved components exist as ions. To define the precursor order n_r for LOD solutions, I used the following equation, $\frac{2}{n_r-1} = \frac{[PEA^+]}{[FA^+]}$. This equation is also valid to obtain the precursor recipe order n_r for ST solutions. In ST solutions, the precursor formula is designed to be $PEA_2FA_{(n_r-1)}Pb_{n_r}Br_{(3n_r+1)}$, which is identical to the stoichiometry of the ideal quasi-2D structure. In LOD solutions, the precursor formula is $PEA_2FA_{(n_r-1)}Pb_{(n_r-1)}Br_{(3n_r-1)}$, where a unit of $PbBr_2$ is reduced compared with in ST solutions. Since the $[Pb^{2+}]$ in all the solutions were controlled to be the same to ensure the same amount of $PbBr_6$ octahedra formed in resulting films, with the same n_r (or the same $[PEA^+]/[FA^+]$), a LOD solution contains a higher concentration of overall organic cations than an ST solution does. This overdose of organic cations in LOD perovskites makes their properties distinct to those of ST perovskites, which is discussed in the following sections.

2.2.1 Structural Properties of Quasi-2D Perovskite Films

I first characterized the structural properties of quasi-2D perovskite films with XRD. Figure 2-1a and 2-1b show XRD patterns of quasi-2D perovskite films fabricated from the ST and LOD precursor compositions. In ST films fabricated with $n_r \geq 3.5$ and LOD films fabricated with $n_r \geq 6$, only the XRD peaks of high-*n* perovskite domains were present although the positions of these peaks were somewhat different compared with the pure 3D $FAPbBr_3$, which will be discussed later. According to a previous report of our laboratory using the same quasi-2D perovskite system for grazing-incidence wide-angle X-ray scattering GIWAX analysis,[10] the formed perovskite domains adopt all orientations in the films, but with slightly preferential alignment parallel to the substrate. In ST films with $n_r < 3.5$ and LOD films with $n_r < 6$, the XRD peaks originating from $n = 1$ and $n = 2$ perovskite domains appeared, along with the existence of the high-*n* perovskite domains. The aforementioned results indicate that the

addition of excess organic ammonium cations makes the formation of the low-*n* perovskite domains easier in LOD films.

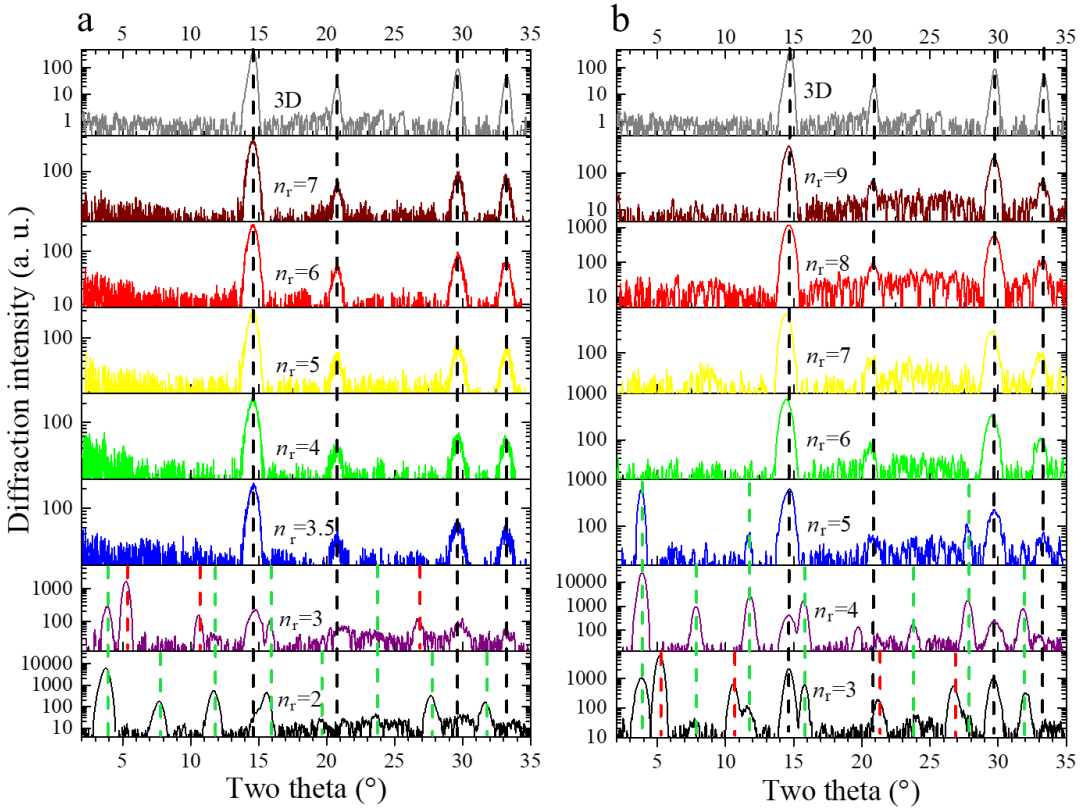

Figure 2-1. XRD patterns of (a) ST and (b) LOD perovskite films. The y-axis scale is logarithmic to make it easier to see the peaks. The peaks labeled with the black, red, and green dashed lines respectively correspond to the high-*n*, *n* = 1, and *n* = 2 perovskite domains.

The XRD peaks at ~14.7 °, which are assigned to the (100) plane of the high-*n* perovskite domains,[5] are magnified to see a change of their peak positions. While little peak shift was recognized in ST films (Figure 2-2a), the peak shift to a lower degree was clearly detected in LOD films (Figure 2-2b), with the largest shift occurring at n_r = 6 or 7. The gradual incorporation of PEA^+ into the 3D lattice for the formation of the middle-*n* or high-*n* perovskite domains may induce lattice expansion and thus slightly increased lattice constant, which leads to this peak shift.[9] In LOD films with n_r < 6, the XRD peaks gradually returned to a higher degree. This is because PEA^+ cations are preferentially consumed to form the *n* = 1 and *n* = 2 perovskite domains as such low-*n* domains tend to form at a very early stage of the film fabrication.[11]

The size of the high-*n* perovskite domains was estimated from the (100) peaks using Scherrer equation with a shape factor of 0.89. As shown in Figure 2-2c, in both ST and LOD films, the domain size firstly decreased and then began to increase gradually as the n_r decreased. The decreased domain size in the large n_r region may be because increasing the PEA^+ concentrations restricts the crystal growth during the film formation.[9,12] At the small n_r, as PEABr was used to form the low-*n* domains, the aforementioned restriction of the crystal growth was released, probably resulting in the rapidly increased size of the high-*n* domains. The smallest domain size was obtained at n_r = 3.5 for ST films and n_r = 6 for LOD films.

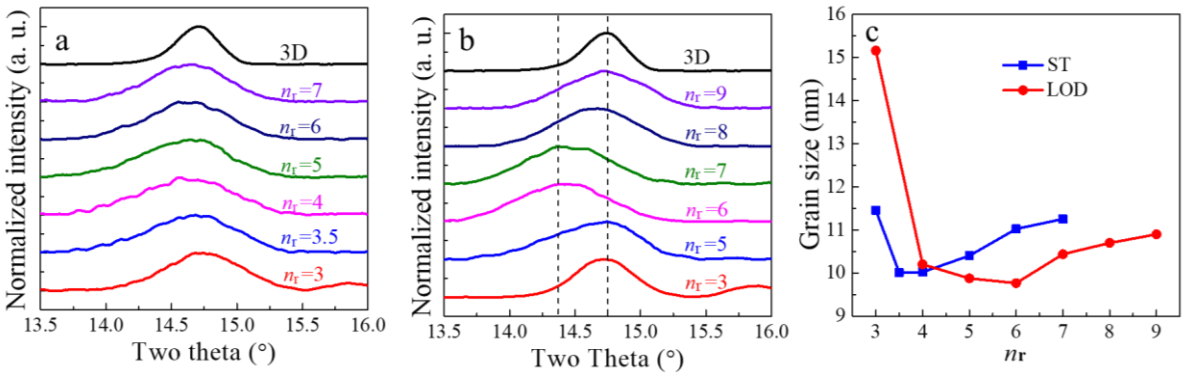

Figure 2-2. Magnified XRD patterns of (a) ST and (b) LOD perovskite films. The dashed lines are guides for the eye to see the peak shift. (c) Size of the high-*n* perovskite domains in ST and LOD films, which was estimated using Scherrer equation.

2.2.2 Optical Properties of Quasi-2D Perovskite Films

The presence of the *n* = 1 and *n* = 2 perovskite domains fabricated with low n_r was also evidenced by the absorption spectra shown in Figure 2-3a and 2-3b. In ST films with $n_r \geq 3.5$ and LOD films with $n_r \geq 6$, the absorption onsets shifted to a shorter wavelength as n_r was decreased, probably because of the bandgap widening by a quantum confinement effect associated with the decreased domain order.[13] Besides, no multiple absorption peaks from different perovskite domains were found in these films. On the other hand, sharp excitonic peaks originating from the *n* = 1 and *n* = 2 perovskite domains[14] were observed in the other ST

films with n_r < 3.5 and LOD films with n_r < 6, which is consistent with the XRD results discussed earlier.

The quantum confinement effect from quasi-2D structure can also be reflected by PL peak wavelengths. As shown in Figure 2-3c, 2-3d, and 2-3e, the more blue-shifted PL peaks of LOD films than those of ST films at all n_r values indicate the lower *n* of emitting domains. This further confirms the promoted incorporation of PEA^+ into the perovskite lattice in LOD films. The co-existence of multiple PL peaks in low-n_r films can be clearly recognized in the low-temperature PL analysis as shown in Figure A-3, Appendix, because of the multi-*n* configuration when low-*n* domains appeared. In all ST films, the main PL peak came from high-*n* domains. However, the main PL peak in low-n_r LOD films was obviously attributed to some low-*n* or middle-*n* domains, keeping the significant PL blueshift even with the appearance of low-*n* domains, although all of the perovskite films contained low-band-gap high-*n* domains (Figure A-3, Appendix). This indicates that the energy or carrier transfer from the low-*n* to high-*n* domains is more insufficient in LOD films, which may be influenced by the spacial locations of domains with different *n*. Some emitting middle-*n* domains in LOD films were not detected in the XRD results, probably because of the absence of long-range crystalline ordering.[15]

Plots of PLQY values as a function of n_r are shown in Figure 2-3f. PLQY values increased as the n_r was decreased. This behavior is typical in quasi-2D perovskite films and may result from stronger exciton confinement associated by the decreased *n* or better defect passivation by PEA^+ at domain boundaries.[1,5,16] Further decreasing n_r resulted in a decrease of PLQYs, probably because of the appearance of the low-*n* domains, the reason of which is discussed later. The highest PLQYs were obtained when n_r was 3.5 for ST films (~54.9%) and n_r was 6 for LOD films (~70.6%).

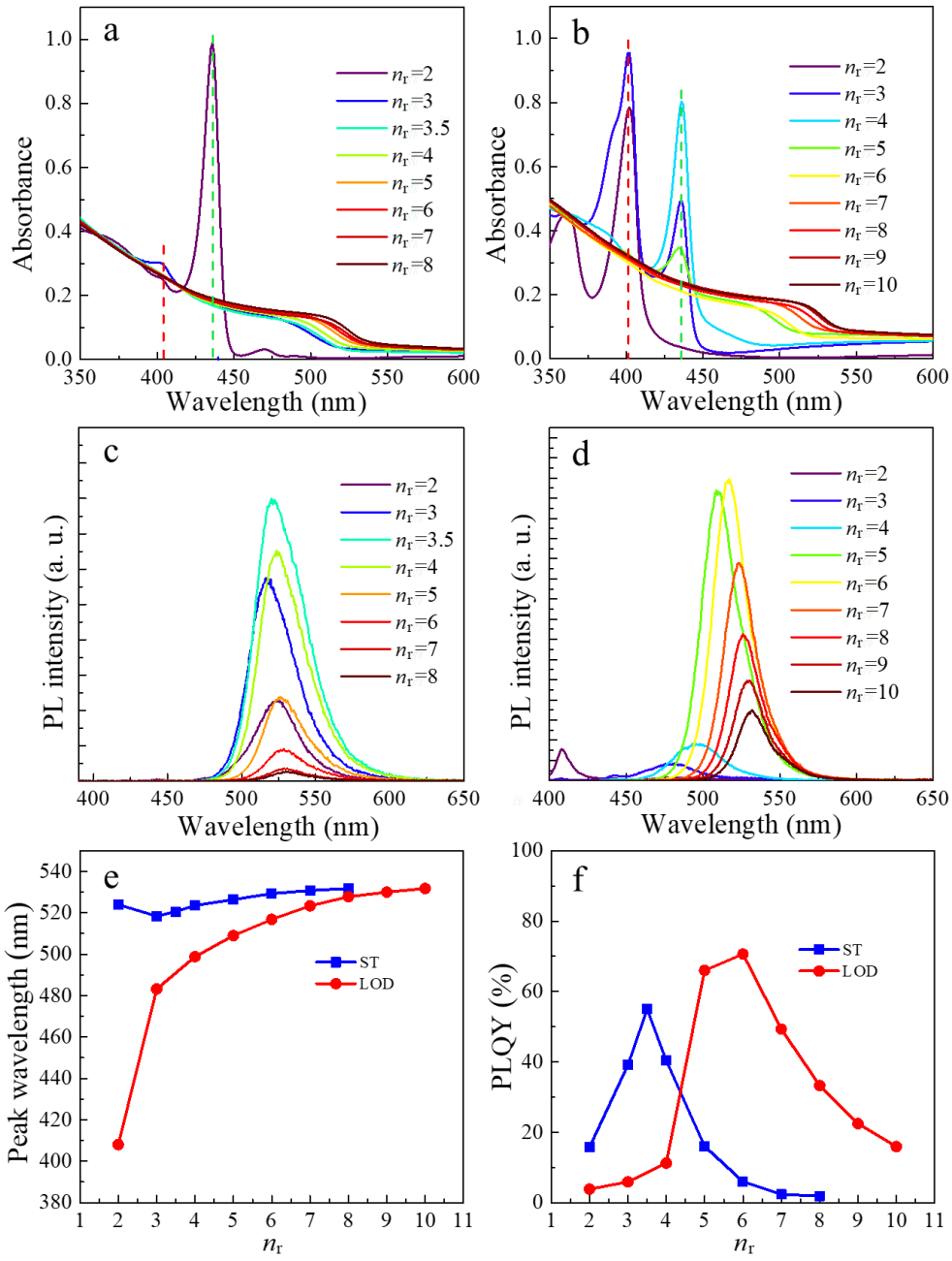

Figure 2-3. Absorption spectra of (a) ST and (b) LOD perovskite films. The red and green dashed lines in (a) and (b) represent the excitonic peaks coming from the n = 1 and n = 2 domains, respectively. PL spectra of (c) ST and (d) LOD perovskite films. (e) PL peak wavelengths and (f) PLQY values of ST and LOD perovskite films as a function of n_r.

2.2.3 Effect of Defect Passivation and Exciton Confinement on Photoluminescence Quantum Efficiencies

To obtain Figure 2-3f, I used a low excitation fluence of ~0.001 mW cm^{-2} at an excitation wavelength of 365 nm. Next, I measured excitation-dependent PLQYs for ST and LOD films

(Figure 2-4a and 2-4b). An increase in PLQY with increasing the excitation fluence would be due to a filling of defects by charge carriers or excited states generated under the photoexcitation.[1] The PLQY values began to decrease in a high fluence region, which may be due to Auger recombination.[2] In films with higher PLQYs, values of PLQY became maximum at lower excitation fluence, probably because of lower defect density. As shown in Figure A-2 of the Appendix part, the maximum PLQY values obtained at the appropriate excitation fluences changed in the manner similar to those obtained at the low fluence (Figure 2-3f). The highest PLQY of LOD films with $n_r = 6$ achieved 95.3%.

According to a previous report, large organic ammonium cations can passivate defect states at grain or domain boundaries.[6,7,9] Therefore, I infer that the LOD precursor compositions using excess organic cations lead to the better defect passivation and higher PLQYs. In ST and LOD films with lower n_r, as PEA^+ cations are used to form low-*n* perovskite domains, it is difficult to effectively passivate the defect states at the domain boundaries, resulting in the low PLQY.

Another possible reason for the n_r dependence of the PLQYs is the exciton confinement effect, which results from the decreased domain *n* and can be quantified by E_B. The E_B can be calculated by fitting the plot of PL spectrum area versus temperature with conventional Arrhenius equation.[1] Figure A-3 and A-4 in the Appendix part display temperature-dependent PL spectra and their fitting results. As shown in Figure 2-4c, I found that films with higher E_B likely have higher PLQYs, indicating the importance of the exciton confinement effect for enhancing PLQYs. The small difference in n_r, which provided the highest E_B and PLQY, is possibly because the low-*n* perovskite domains surrounding the high-*n* perovskite domains induces extra exciton confinement.[17] When low-*n* domains did not appear, LOD films had obviously higher E_B than ST films had. The E_B values estimated here are reasonable among previously reported quasi-2D perovskite films.[18]

For a better understating of the effect of grain passivation and E_B, I studied the parameters of different recombination pathways through time-resolved PL (TRPL) measurements on ST and LOD perovskite films (Figure A-5, Appendix). All the PL decay curves can be finely fitted with a tri-exponential decay equation:[19]

$$\frac{I(t)}{I_0} = f_1 e^{-\frac{t}{\tau_1}} + f_2 e^{-\frac{t}{\tau_2}} + f_3 e^{-\frac{t}{\tau_3}} \qquad (2-1)$$

where $I(t)$ is the PL intensity, I_0 is the initial PL intensity, τ_i values are the lifetimes of different decay components, and f_i values are the fractions of different decay components. Table A-1 and A-2 in the Appendix part summarize the parameters obtained from the fitting. For every sample, there are a τ_1 of several ns, a τ_2 of tens of ns, and a τ_3 of hundreds of ns, which represent different releasing pathways of excited states in quasi-2D perovskites. As discussed in previous reports,[20] τ_1, τ_2, and τ_3 can be ascribed to the fast defect-induced quenching, the excitonic radiative recombination, and the slow free carrier radiative recombination, respectively. The f_i values of the three PL decay components are plotted as a function of n_r in Figure 2-4d. The f_2 values are much higher than f_3 values, indicating that excitonic recombination is the predominant radiative recombination in quasi-2D perovskites. Values of f_1 reach the lowest value and values of f_2 reach the highest value at n_r which provided the highest PLQY for both ST and LOD films. This represents the case of the lowest fraction of defect-induced quenching and the highest fraction of excitonic recombination, which is a result of better passivation and higher E_B.

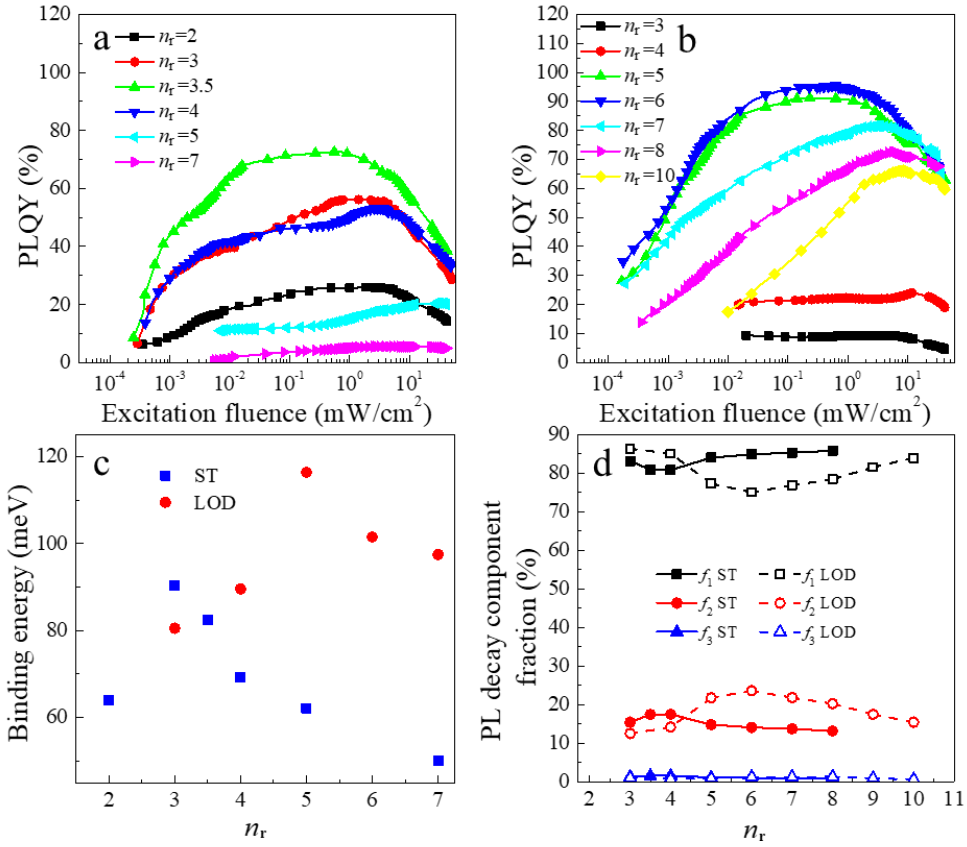

Figure 2-4. PLQY values of (a) ST and (b) LOD perovskite films at different excitation fluences. Plots of (c) exciton binding energies and (d) various PL decay component fractions of ST and LOD perovskite films as a function of n_r.

2.2.4 Mechanisms of Domain Formation Impacted by Precursor Compositions

On the basis of the experimental results discussed earlier, I depict the quasi-2D perovskite structures with various n_r. Figure 2-5a exhibits the ideal quasi-2D perovskite structures, in which the thickness of the stacked $PbBr_6$ octahedral slabs exactly corresponds to n_r. However, in the actual films, increasing the concentration of PEA^+ decreases the domain size and a lot of PEA^+ ions exist at the domain boundaries for the defect passivation as illustrated in Figure 2-5b and reported in ref. 6. The PEA^+ passivators on the domain boundaries can also provide the dielectric confinement.[8] These effects are more pronounced in LOD films than in ST films because of the presence of excess organic cations relative to Pb^{2+} cations. Besides, I think that PEA^+ cations are easier to incorporate into the perovskite lattice in LOD films to form quasi-

2D structures, thus inducing the more significant quantum confinement. However, at the small n_r, as the large amount of the low-*n* perovskite domains emerges, the effect of the defect passivation and dielectric and quantum confinement becomes weak.

Besides the depletion of PEA^+, another possible reason why the formation of low-*n* perovskite domains makes PLQY lower is the superfast quenching process of excitons.[18] Except defect-induced quenching, the exciton-phonon scattering was also reported to effectively quench excitons in pure 2D perovskites (n = 1),[20] with a PL lifetime lower than 1 ns,[16] resulting in the non-radiative recombination rate nearly two orders of magnitude higher than radiative one.[21] The exciton-phonon scattering also appears in the n = 2 domains.[4] It makes sense that this ultra-fast quenching in low-*n* perovskite domains could happen more significantly than the energy transfer to high-*n* perovskite domains.

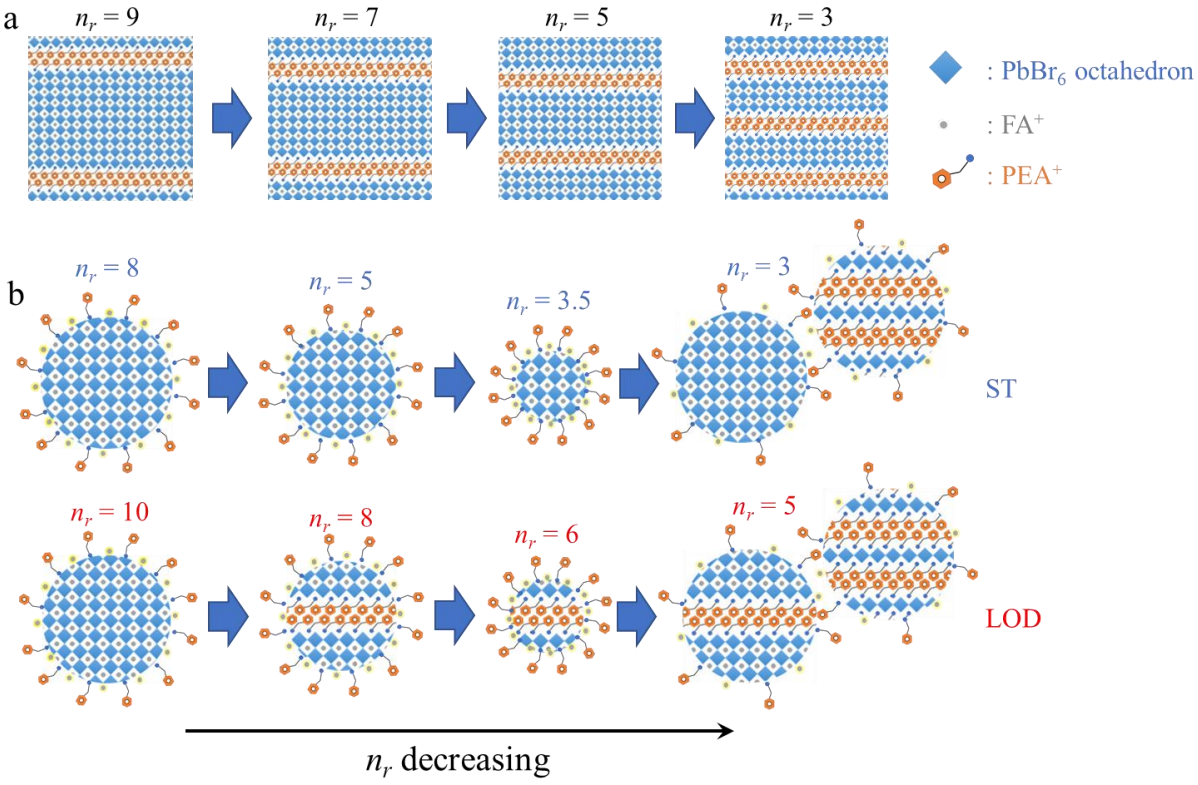

Figure 2-5. Schematics of (a) ideal quasi-2D perovskite structures and (b) speculated actual situations in ST and LOD films. The arrows indicate a direction of decreasing the n_r.

To further confirm the influence of low-*n* domains, I fabricated ST films with an n_r of 5 using a dimethyl sulfoxide (DMSO) solution. As shown in Figure A-6 in the Appendix part, these films had a clear trace of low-*n* perovskite domains when compared with the previously discussed ST films fabricated from an *N*,*N*-dimethylformamide (DMF) solution. The higher boiling point of DMSO (189 ℃) than that of DMF (153 ℃) could make the formation of the low-*n* perovskite domains easier. Since the thicknesses of the films fabricated with the different solvents were similar, the lower PL intensities of the films fabricated with DMSO confirmed that the low-*n* perovskite domains are unfavorable.

2.2.5 LEDs Device Performances

I fabricated PeLEDs with an architecture of glass substrate/indium tin oxide (ITO) anode/PVK hole transport layer (30 nm)/perovskite emitting layer (60 nm)/TPBi electron transport layer (40 nm)/LiF electron injection layer (1 nm)/Al cathode (100 nm) (Figure 2-6a). Here, PVK and TPBi stand for poly(*N*-vinylcarbazole) and 1,3,5-tris(1-phenyl-1*H*-benzo[d]imidazol-2-yl)benzene, respectively, with the chemical structures shown in Scheme 2-1. For ST PeLEDs, there was a good relationship between the EQEs and the PLQYs; both the EQE and the PLQY reached the highest at n_r = 3.5 (Figure 2-6b). However, the EQE of LOD PeLEDs was the highest at n_r = 8 (Figure 2-6c). This n_r is different from n_r = 6, at which the highest PLQY was obtained, and the reason of which is still unclear and may be related to the carrier balance factor. Furthermore, all the devices had a strong EQE roll-off in a high current density region, which will be discussed in Chapter 3.

Here I compared the device performance of the best ST (n_r = 3.5) and LOD (n_r = 8) PeLEDs. The EL spectra of both LOD and ST PeLEDs were similar, with the peak wavelength of ~529 nm originated from the quasi-2D perovskite emitters. The FWHM value was ~23 nm, pointing to EL with high color purity (Figure 2-6d). Driving voltages were lower in LOD

PeLED than in ST PeLEDs (Figure 2-6e). I attributed the lower voltages to better carrier transport in LOD films than ST films because of the smaller amount of the insulating PEA^+ component in LOD films.[9] The respective PEA^+ concentrations were 0.1 and 0.2 M in the precursor solutions used for LOD PeLEDs with n_r = 3.5 and LOD PeLEDs with n_r = 8 (Table A-3 and A-4, Appendix).

Additionally, LOD PeLEDs had higher maximum luminance (Figure 2-6e) and approximately twice higher EQEs and current efficiencies (Figure 2-6f) compared with ST PeLEDs although the PLQY values were similar between the corresponding LOD and ST films (~70%). The maximum luminance and EQE achieved 37,477 cd m^{-2} and 14.7% for LOD PeLEDs while they were 3,664 cd m^{-2} and 6.8% for ST PeLEDs. Considering the PLQY values (~70%) and the reported out-coupling efficiency (23%)[10] of a similar device architecture, the internal quantum efficiencies were calculated as 87.5% for LOD PeLED and 42.2% for ST PeLEDs. One reason for the higher efficiencies is the better morphology of LOD films (Figure A-7 in the Appendix part) with lower roughness and less pinholes, which reduces the formation of shunting paths between the two electrodes and suppresses the leak current. Another reason could be the less influence from Auger recombination because the more suppressed decrease in PLQY at higher excitation fluence in LOD films with n_r = 8 than in ST films with n_r = 3.5 (Figure 2-4a and 2-4b).

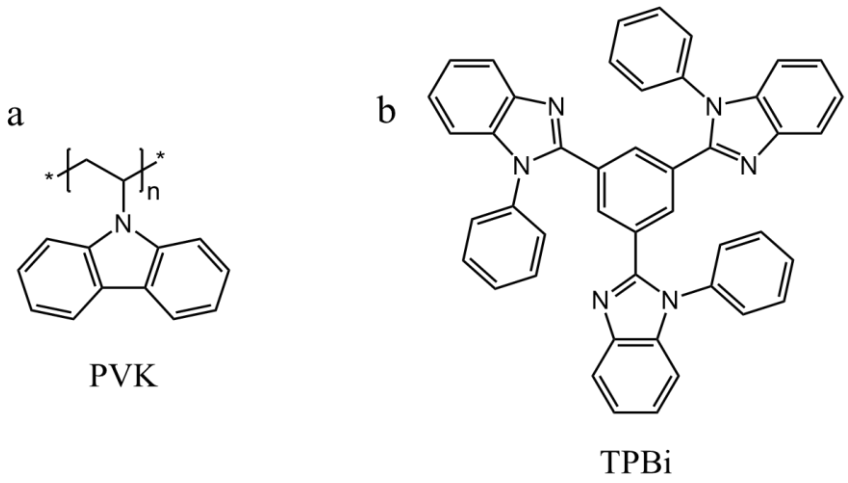

Scheme 2-1. The chemical structures of (a) PVK and (b) TPBi.

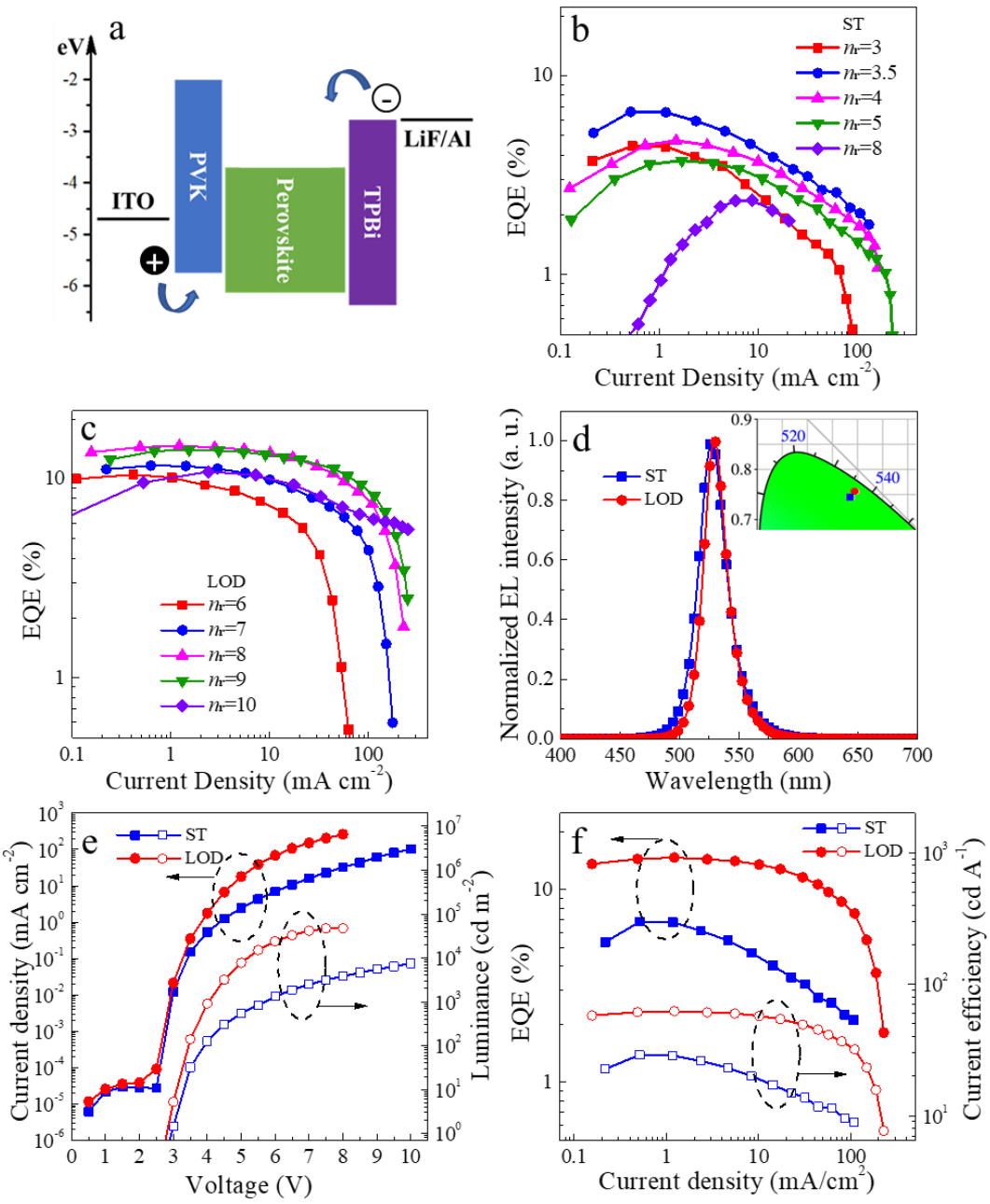

Figure 2-6. (a) Device architecture. EQE versus current density curves of (b) ST and (c) LOD PeLEDs with various n_r. (d) Normalized EL spectra, (e) current density versus voltage (*J*-*V*) and luminance versus voltage curves, and (f) EQE versus current density and current efficiency versus current density curves of ST (n_r = 3.5) and LOD (n_r = 8) PeLEDs. The inset of (d) shows Commission Internationale de L'Éclairage color coordinates.

The EL stability of ST (n_r = 3.5) and LOD (n_r = 8) PeLEDs was evaluated under constant-current driving at 0.25 mA cm^{-2}. For comparison, the PL stability of ST (n_r = 3.5) and LOD (n_r = 8) films was also measured under the continuous irradiation of excitation light with a wavelength of 365 nm and a power of 4.3 mW cm^{-2}. These stability results are shown in Figure

A-8, Appendix. Compared with ST samples, LOD samples exhibited better EL and PL stability. It is worth mentioning that the EL and PL intensities of ST samples first increased and then decreased with time. The increase in EL and PL intensity at the initial stage can be attributed to a gradual filling of defect states with charge carriers or excited states.[22] On the other hand, no increase in EL and PL intensity was observed from LOD samples, which may be due to lower defect density as I discussed earlier. Since, on the basis of our lab's previous results,[22] the co-existence of excited states and charge carriers in PeLEDs accelerates the degradation, thus the EL stability was inferior to the PL stability (Figure A-8). Overall, I succeeded in demonstrating that choosing the appropriate LOD precursor composition can increase the EL and PL stability. However, the half lifetime, at which EL intensity decreases to half of the initial, was very low (less than one hour). The degradation mechanisms of PeLEDs will be further discussed in Chapter 3.

2.3 Conclusion

In conclusion, I studied the optical, structural, LED performance of quasi-2D perovskite films fabricated with ST and LOD precursor compositions with different n_r. I found that, while PEA^+ cations in ST films mainly function as a passivator, PEA^+ cations in LOD films work for not only the defect passivation but also the effective formation of small quasi-2D perovskite domains. In either case, the formation of low-*n* domains is unfavorable because these domains make PLQYs lower. More efficient defect passivation, higher binding energy, and, therefore, higher PLQYs were achieved in LOD films than in ST films. LOD perovskite films with the well-designed precursor composition achieved a high PLQY of 95.3%, maximum EQE of 14.7%, and maximum luminance of 37,477 cd m^{-2}. These findings will shed light upon the importance of controlling the precursor stoichiometry for the defect passivation, quasi-2D domain distribution, and LED performance.

2.4 Experimental

Material and precursor preparation: FABr, $PbBr_2$, and PEABr were purchased from Tokyo Chemical Industry. PVK, 18-crown-6, chlorobenzene, DMF, and toluene were purchased from Sigma-Aldrich. TPBi was purchased from Lumtec. These materials were used without purification while TPBi was purified by a train sublimation method prior to use. A $FAPbBr_3$ precursor solution was prepared by dissolving FABr and $PbBr_2$ into DMF at a concentration of 0.35 M and stirred overnight at room temperature for 12 h. A $(PEA)_2PbBr_4$ precursor solution was prepared by dissolving PEABr and $PbBr_2$ into DMF at a concentration of 0.35 M and stirred overnight at room temperature for 12 h. To prepare ST solutions, the aforementioned $FAPbBr_3$ and $(PEA)_2PbBr_4$ solutions were mixed at a certain ratio. To prepare LOD solutions, the certain amount of PEABr was added into the $FAPbBr_3$ solution. These ST and LOD solutions were stirred for 3 h at room temperature. 18-crown-6 was finally added into all the precursor solutions at a concentration of 3.5 mM to help the better dispersion of PEABr.

Perovskite film and LED fabrication: Perovskite films used for measuring the optical, structural, and morphological properties were fabricated on fused silica substrates. Glass substrates coated with a pre-patterned ITO layer with a thickness of 50 nm were used for the LED fabrication. The aforementioned substrates were ultrasonically cleaned in detergent, pure water, acetone, and isopropanol for 15 min, followed by boiling in isopropanol for 10 min. After that, the substrates were transferred to a nitrogen-filled glovebox with the O_2 and H_2O concentrations < 10 ppm. A PVK layer was spin-coated on the clean ITO surface at 1,000 rpm for 1 min using a solution of PVK in chlorobenzene (5.5 mg mL^{-1}) and annealed at 150 ℃ for 15 min. A perovskite layer was fabricated with the precursor solutions *via* a two-stage spin-coating (500 rpm and 5 s for the first stage and 4,500 rpm and 45 s for the second stage). 3.6−3.9 seconds after the second stage began, 0.23 mL of toluene was dropped on the film. The sample was immediately annealed at 100 ℃ for 7 min. Next, the substrates were transferred to a

vacuum evaporation chamber. After the evacuation of the chamber to < 10^{-4} Pa, 100-nm-thick TPBi, 0.8-nm-thick LiF, and 100-nm-thick Al layers were vacuum-deposited onto the perovskite layer to complete PeLEDs. After the PeLEDs were unloaded from the chamber to the glovebox without exposure to air, the PeLEDs were encapsulated with a quartz glass lid and ultraviolet-cured resin.

PeLED characterization: The EL spectra and current density versus voltage, luminance versus current density, EQE versus current density, and current efficiency versus current density characteristics of the PeLED were measured under room temperature using an integrating sphere system (A10094, Hamamatsu Photonics), which was equipped with a computer-controlled source meter (2400, Keithley) and a photonic multi-channel analyzer (C9920-12, Hamamatsu). The operational stability was measured using the same system.

Absorption, PL spectroscopy and TRPL measurements: The ultraviolet-visible absorption measurement was carried out with a Lambda 950-PKA Perkin-Elmer spectrophotometer. The PL spectra were measured with a spectrofluorometer (Fluoromax-4, Horiba Jobin Yvon). The TRPL curves were measured with a fluorescence lifetime measurement system (Quantaurus-Tau, Hamamatsu Photonics). Both PL spectra and PLQY curves were collected with an excitation wavelength of 365 nm.

PLQY measurement: The PLQY values were estimated with a reference sample of a tris(8-hydroxyquinolinato) aluminum (Alq_3) thin film vacuum-deposited on a fused silica substrate. The absorbance and PL spectra of this reference sample were measured under the same conditions with the perovskite samples. The absolute PLQY of the reference sample was measured under the 365-nm optical excitation with a Hamamatsu Quantaurus-QY system. The PLQY values of perovskite samples were calculated by comparing the absorbance and PL spectra of the reference and perovskite samples and the absolute PLQY of the reference sample.

Excitation fluence dependent PLQY and optical stability: The PL intensities of the reference and perovskite samples at different excitation fluences were detected by Thorlabs photodiodes. The excitation fluence-dependent PLQY values were calculated by considering the absorbance and PL intensities of the reference and perovskite samples and the absolute PLQY of the reference at each excitation power. The optical stability was measured with the aforementioned set-up, which is composed of the excitation light source and photodiodes.

Temperature-dependent PL spectra: A perovskite film was cooled in vacuum with a cryostat with a helium compressor unit (CNA-11B, Sumitomo). At various temperatures, PL spectra of the film were measured using a photonic multi-channel analyzer (C14631, Hamamatsu) under the photoexcitation with a wavelength of 365 nm.

XRD measurement: The XRD patterns were measured with an X-ray diffractometer (Rigaku, RINT-2500) using a conventional $2\theta/\theta$ technique [λ = 1.54 Å (CuKα)]. To avoid the degradation in air, a perovskite film was covered with a plastic dome with nitrogen filled in.

AFM measurement: AFM images were measured in tapping mode with an AFM microscope (JSPM-5400, JEOL).

Film thickness measurement: The thicknesses of each film used in this study were measured with a surface profilometer (DektakXT, Bruker).

2.5 References

(1) Yuan, M.; Quan, L. N.; Comin, R.; Walters, G.; Sabatini, R.; Voznyy, O., . . . Sargent, E. H., *Nat. Nanotechnol.* **2016,** *11*, 872.

(2) Yu, M.; Yi, C.; Wang, N.; Zhang, L.; Zou, R.; Tong, Y., . . . Wang, J., *Adv. Opt. Mater.* **2018,** *7*, 1801575.

(3) Ban, M.; Zou, Y.; Rivett, J. P. H.; Yang, Y.; Thomas, T. H.; Tan, Y., . . . Sun, B., *Nat. Commun.* **2018,** *9*, 3892.

(4) Guo, Z.; Wu, X.; Zhu, T.; Zhu, X.; Huang, L., *ACS Nano* **2016,** *10*, 9992.

(5) Yang, X.; Zhang, X.; Deng, J.; Chu, Z.; Jiang, Q.; Meng, J., . . . You, J., *Nat. Commun.* **2018,** *9*, 570.

(6) Lee, J. W.; Dai, Z.; Han, T. H.; Choi, C.; Chang, S. Y.; Lee, S. J., . . . Yang, Y., *Nat. Commun.* **2018,** *9*, 3021.

(7) Xiao, Z.; Kerner, R. A.; Tran, N.; Zhao, L.; Scholes, G. D.; Rand, B. P., *Adv. Funct. Mater.* **2019,** *29*, 1807284.

(8) Katan, C.; Mercier, N.; Even, J., *Chem. Rev.* **2019,** *119*, 3140.

(9) Xiao, Z.; Kerner, R. A.; Zhao, L.; Tran, N. L.; Lee, K. M.; Koh, T.-W., . . . Rand, B. P., *Nat. Photonics* **2017,** *11*, 108.

(10) Qin, C.; Matsushima, T.; Potscavage, W. J.; Sandanayaka, A. S. D.; Leyden, M. R.; Bencheikh, F., . . . Adachi, C., *Nat. Photonics* **2019,** *14*, 70.

(11) Sun, Y.; Zhang, L.; Wang, N.; Zhang, S.; Cao, Y.; Miao, Y., . . . Huang, W., *npj Flexible Electronics* **2018,** *2*, 1.

(12) Han, D.; Imran, M.; Zhang, M.; Chang, S.; Wu, X. G.; Zhang, X., . . . Zhong, H., *ACS Nano* **2018,** *12*, 8808.

(13) Blancon, J. C.; Tsai, H.; Nie, W.; Stoumpos, C. C.; Pedesseau, L.; Katan, C., . . . Mohite, A. D., *Science* **2017,** *355*, 1288.

(14) Lee, H. D.; Kim, H.; Cho, H.; Cha, W.; Hong, Y.; Kim, Y. H., . . . Lee, T. W., *Adv. Funct. Mater.* **2019**, 1901225.

(15) Quintero-Bermudez, R.; Gold-Parker, A.; Proppe, A. H.; Munir, R.; Yang, Z.; Kelley, S. O., . . . Sargent, E. H., *Nat. Mater.* **2018,** *17*, 900.

(16) Byun, J.; Cho, H.; Wolf, C.; Jang, M.; Sadhanala, A.; Friend, R. H., . . . Lee, T. W., *Adv. Mater.* **2016,** *28*, 7515.

(17) Zou, W.; Li, R.; Zhang, S.; Liu, Y.; Wang, N.; Cao, Y., . . . Huang, W., *Nat. Commun.* **2018,** *9*, 608.

(18) Ma, S.; Cai, M.; Cheng, T.; Ding, X.; Shi, X.; Alsaedi, A., . . . Dai, S., *Sci. China Mater.* **2018,** *61*, 1257.

(19) Tsai, H.; Nie, W.; Blancon, J. C.; Stoumpos, C. C.; Soe, C. M. M.; Yoo, J., . . . Mohite, A. D., *Adv. Mater.* **2018,** *30*, 1704217.

(20) Xing, G.; Wu, B.; Wu, X.; Li, M.; Du, B.; Wei, Q., . . . Huang, W., *Nat. Commun.* **2017,** *8*, 14558.

(21) Kawano, N.; Koshimizu, M.; Sun, Y.; Yahaba, N.; Fujimoto, Y.; Yanagida, T.; Asai, K., *The Journal of Physical Chemistry C* **2014,** *118*, 9101.

(22) Watanabe, S.; Cheng, T.; Tumen-Ulzii, G.; Qin, C.; Matsushima, T.; Adachi, C., *Appl. Phys. Lett.* **2019,** *115*, 233502.

Chapter 3

Ion Migration-Induced Degradation and Efficiency Roll-off in Quasi-2D Perovskite Light-Emitting Diodes

3.1 Introduction

In Chapter 2, I mentioned that, with the same excitation fluence of PL and EL, quasi-2D perovskites under electrical driving have a much shorter lifetime than under optical driving. That indicates a special degradation mechanism under EL for quasi-2D perovskites. Also, despite the high PL and EL efficiencies,[1–4] quasi-2D PeLEDs, especially green- and blue-emitting PeLEDs, still suffer from low operational durability.[5] The device lifetimes of high-efficiency quasi-2D PeLEDs reported so far are only in the timescale of minutes,[3,4,6,7] which agrees with my results in Chapter 2 and seriously impedes the practical applications in industry. The factors, such as defect-assisted decomposition[8] and imbalanced charge injection[9], were found to lower the operational durability. Besides, quasi-2D PeLEDs are also known to have a strong EQE roll-off at high current densities.[9–12] One source of the EQE roll-off is Auger recombination.[10] However, other convincing explanations to understand the PeLEDs' degradation and EQE roll-off would exist.

Besides, as introduced in Chapter 1, ion migration is an important factor of many unusual phenomena in perovskite solar cells, such as photocurrent hysteresis, photo-induced giant dielectric constant, photo-induced phase separation, and a rapid decline of device performances.[13,14] Therefore, exploring the influence of ion migration in quasi-2D PeLEDs might provide important clues for the source of their short working lifetimes.

Here, I investigated the degradation and EQE roll-off of quasi-2D PeLEDs associated with ion migration. I found that the organic cations passivating defect states at domain boundaries drift under external bias, causing some domains losing passivation of defects. This process, which was evidenced by the recovery behaviors and transient EL results of PeLEDs, was found to contribute to the reversible EQE decay and severe roll-off under high current densities. Furthermore, under long electrical operation, the mobile cations entered the electron

transport layer (ETL), which damaged the electron transport property of the ETL and resulted in an irreversible decay of device's EQEs. The mechanisms I discovered in this chapter give a good explanation to the EQE decay behaviors of PeLEDs and would provide a direction for future research on optimizing the operational durability of quasi-2D PeLEDs.

3.2 Results and Discussion

The study was carried out on PeLEDs with the architecture shown in Figure 2-6a. The perovskite emitting layer in the PeLEDs was fabricated using the LOD precursor composition described in Chapter 2. As shown in Figure 2-6c, the EQE roll-off behaviors depended upon the n_r values; PeLEDs with lower n_r tended to have more severe EQE roll-off although all the devices had very fast EQE roll-off, which is similar to the roll-off behavior in some other previous reports,[9] and will be discussed in following contents.

3.2.1 Evolutions of LED Properties During Continuous Operation

Constant-current lifetime measurement was carried out on PeLEDs at 0.25 mA cm^{-2}. At this current density, the EQEs reached the values above 10%. The normalized driving voltage and EQE curves versus the working time are shown in Figures 3-1a and 3-1b. It is clear that EQEs of all the devices slowly degraded in the first stage. In the second stage, the EQE degradation was obviously faster than in the first stage. Interestingly, the driving voltages decreased slowly in the first stage, which should be attributed to the redistribution of build-in fields, and will be discussed later. The driving voltages then increased significantly fast in the second stage, which could be a result of degraded electronic properties of devices. The different trends of the driving voltage in the different stages should be related to the mechanisms of the EQE decay. The relationship between the EL peak wavelength and the working time was exhibited in Figure 3-1c. The EL peak was blue-shifted as n_r decreased, due to the widened

bandgap from the quantum size effect of the quasi-2D perovskite. It is worth noticing that the EL peaks of all the devices did not exhibit any trend of shifting during the whole process of operation. The normalized EL spectra at the beginning and the end of the constant-current measurement also exhibited no difference (Figure 3-1d). The spectroscopic properties (including the peak positions and shapes) of the quasi-2D perovskite are known to be dominated by the component and structural features of domains.[6,15,16] Therefore, the identical EL spectra before and after the constant-current measurement could indicate no transformation inside the domain during the decay of EQEs.

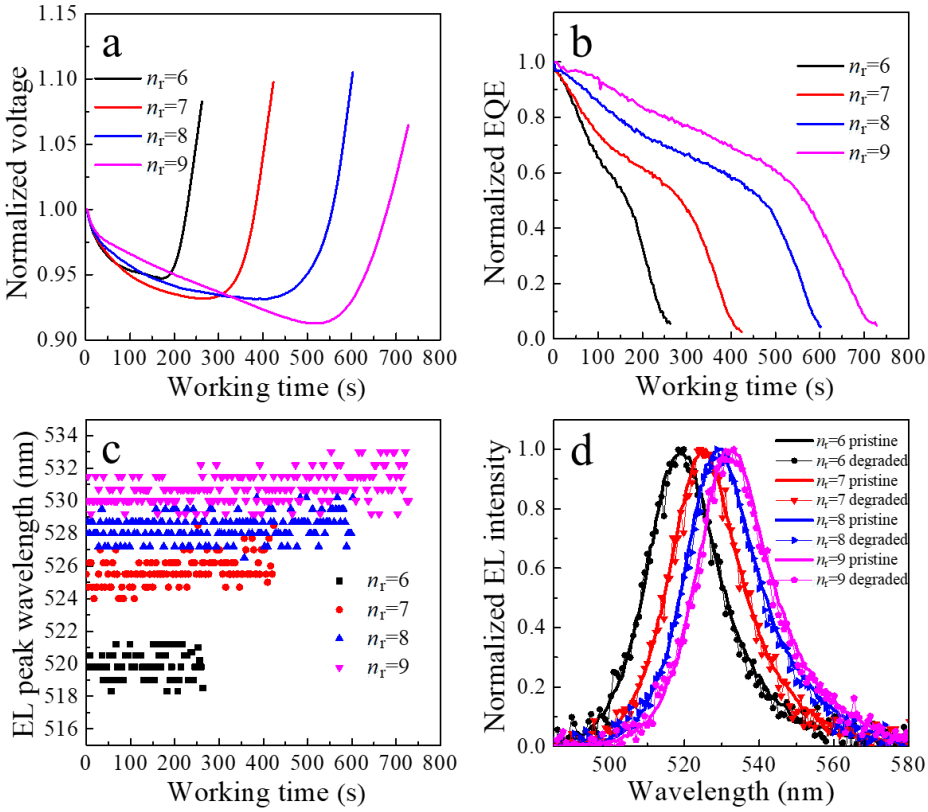

Figure 3-1. Evolution of (a) voltages, (b) EQEs, and (c) EL peak wavelengths of PeLEDs under constant-current operation at 0.25 mA cm^{-2}. (d) Normalized EL spectra of PeLEDs before and after the constant-current measurement.

3.2.2 Influenced Domain Passivation by Ion Migration

Interestingly, I found a recovery behavior of the device performances in the constant-current lifetime measurement. As shown in Figure 3-2a, the constant-current measurement of

an n_r = 9 device was broken off at 214, 462, and 633 s. A rest time of 10 min was taken in each break off. Compared with the data obtained from the devices under continuous driving, there was a significant recovery of the voltage after each rest. Meanwhile, recoveries of EQE after the rests at 214 and 462 s were also found. However, in the rest at 633 s, when the decay came to the second stage, EQEs would no longer recover. Figure 3-2b shows the results of TRPL obtained before the constant-current measurement, at the beginning of each abovementioned rest, and just after the constant-current measurement. The data was fitted with tri-exponential fitting. I found that the f_1, which is the fraction of the defect-induced quenching, increased during the constant-current test, which should be a result of increased defect-state density.[12] The similar recovery behavior and trend of TRPL were also found in the devices with other n_r (Figure A-9, Appendix).

The recovery processes of the voltages and EQEs during a rest in the first stage were further confirmed in Figure 3-2c. During the rest, voltages and EQEs were collected, not continuously, but time-by-time between long intervals, to avoid aging the device. Gradual increases of the voltages and EQEs were found as expected. The performance recovery was also reported by papers on perovskite solar cells,[17,18] and was attributed to the ion migration processes in perovskite films, because the ions tend to drift back to the original positions during the rest under the driving of build-in fields. Therefore, I suppose that the decay mechanisms of PeLEDs are also closely related to the ion migration. Under a reverse bias, the PeLED EQE recovery was found to be accelerated (shown in Figure A-10, Appendix), confirming the recovery mechanism of ions drifting back under build-in fields. In Figure 3-2a, when the operation restarted after the rests, the EQE and voltage values quickly approached the symbol plot curves measured with the continuous operation. This might be ascribed to the fact that, once the ions are migrated under bias, they are mobilized, and easier to migrate if they are driven by voltage again. Together with the abovementioned results that there were no

component and structural changes inside the domains and that the defect density was increased during the constant-current measurement, I deduce that the EQE decay is partially induced by the migration of FA^+ and PEA^+ ligands attached on the domain boundaries, leading to a gradual failure of defect passivation and thus the efficiency decrease. This inference is reasonable because grain boundaries are a main channel for ion migration in perovskite films.[13,19–21] The activation energy of FA^+ migration in perovskites was estimated by density functional theory (DFT) calculation to be 0.5 eV.[22] Besides, the dissociation energy of PEA^+ from the quasi-2D perovskite structure was calculated by DFT to be 3.988 eV.[23] However, the abovementioned calculation results were both based on bulk perovskite models. For ion migration through domain boundaries with defects, the activation energies should be much smaller (roughly halved) compared with in bulk structures.[14] Since FA^+ migration was experimentally confirmed in perovskite solar cells under driving voltages less than 1 V,[19,24] and the PeLED degradation based on the PEA^+ dissociation was also reported,[19,23,24] it is rational to propose that FA^+ and PEA^+ are the ions that migrate through the domain boundaries.

To further confirm that the degradation of the perovskite films is attributed to the reduced domain-boundary passivation, the carrier-trap states were studied with a technique of thermally stimulated current (TSC) measurement.[25] As shown in Figure 3-2d, the devices before and after the EQE decayed to the second stage both exhibited a single TSC peak at around 100 K. Based on a previous report,[22] the trap depth (E_T) can be calculated using the following equation,

$$E_T = k_B T_m \ln\left(\frac{T_m^4}{\beta}\right) \qquad (3-1)$$

where k_B is the Boltzmann's constant (8.617×10^{-5} eV K^{-1}), T_m is the temperature of the TSC peak, and β is the heating rate (5 K min^{-1}). As a calculation result, E_T was 0.14 eV in both pristine and degraded devices. Figure 3-2d also shows that the shape of the TSC curves stayed unchanged, but the TSC intensities remarkably increased after the EQE decay. Since the defects

in pristine perovskite films are mainly located on the grain boundaries,[26,27] I further proved that the grain-boundary defect (which should be the vacancy of mobile ion) increases in density, and the formation of other types of defects is not pronounced with the perovskite degradation in PeLEDs. The trap density (N_T) can be calculated with the following equation.[22]

$$N_T = \frac{2Q}{qAL} \qquad (3-2)$$

where Q is the quantity of charges released during the heating process, which can be obtained by integrating the TSC curve over the heating time, q is the elementary charge, A is the device working area, and L is the perovskite film thickness. As a result, the N_T before and after the EQE degradation are calculated to be 9.68×10^{16} cm^{-3} and 3.44×10^{17} cm^{-3}.

The early theoretical calculation studies on the DFT models of bulk perovskites usually took the vacancies of organic cations as benign defects, which do not trap carriers.[28,29] However, experimental results indicated that the migration of organic cation through perovskite domain boundaries could induce increased quenching centers and severely deteriorated device performances.[24] More specifically, exposed, undercoordinated halogen anions (or organic cation vacancies) on perovskite crystal boundaries were found to act as hole traps in solar cells.[30] This might be a result of the complex conditions of the dangling bonds and lattice distortion on the domain boundaries. Since the domain boundary defects in our case are supposed to the negatively charged organic cation vacancies, which are accepter traps, the trap state energy level should be 0.144 eV above the top of the valance band of the perovskite.

However, the perovskite degradation should not be the only source for the EQE decay. I measured the PL of the working area of an n_r = 9 device at 0, 310 and 685 s of the constant-current measurement. The PL peak areas were used as an indicator of the PLQYs. The evolutions of PLQYs and EQEs are compared in Figure 3-2e. The relative PLQYs dropped to almost the same percentage as EQE did from 0 to 310 s, indicating that the decay of perovskite PLQYs is the main factor for the EQE decay in the first stage. However, EQEs dropped to 17%

of the original value at 685 s, while the PLQY still remained 48 % of the original value, meaning that the degradation of other layers beside the perovskite layer also influences the EQE decay in the second stage, which is possibly related to the irreversibility of EQE. The PL spectra stayed invariable during the decay (Figure 3-2f) even when shown in logarithmic scale (Figure A-11, Appendix), which supports that no degradation inside the domains occurred, as mentioned earlier.

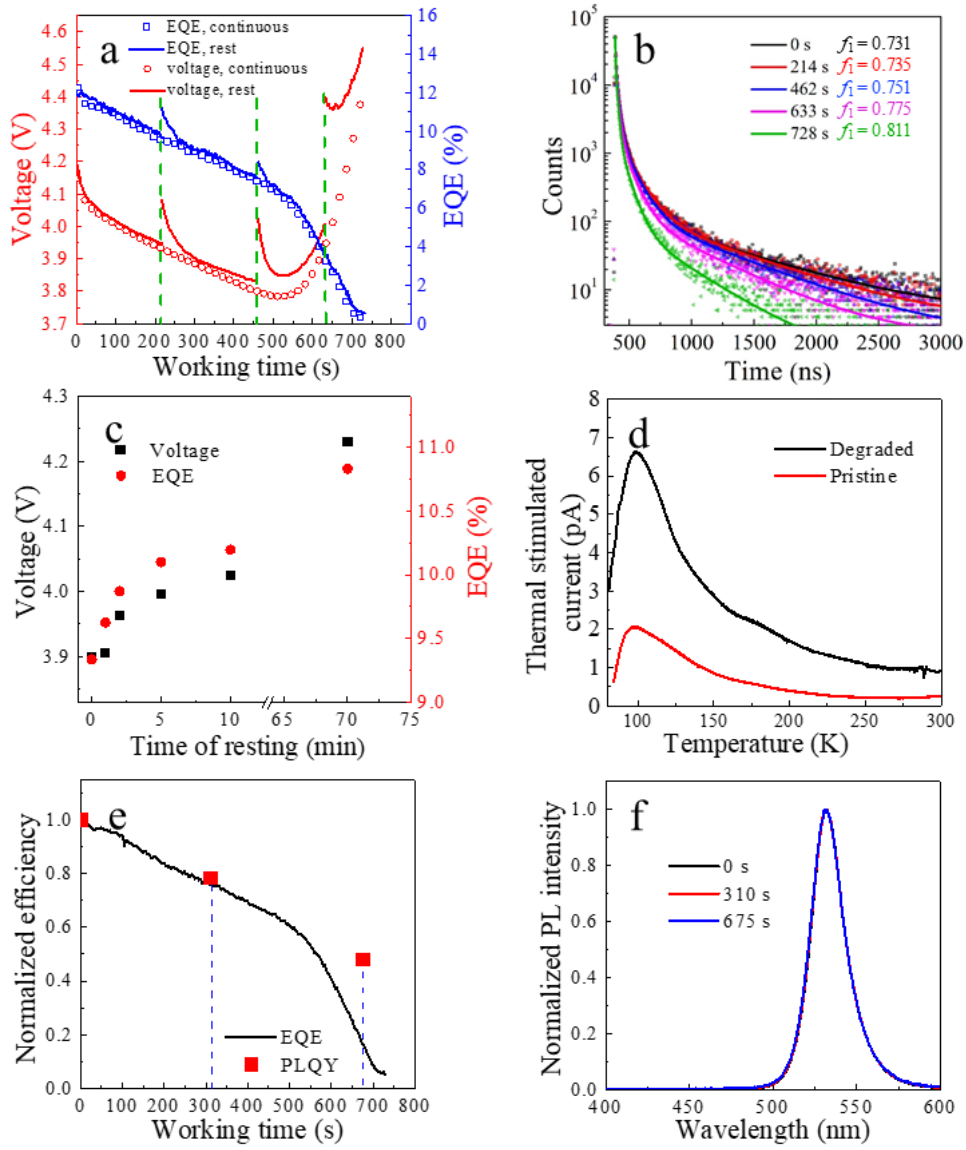

Figure 3-2. (a) Voltage and EQE evolutions of n_r = 9 PeLEDs under continuous constant-current operation without and with rests in certain operation times. (b) TRPL results (dots) along with fitting curves of an n_r = 9 PeLED measured in the rest times in Figure 3-2a. The calculated f_1 are displayed in the figure. (c) Discretely collected voltages and EQE values during a rest at 300 s of the constant-current operation. (d) TSC patterns of an n_r = 9 PeLED before

and after the constant-current measurement. (e) EQE and PLQY evolutions of an n_r = 9 PeLED. (f) Normalized PL spectra corresponding to the PLQY measurement points in (e).

3.2.3 Efficiency Roll-off and Overshoot Influenced by Ion Migration

The EL kinetics in PeLEDs was studied under pulse voltage driving. Square-wave voltages of amplitudes ranging from 5.3 to 17.6 V with the duration from 300 to 5 ms were applied on an n_r = 9 device. The suitable pulse duration was chosen for each voltage value to obtain the complete trends of current, EL intensity, and efficiency, but without aging the device. The current responses of all the driving conditions are shown in Figure A-12 of the Appendix part. As shown in Figure 3-3a, during the applying of a 6-V voltage for 300 ms, the current and luminance kept rising, while the EQE firstly increased and then became constant at 14.5 %. The currents under other voltages also had a trend of increasing during pulses of millisecond timescale, with the EQE increased and stabilized (Figure A-13, Appendix). The increasing of current during the pulse could correspond to the voltage drop during the first stage of the constant-current lifetime measurement. With the EQE in the stable stage of each pulse voltage, a curve of pulse-driving EQE versus current density can be derived. Since the aging of devices can be ignored in the pulse duration with millisecond timescale, the pulse-driving EQE excluded the influence from device degradation. As shown in Figure 3-3b, the pulse-driving EQE had a milder roll-off compared with that of DC-driving EQE, for both n_r = 9 and n_r = 6 devices. Besides, a higher maximum EQE can be obtained through pulse driving, with 15.1% for n_r = 9. This result reflects the roll-off behavior of DC-driving EQE is impacted by ion-migration induced passivation deterioration. The difference between DC-driving and pulse-driving EQEs is more significant in n_r = 6 devices than in n_r = 9 devices. This is possibly because n_r = 6 devices suffer more from the migration of ions at domain boundaries because a perovskite with a higher concentration of PEA^+ (lower n_r in this case) tend to contain smaller domains with larger boundary-surface areas.[12] The severer ion migration from the larger

boundary surface also causes the faster degradation of PeLEDs with lower n_r, as shown in Figure 3-1a and 3-1b. To exclude the factor of different electric field intensities on the perovskite layer with different n_r in the constant-current driving, I also compared the PeLED performance evolutions under constant-voltage driving. As shown in Figure A-14a and A-14b of the Appendix part, even working under the same driving voltage, the devices with lower n_r still suffered from obviously severer degradation, which emphasizes the important role of domain boundary surface and ion migration in device degradation.

The current dynamics under pulse voltage of PeLEDs before and after the EQE decayed to the second stage were found different. During the applying of a 7.5-V voltage for 30 ms, the current of the degraded device increased slower than the pristine one (Figure 3-3c). Furthermore, both of the pristine and degraded devices generated a small reverse current of over 10 ms after cutting off the voltage (Figure 3-3c inset). According to a previous report,[15] the parasitic capacitance caused by ion migration could lead to charging or discharging over a timescale of milliseconds. The reverse current mentioned above is clearly a behavior of discharging. Since the pristine device released a discharging current higher than the degraded device did, there should be a higher parasitic capacitance and thus stronger ion migration in the pristine device. The difference in parasitic capacitance was also evidenced by the results of AC impedance spectra (Figure A-15, Appendix), in which the capacitance value in the equivalent circuit of PeLEDs can be calculated.

Another interesting phenomenon observed from the EL kinetics with the short pulse excitation is the so-called overshoot effect. As shown in Figure 3-3d, after the termination of a 50 μs-long voltage pulse, the EL intensity exhibited a sharp increase. The overshoot effect was also reported in previous papers on PeLEDs,[9,31] and was finely explained. In this case, when the applied voltage is 0 V (during the pulse interval), the alignment of the Fermi levels of all device structures generate the intrinsic build-in field (E_{bi}) though the device pointing from the

cathode to the anode, tilting the energy bands, as shown in Figure A-16a of the Appendix part. The mobile FA^+ and PEA^+ cations on the domain boundaries tend to accumulate on the HTL (hole transport layer)/perovskite interface under the driving of E_{bi}. This accumulation of cations generates an extra electric field (E_c) inside the perovskite layer screening E_{bi}, and induces band bending at the interfaces of the perovskite layer (Figure A-16b, Appendix). When a voltage pulse is applied on the device, because of the energy band tilting induced by all the electric fields, together with the band bending at the interfaces, potential pockets near the interfaces are formed, which are spatial regions with a locally extreme potential value that trap injected carriers (Figure A-16c, Appendix). When the voltage is removed, the trapped holes and electrons are released and recombine in the perovskite layer in a very short timescale, producing the overshoot emission (shown in Figure 3-3e). However, if the applied voltage pulse has large intensity or long duration, the mobile cations might noticeably migrate to the ETL. The gradually released gathering of cations can relieve the band bending, and thus shallow the potential pockets. Therefore, the overshoot effect would be weakened. When the migration of cations to the ETL is intense enough, the aggregation of mobile cations happens on the perovskite/ETL interface, creating strong potential drops at the interfaces, which further reduces the possibility of overshoot (Figure A-16d, Appendix). The gradually weakened overshoot with stronger or longer voltage pulse was observed, as shown in Figure 3-3d and Figure A-17 of the Appendix part. Similarly, the overshoot effect was absent in Figure 3-3a after the 300-ms pulse, which was also a result of limited resolution.

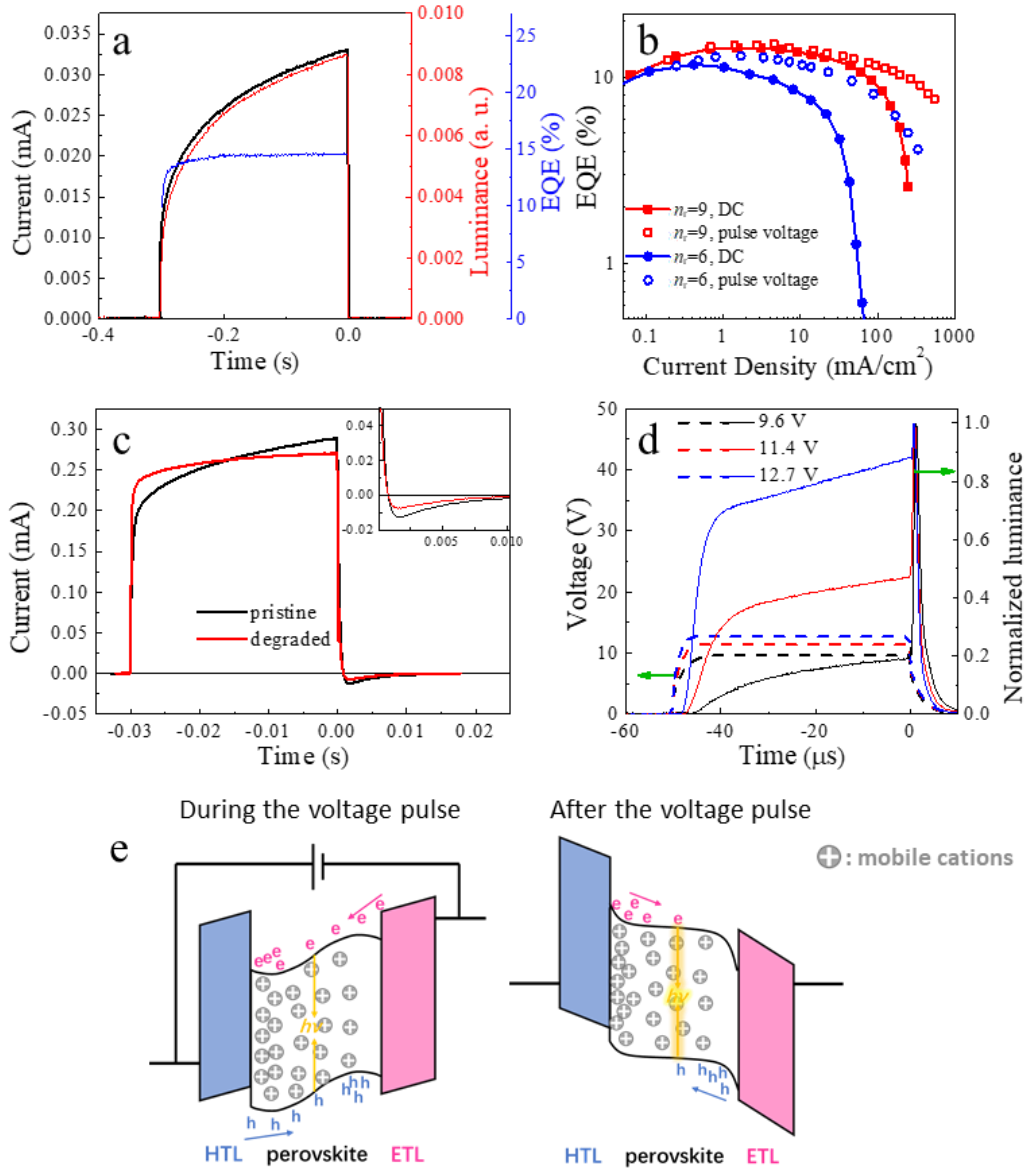

Figure 3-3. (a) Current, luminance, and EQE kinetics of an n_r = 9 PeLED during a voltage pulse of 6 V and 0.3 s. (b) EQE versus current density data of n_r = 6 and n_r = 9 PeLEDs under DC and pulse operations. (c) Current kinetics of an n_r = 9 PeLED before and after the constant-current measurement. The data was collected during a voltage pulse of 7.5 V and 0.03 s. Inset shows the enlarged figure around 0 s. (d) Voltage pulse durations and the corresponding luminance evolutions of an n_r = 9 PeLED. (e) Potential energy diagrams illustrating the charging and releasing processes in a PeLED.

3.2.4 Degradation of the Electron Transport Layer Induced by Mobile Cations

As mentioned in the analysis of Figure 3-2e, the EQE decay of PeLEDs during constant-current driving involves the degradation of other layers besides the perovskite layer. To find if any charge-transporting layer adjacent to the perovskite layer was influenced during operation,

single-carrier devices were fabricated, with the architectures shown in Figure 3-4a and 3-4b. For hole-only devices (HODs), the device architecture was glass substrate/ITO (50 nm)/PVK (30 nm)/perovskite (60 nm)/α-NPD (10 nm)/MoO_3 (10 nm)/Al (100 nm), in which α-NPD stands for *N*,*N*′-di(1-naphthyl)-*N*,*N*′-diphenyl-(1,1′-biphenyl)-4,4′-diamine, as shown in the inset of Figure 3-4a. For electron-only devices (EOD), the device architecture was glass substrate/ITO (50 nm)/SnO_2 (30 nm)/perovskite (60 nm)/TPBi (40 nm)/LiF (1 nm)/Al (100 nm). The low valence band edge of SnO_2 and the high-work function of MoO_3 efficiently blocked the hole injection into EODs and the electron injection into HODs, which can be evidenced by the absence of EL from these devices, indicating completely unipolar current flow through these devices. Both EODs and HODs were driven at a current density of 0.25 mA cm^{-2}, and their $J-V$ curves were collected before and after the constant-current driving. I found that the voltages on HODs only exhibited a very limited decrease during the constant-current driving of over 400 s (Figure A-18, Appendix). Also, $J-V$ properties of HODs varied little after the driving (Figure 3-4a). However, EODs experienced a larger increase in voltage after the constant-current driving, which shares a similar trend with that of PeLEDs, in only 100 s. Remarkable differences in $J-V$ curves of EODs before and after the driving were also found; the current densities in a high voltage region obviously decreased after the constant-current driving (Figure 3-4b). A perovskite-only device with a simple architecture of glass substrate/ITO (50 nm)/perovskite (60 nm)/Au (50 nm) was also fabricated. After driven under a high current density of 2 mA cm^{-2} for over 450 s, $J-V$ properties displayed no change compared with the pristine condition (Figure 3-4c). Those results reflect the fact that the irreversible degradation of PeLEDs is closely related to the deterioration of the ETL, which is TPBi in this case.

In the operations of PeLEDs, the mobile FA^+ and PEA^+ on the domain boundaries tend to migrate to the ETL as mentioned above. Therefore, I infer that the deterioration of the ETL

is a result of the interaction between the mobile cations and TPBi. To evidence this, I studied *J*–*V* properties of TPBi-only devices with an architecture of glass substrate/ITO (50 nm)/TPBi (50 nm)/LiF (1 nm)/Al (100 nm). 5 mol% of PEABr or FABr was doped into the TPBi layer to simulate the cations migrating into the TPBi layer. As shown in Figure 3-4d, the current densities of the PEABr or FABr doped devices were dramatically inferior to those of the pure TPBi device. Therefore, I confirmed that the deteriorated electron transport property of TPBi is from the interaction with FA^+ or PEA^+, which contributes to the irreversible EQE decay in the second stage.

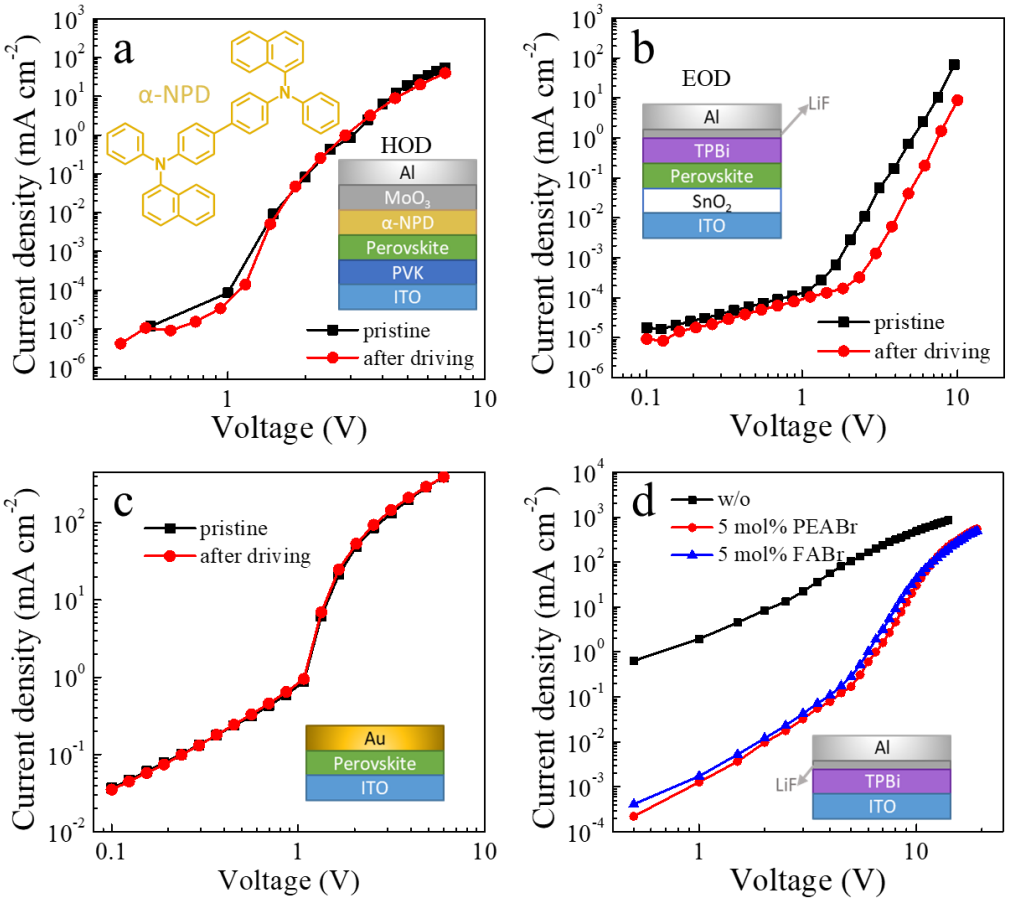

Figure 3-4. *J*–*V* curves of (a) HODs, (b) EODs, and (c) perovskite-only devices before and after the constant-current measurement. (d) *J*–*V* curves of TPBi-only devices without or with PEABr or FABr doping. The inset of (a) shows the chemical structure of α-NPD.

To provide a direct, solid evidence for the migration of organic cations, profile X-ray photoelectron spectroscopy (XPS) measurement was carried out on an n_r = 9 PeLED degraded to the second stage, comparing with a pristine control device. In this measurement, PeLEDs

were sputtered with Ar ions for different cycles, during which certain thicknesses of the device structure were etched off. After each sputtering cycle, XPS results were gathered. The XPS peak intensities of different elements at various sputtering cycles provide the clues of composition distribution along the device thicknesses. As shown in Figure 3-5a, different device structures, which are labeled with different background colors, can be identified from the distribution of elements. The curves of Br 3d and Pb 4f of pristine and degraded devices overlapped well, indicating that there was no redistribution of Br and Pb during the device operation, excluding the irreversible migration of them. The curves of N 1s were hard to quantitatively compare due to their low signal-to-noise ratio. However, the C 1s curves of pristine and degraded devices exhibited a recognizable difference, as shown in Figure 3-5b (the enlarged figure of Figure 3-5a). Compared with the pristine device, the C 1s intensity of the degraded device decreased in the perovskite layer and increased in the TPBi layer, while in the PVK layer it remained unchanged. This result confirms the irreversible migration of organic cations to the ETL. At the 36th sputtering cycle (in the perovskite layer), the largest reduction of C 1s intensity of the degraded device compared with the pristine device was reached, which is 8 %. As introduced in our previous report,[32] the perovskite domain size in an $n_r = 9$ film was 11 nm. In another paper on quasi-2D perovskite,[12] for an 11-nm perovskite domain, about 25 % of the allover organic cations were estimated passivating on the domain boundary. That means at most 32 % of the passivating organic cations left the domain boundary in the degraded PeLED.

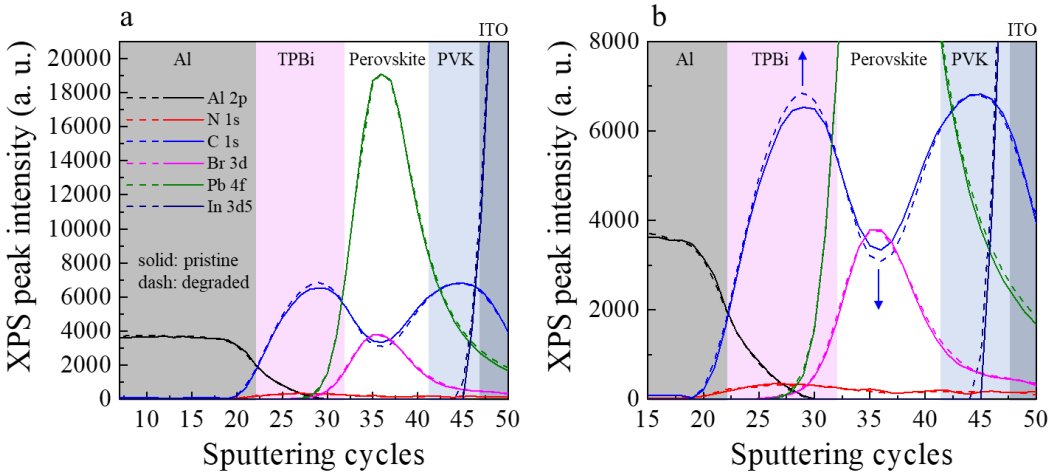

Figure 3-5. (a) Profile XPS peak intensity curves of n_r = 9 PeLEDs before (solid lines) and after (dash lines) degraded to the second stage. (b) Enlarged figure of (a) to show the clear difference of the C 1s curves. The blue arrows point the change directions after the degradation.

The low activation energy of halide anion migration is known in perovskites, implying that the Br^- in our perovskite system may also be mobile. However, this possibility is not supported by the profile XPS results in Figure 3-5. The lack of the trace of irreversible Br^- migration might be attributed to that the Br^- did not interact with and was not trapped in the PVK HTL. Besides, it was reported that the excess injection of a certain kind of carriers could lead to the selection of mobile cations or anions.[33] Specifically, there might have existed an excess injection of holes over electrons in our PeLEDs that facilitated the cations to migrate rather than anions. The excess hole injection can be evidenced by the higher hole current in HODs than the electron current in EODs, as shown in Figure 3-4a and 3-4b.

3.2.5 Deduced Decay Mechanisms of Quasi-2D Perovskite LEDs

Based on the experimental results discussed before, the mechanisms of the two-stage PeLED degradation under constant-current operation can be described by the energy level diagrams shown in Figure 3-6a and 3-6b. In the first stage of degradation, the FA^+ and PEA^+ cations on the domain boundaries migrate towards the ETL under the driving with an external

bias and gradually accumulate on the perovskite/ETL interface. The accumulated cations and the negative charge centers left behind the migrated cations generate extra build-in fields (marked as E_{ebi}) imposed on the carriers going to be injected through the two interfaces of the perovskite film. As shown in Figure 3-6a and 3-6b, the direction of E_{ebi} is favorable for the injection of both holes and electrons, and that is the reason for the voltage decrease in Figure 3-1a. However, the migration of the ligand cations leads to the perovskite domains around the recombination region losing passivation gradually, resulting in the EQE decay. If the driving stops in the first stage, the mobile cations would drift back to their original positions under the intrinsic build in field (E_{bi}). Because E_{bi} should be much smaller than the filed induced by the external driving voltage, the cation aggregation after the rest would not be as intense as during the driving, which means that the domain passivation around the recombination zone would recover to some degree. Furthermore, since the mobile cations would be dispersed or even aggregated on the HTL/perovskite interface under the driving of E_{bi}, the E_{ebi} would be reduced for even inverted after the rest. As a result, the recovery of EQEs and voltages was observed when the constant-current driving restarted.

In the second stage of the PeLED degradation, a large number of the mobile cations penetrate into and are trapped in the TPBi layer. The reduction of the mobile cations that can be driven by E_{bi} is evidenced in Figure 3-3c. The interaction between these organic ammonium cations and TPBi molecules damage the electron transport property of the TPBi layer, which contributes to the voltage rising in Figure 3-1a and results in unbalanced carrier injection. In this way, the recombination zone could gradually approach the ETL side, which makes the injected holes easier to leak to the ETL and increases the opportunity for excitons being quenched by interface traps. That explains why EQEs decayed more severely than PLQYs did in the second stage of degradation, as shown in Figure 3-2e. When the driving stops, the mobile cations drift backwards just as in the first stage. However, since the recombination zone is close

to the ETL and the free mobile cations in the perovskite layer are few, the domain passivation condition around the recombination zone is not improved after the rest, which makes the EQE decay in the second stage irreversible.

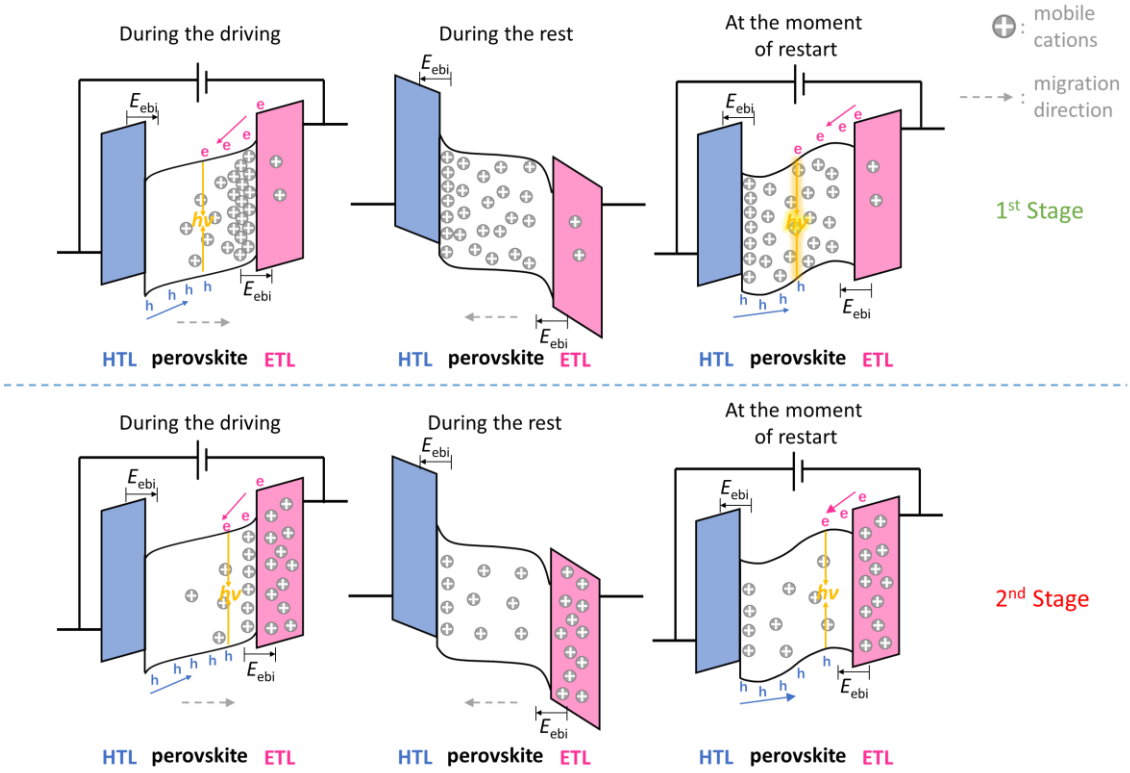

Figure 3-6. Diagrams illustrating the potential alignment, charge injection, positions and motions of mobile cations, and E_{ebi} of PeLEDs in the (a) first and (b) second stages of EQE decay.

3.3 Conclusion

In conclusion, I discussed two stages of EQE decay in the operation of quasi-2D PeLEDs. During the EQE decay process, the main change of the perovskite film was found to be the gradual losing of domain-boundary passivation. Because of the recovery behavior of PeLEDs, this degradation was proposed to be induced by the migration of PEA^+ and FA^+ ligands through the domain boundaries, which was confirmed by the EL kinetics under pulse voltages. The efficiency roll-off behavior was also found to be related to this cation migration. Furthermore, the mobile cations get trapped in the ETL, causing the damage to the electron transport property

of TPBi, which leads to the irreversible decay of EQE in the second decay stage. The mechanisms depicted in this chapter contribute to the comparably short operation lifetimes of quasi-2D PeLEDs, and provide instructive ideas to enhance the lifetimes, such as preventing ion migration, isolating the ETL from interacting with mobile cations in the perovskite, and so forth.

3.4 Experimental

Materials. PEABr, FABr, TPBi, and $PbBr_2$ were obtained as introduced in the Experimental part in Chapter 2. PVK and 18-crown-6 were purchased from Sigma-Aldrich. TPBi and α-NPD were purchased from Lumtec. A SnO_2 colloidal precursor solution (15 wt% in water) was purchased from Alfa Aesar. TPBi was purified using a train sublimation method prior to use, while other materials were used as purchased without purification.

Precursor solution preparation. Quasi-2D perovskite precursor solutions of various n_r were prepared using the LOD precursor composition described in the Experimental part in Chapter 2 with the same experimental conditions.

Device preparation. PeLED devices were fabricated using the same experimental conditions previously described in the Experimental part in Chapter 2

For the HOD fabrication, the fabrication process was the same as that of PeLEDs except the layers vacuum-deposited on the perovskite layer, which were 10-nm-thick α-NPD, 10-nm-thick MoO_3, and 100-nm-thick Al layers.

For the EOD fabrication, a 30-nm thick SnO_2 layer was spin-coated on the clean ITO-coated glass substrates from the precursor solution and annealed in air at 150 ℃ for 15 min. After that, the samples were transferred into a nitrogen-filled glovebox. The fabrication processes of the perovskite layer and the electrode were the same as in the preparation of PeLEDs.

For the fabrication of perovskite-only devices, the perovskite layer was deposited on a clean ITO-coated glass substrate in a nitrogen-filled glovebox. A 50-nm-thick gold layer was then vacuum-deposited on the perovskite layer. The perovskite preparation method and the vacuum-deposition conditions were the same as those in the preparation of PeLEDs.

For the fabrication of TPBi-only devices, after the clean ITO-coated glass substrates were transferred into a nitrogen-filled glovebox, a 50-nm-thick TPBi layer was deposited on this substrate from a TPBi solution in methanol doped with PEABr, FABr, or nothing. Then, 1-nm-thick LiF and 100-nm-thick Al layers were vacuum-deposited successively onto the TPBi layer with the conditions same as those for the preparation of PeLEDs.

Device characterization: The *J–V* and EQE versus current density characteristics, and EL spectra of the devices were measured with the same evaluation methods and equipment previously described in the Experimental part in Chapter 2. The voltage versus working lifetime and EQE versus working lifetime characteristics of devices under constant-current driving were also measured using the same system.

PL spectroscopy measurement: PL spectra of PeLEDs were collected with the same evaluation methods and equipment previously described in the Experimental part in Chapter 2. Only the electric working area on a device was exposed to the excitation light, while other area was cover by black tapes.

TRPL measurement: TRPL results were collected with the same evaluation methods and equipment previously described in the Experimental part in Chapter 2. Only the electric working area on a device was exposed to the excitation light, while other area was cover by black tapes.

Thermally stimulated current measurement. The TSC versus temperature characterizations were carried on PeLEDs using a Rigaku TSC-FETT EL2000 system. The device heating rate during the TSC measurement was 5 K min^{-1}.

Transient EL characteristics: The current density and EL intensity kinetics during a certain voltage pulse were collected using a wave function generator (NF, WF1947), a high-speed amplifier (NF, HSA4101), a fast response photo-multiplier tube (Hamamatsu, R925) with a signal amplifier (Hamamatsu, C6438), and an oscilloscope (Agilent, DSO5034A). The transient EQE was calculated using an n_r = 9 device as a reference. The absolute DC-driving EQE under 4.7 V of this reference device was collected using the integrating sphere system mentioned above. The current density and EL intensity values of the reference device under DC voltage of 4.7 V were also collected with the transient EL measurement system. With the values measured from the reference device, the transient EQE of other samples under pulse excitations can be calculated.

AC impedance measurement: The impedance spectra were collected with an electrochemical comprehensive analysis system (Solartron, Modulab XM). The DC voltage component applied on the PeLEDs was 3.4 V, and the AC voltage component was 30 mV, with the AC frequency swept from 10,000 Hz to 0.1 Hz.

Profile XPS measurement. The profile XPS measurement was carried out on fresh and degraded n_r = 9 PeLEDs in an ultrahigh vacuum chamber with an X-ray photoelectron spectrometer equipped with an Ar gas cluster ion beam gun (PHI 5000 VersaProbe II, ULVACΦ) (Mg Kα source, 1253.6 eV).

3.5 References

(1) Zhao, B.; Bai, S.; Kim, V.; Lamboll, R.; Shivanna, R.; Auras, F., . . . Di, D., *Nat. Photonics* **2018,** *12*, 783-789.

(2) Wang, Q.; Wang, X.; Yang, Z.; Zhou, N.; Deng, Y.; Zhao, J., . . . Huang, J., *Nat. Commun.* **2019,** *10*, 5633.

(3) Li, Z.; Chen, Z.; Yang, Y.; Xue, Q.; Yip, H. L.; Cao, Y., *Nat. Commun.* **2019,** *10*, 1027.

(4) Ban, M.; Zou, Y.; Rivett, J. P. H.; Yang, Y.; Thomas, T. H.; Tan, Y., . . . Sun, B., *Nat. Commun.* **2018,** *9*, 3892.

(5) Cheng, L.; Jiang, T.; Cao, Y.; Yi, C.; Wang, N.; Huang, W.; Wang, J., *Adv. Mater.* **2019**, e1904163.

(6) Yang, X.; Zhang, X.; Deng, J.; Chu, Z.; Jiang, Q.; Meng, J., . . . You, J., *Nat. Commun.* **2018,** *9*, 570.

(7) Jiang, Y.; Qin, C.; Cui, M.; He, T.; Liu, K.; Huang, Y., . . . Chen, J., *Nat. Commun.* **2019,** *10*, 1868.

(8) Watanabe, S.; Cheng, T.; Tumen-Ulzii, G.; Qin, C.; Matsushima, T.; Adachi, C., *Appl. Phys. Lett.* **2019,** *115*, 233502.

(9) Fakharuddin, A.; Qiu, W.; Croes, G.; Devižis, A.; Gegevičius, R.; Vakhnin, A., . . . Heremans, P., *Adv. Funct. Mater.* **2019,** *29*, 1904101.

(10) Zou, W.; Li, R.; Zhang, S.; Liu, Y.; Wang, N.; Cao, Y., . . . Huang, W., *Nat. Commun.* **2018,** *9*, 608.

(11) Chiba, T.; Hayashi, Y.; Ebe, H.; Hoshi, K.; Sato, J.; Sato, S., . . . Kido, J., *Nat. Photonics* **2018,** *12*, 681-687.

(12) Xiao, Z.; Kerner, R. A.; Tran, N.; Zhao, L.; Scholes, G. D.; Rand, B. P., *Adv. Funct. Mater.* **2019,** *29*, 1807284.

(13) Shao, Y.; Fang, Y.; Li, T.; Wang, Q.; Dong, Q.; Deng, Y., . . . Huang, J., *Energ. Environ. Sci.* **2016,** *9*, 1752-1759.

(14) Yuan, Y.; Huang, J., *Acc. Chem. Res.* **2016,** *49*, 286-93.

(15) Yuan, M.; Quan, L. N.; Comin, R.; Walters, G.; Sabatini, R.; Voznyy, O., . . . Sargent, E. H., *Nat. Nanotechnol.* **2016,** *11*, 872-877.

(16) Yuan, S.; Wang, Z. K.; Xiao, L. X.; Zhang, C. F.; Yang, S. Y.; Chen, B. B., . . . Liao, L. S., *Adv. Mater.* **2019,** *31*, e1904319.

(17) Tumen-Ulzii, G.; Qin, C.; Klotz, D.; Leyden, M. R.; Wang, P.; Auffray, M., . . . Adachi, C., *Adv. Mater.* **2020**, e1905035.

(18) Domanski, K.; Roose, B.; Matsui, T.; Saliba, M.; Turren-Cruz, S.-H.; Correa-Baena, J.-P., . . . Abate, A., *Energ. Environ. Sci.* **2017,** *10*, 604-613.

(19) Yun, J. S.; Seidel, J.; Kim, J.; Soufiani, A. M.; Huang, S.; Lau, J., . . . Ho-Baillie, A., *Adv. Energy Mater.* **2016,** *6*, 1600330.

(20) Lee, H.; Ko, D.; Lee, C., *ACS Appl. Mater. Inter.* **2019,** *11*, 11667-11673.

(21) Lee, S.; Kim, D. B.; Yu, J. C.; Jang, C. H.; Park, J. H.; Lee, B. R.; Song, M. H., *Adv. Mater.* **2019,** *31*, e1805244.

(22) Qin, C.; Matsushima, T.; Fujihara, T.; Potscavage, W. J., Jr.; Adachi, C., *Adv. Mater.* **2016,** *28*, 466-71.

(23) Cheng, T.; Qin, C.; Watanabe, S.; Matsushima, T.; Adachi, C., *Adv. Funct. Mater.* **2020,** *30*, 2001816.

(24) Wei, D.; Ma, F.; Wang, R.; Dou, S.; Cui, P.; Huang, H., . . . Li, M., *Adv. Mater.* **2018,** *30*, 1707583.

(25) Qin, C.; Matsushima, T.; Potscavage, W. J.; Sandanayaka, A. S. D.; Leyden, M. R.; Bencheikh, F., . . . Adachi, C., *Nat. Photonics* **2019,** *14*, 70-75.

(26) Zou, Y.; Ban, M.; Yang, Y.; Bai, S.; Wu, C.; Han, Y., . . . Sun, B., *ACS Appl. Mater. Inter.* **2018,** *10*, 24320-24326.

(27) Shao, Y.; Xiao, Z.; Bi, C.; Yuan, Y.; Huang, J., *Nat. Commun.* **2014,** *5*, 5784.

(28) Yin, W.-J.; Shi, T.; Yan, Y., *Appl. Phys. Lett.* **2014,** *104*, 063903.

(29) Yin, W. J.; Shi, T.; Yan, Y., *Adv. Mater.* **2014,** *26*, 4653-8.

(30) Abate, A.; Saliba, M.; Hollman, D. J.; Stranks, S. D.; Wojciechowski, K.; Avolio, R., . . . Snaith, H. J., *Nano Lett.* **2014,** *14*, 3247-54.

(31) Kim, H.; Zhao, L.; Price, J. S.; Grede, A. J.; Roh, K.; Brigeman, A. N., . . . Giebink, N. C., *Nat. Commun.* **2018,** *9*, 4893.

(32) Cheng, T.; Qin, C.; Watanabe, S.; Matsushima, T.; Adachi, C., *Adv. Funct. Mater.* **2020,** *30*, 2001816.

(33) Lin, Y.; Chen, B.; Fang, Y.; Zhao, J.; Bao, C.; Yu, Z., . . . Huang, J., *Nat. Commun.* **2018,** *9*, 4981.

Chapter 4

Conclusion and Perspective

Quasi-2D PeLEDs have earned much attention from researchers because of their rapidly improving EQEs. However, how the structural properties (multi-*n* configuration, domain passivation effect, and etc.) of quasi-2D perovskite films affect the emission properties remains controversial. Besides, quasi-2D PeLEDs reported by far still had short working lifetimes and severe EQE roll-off, for which the mechanisms need investigation.

The work presented in this thesis reports on the essential factors impacting the emission efficiencies and working lifetimes of quasi-2D PeLEDs and the mechanisms of how these factors work.

4.1 Conclusion

In **Chapter 2**, I systematically investigated how the stoichiometric engineering impacts the defect passivation and domain distribution of quasi-2D perovskites to understand the influence to the emission efficiencies. By tuning the ratio of perovskite precursors, not only the *n* of the emission domains was changed, but also the non-emission low-*n* domains were controlled. These low-*n* domains were further proved unfavorable for obtaining efficient emission of quasi-2D perovskites.

As a result, in perovskite films prepared from stoichiometric quasi-2D precursor compositions, large organic ammonium cations function well as passivators. In comparison, compositions of simply adding a large organic halide salt into the 3D perovskite precursor ensure not only the defect passivation but also the effective formation of quasi-2D perovskite domains, with avoiding unfavorable low-*n* domains appearing, ending up with remarkably high exciton binding energies. Quasi-2D perovskite films fabricated with a well-designed precursor composition achieved a high PLQY of 95.3% and an EQE of 14.7% in LEDs

In **Chapter 3**, I discussed the mechanism of the degradation and EQE roll-off on the basis of ion migration. From the trends of EQE and voltage evolutions, two device decay stages with

different mechanisms were found. The recovery behaviors of the quasi-2D PeLEDs indicate that some ion migration dominates the EQE decay. The migrated ions were then discovered to be ammonium cations attached on the domain boundaries, and their migration was also responsible for the severe EQE roll-off.

As a result, I conclude that the migration of ligand cations through domain boundaries of quasi-2D perovskite films induces the gradual losing of defect passivation at the boundaries, which results in the reversible PeLED degradation and severe EQE roll-off. When the device operation time is long, the mobile cations enter and interact with the electron transport layer, leading to the stage of irreversible PeLED degradation. The device degradation mechanisms we discovered here are constructive for developing quasi-2D PeLEDs with smaller efficiency roll-off and better operational durability.

4.2 Perspective

With the results and conclusions reported in this thesis, future researches can be conducted to achieve higher EQE of PeLEDs. In Chapter 2, I found the defect passivation on grain boundaries is of great importance in enhancing the devices' EQEs. Therefore, more effective passivating molecules could be designed and synthesized as a dopant to perovskite films to get more complete defect passivation. Moreover, the domain-controlling methods by stoichiometric engineering as introduced in Chapter 2 might be useful to improve the overall performances of blue PeLEDs.

For conventional 3D perovskites, blue emission can only be obtained in involving Cl^- ions. However, the low solubility and structural instability of Cl-based perovskites impede the developing of corresponding high-performance LEDs. Recent progresses on the research of high-efficiency blue PeLEDs relied very much on quasi-2D configuration, in which sufficient quantum size effect was achieved on a Br-based perovskite for realizing blue emission.[1–3]

However, the performances of these blue PeLEDs have still been much inferior to those of red and green PeLEDs by far. Furthermore, most of the high-efficiency blue PeLEDs based on quasi-2D perovskites have EL peaks centered around 480~490 nm, which corresponds to sky blue color rather than blue,[2] as shown in Figure 4-1a and 4-1b.

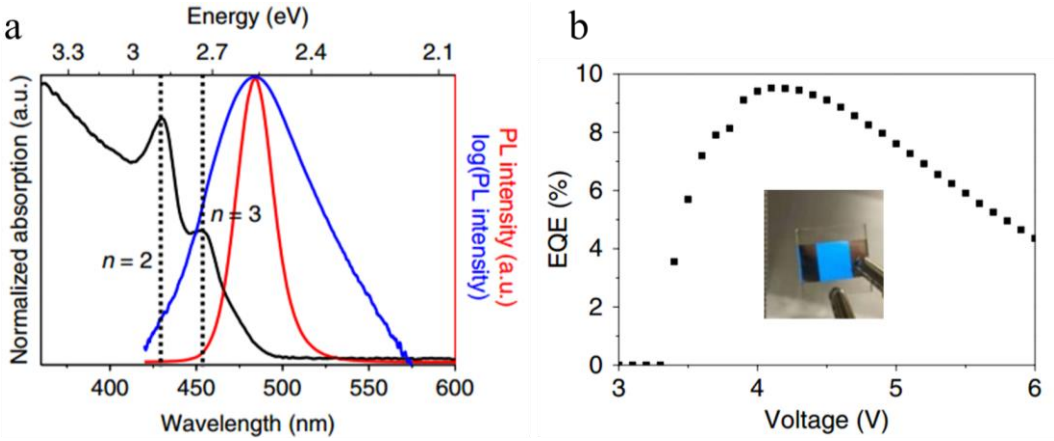

Figure 4-1. (a) Absorption and PL spectra of a typical quasi-2D perovskite film. The black, red, and blue lines represent the absorption, PL spectrum, and the PL spectrum with the intensity shown in logarithmic scale, respectively. (b) EQE versus voltage data of the corresponding LED device. The inset of Figure 4-1b is the working picture of a sly-blue PeLED. This figure is reproduced from ref. 2.

In my opinion, the moderate performances of blue quasi-2D PeLEDs are closely related to the multi-*n* configuration introduced in Chapters 1 and 2. To obtain blue emission with the wavelength centered near 460 nm, the quasi-2D perovskite of about $n = 3$ should be used. However, in the film deposited from an $n_r = 3$ precursor solution, domains of the $n < 3$, $n = 3$, and $n > 3$ coexist. Emission from the $n > 3$ domains with narrow bandgaps would predominate (shown in Figure 4-2a), which is red-shifted compared with the emission from the $n = 3$ domains. Besides, since the $n = 1$ and $n = 2$ domains are unfavorable for the emission efficiency as mentioned in Chapter 2, high EQE of the LEDs is hard to reach.

Although pure-*n* quasi-2D perovskites are hard to achieve with solution processing, the methods of concentrating the *n* distribution still exit. Using the LOD precursor compositions (with less PbX_2 compared with ideal stoichiometry) introduced in Chapter 2, the formation of unfavorable $n = 1$ and $n = 2$ domains could be suppressed. In the case of $n_r = 3$, the average

domain *n* should be near 3, which means reducing the low-*n* domain also limits the formation of domains with *n* higher than 3, which is proved valid with the more blue-shifted PL peaks of LOD films than those of ST films (Figure 2-3e). On the other hand, the low-*n* domains are generated in the early stage of the film formation, which is always before the annealing process, while the high-*n* domains are mostly formed during annealing.[4] Therefore, some techniques that can promote the rapid and simultaneous formation of perovskite crystallization nuclei, such as hot-casting,[5] can further concentrate the *n* distribution. In the best cases, the preparing of nearly pure $n = 3$ perovskite films is supposed to result in much enhanced emission efficiencies and further blue-shifted emission peaks, as shown in Figure 4-2b.

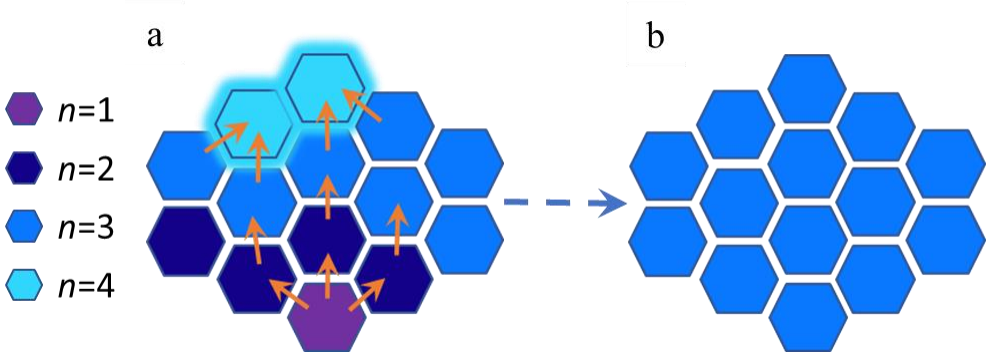

Figure 4-2. (a) Scheme of the multi-*n* configuration of a quasi-2D perovskite film prepared from an $n_r = 3$ precursor solution. (b) Controlled *n* purity for efficient blue emission.

In Chapter 3, I found that the migration of cations on the domain boundaries and their interaction with a TPBi layer induces PeLED degradation. This degradation mechanism of quasi-2D PeLEDs might inspire ideas to enhance the working lifetimes and relief the efficiency roll-off by preventing the ion migration. The potential strategies for suppressing the influence of the ion migration include following methods:

1. Increasing domain size for smaller domain boundary area.
2. Fill the domain boundaries with other dopant molecules that can suppress the ion migration.
3. Adding an ion blocking layer between the perovskite layer and the electron-transporting layer.

4. Introducing large organic ammonium cations which have a stronger interaction with the domain boundaries to increase the energy required for the detaching of the cations.

Furthermore, using a further modified quasi-2D perovskite with high PLQY, high exciton binding energy, high structural and optoelectronic durability, low-threshold lasing of various color might be obtained based on the findings in this thesis. If the high charge-transporting capability of perovskite materials can be retained at the same time, electrically pumped perovskite lasing is possible to achieve, which would largely broaden the application of perovskites and open up new research fields.

4.3 References

(1) Wang, Q.; Wang, X.; Yang, Z.; Zhou, N.; Deng, Y.; Zhao, J., . . . Huang, J., *Nat. Commun.* **2019,** *10*, 5633.

(2) Liu, Y.; Cui, J.; Du, K.; Tian, H.; He, Z.; Zhou, Q., . . . Jin, Y., *Nat. Photonics* **2019,** *13*, 760.

(3) Li, Z.; Chen, Z.; Yang, Y.; Xue, Q.; Yip, H. L.; Cao, Y., *Nat. Commun.* **2019,** *10*, 1027.

(4) Sun, Y.; Zhang, L.; Wang, N.; Zhang, S.; Cao, Y.; Miao, Y., . . . Huang, W., *npj Flexible Electronics* **2018,** *2*, 1.

(5) Tsai, H.; Nie, W.; Blancon, J. C.; Stoumpos, C. C.; Soe, C. M. M.; Yoo, J., . . . Mohite, A. D., *Adv. Mater.* **2018,** *30*, 1704217.

Chapter 5

Appendix

5.1 Appendix Figures

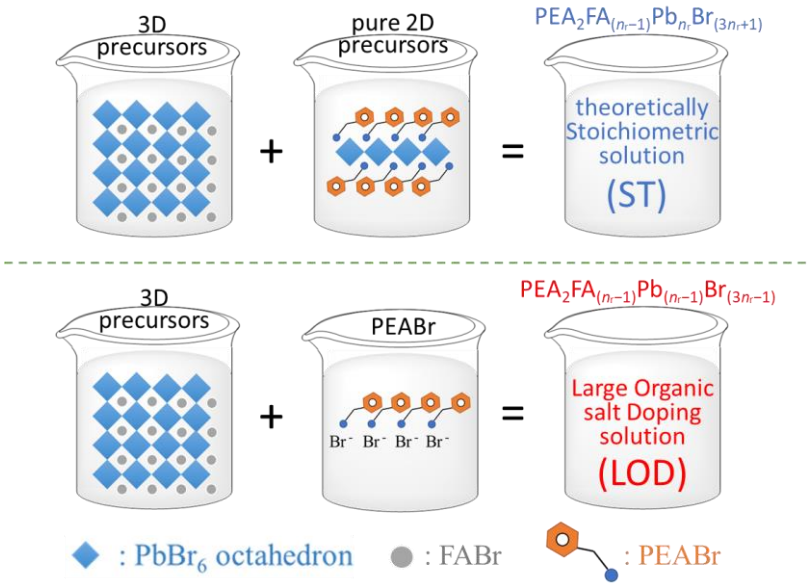

Figure A-1. Illustration showing the preparation of perovskite precursor solutions with ST and LOD compositions. ST solutions were made by mixing the pure 2D PEA_2PbBr_4 and 3D $FAPbBr_3$ perovskite solutions. LOD solutions were made by doping PEABr into the 3D $FAPbBr_3$ perovskite solutions. In the perovskite precursor solutions, all the dissolved components exist as ions.

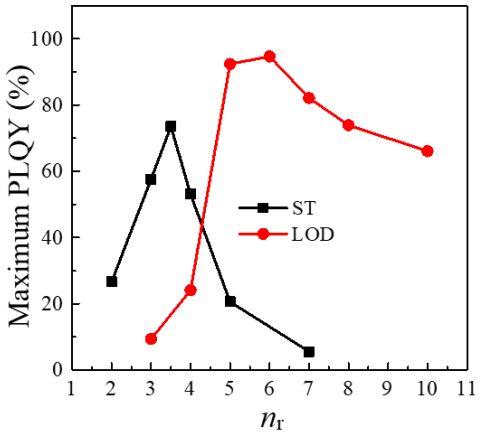

Figure A-2. Plots of the maximum PLQYs obtained at the appropriate excitation fluences as a function of n_r for ST and LOD perovskites films. The maximum PLQY values were taken from Figure 2-4a and 2-4b.

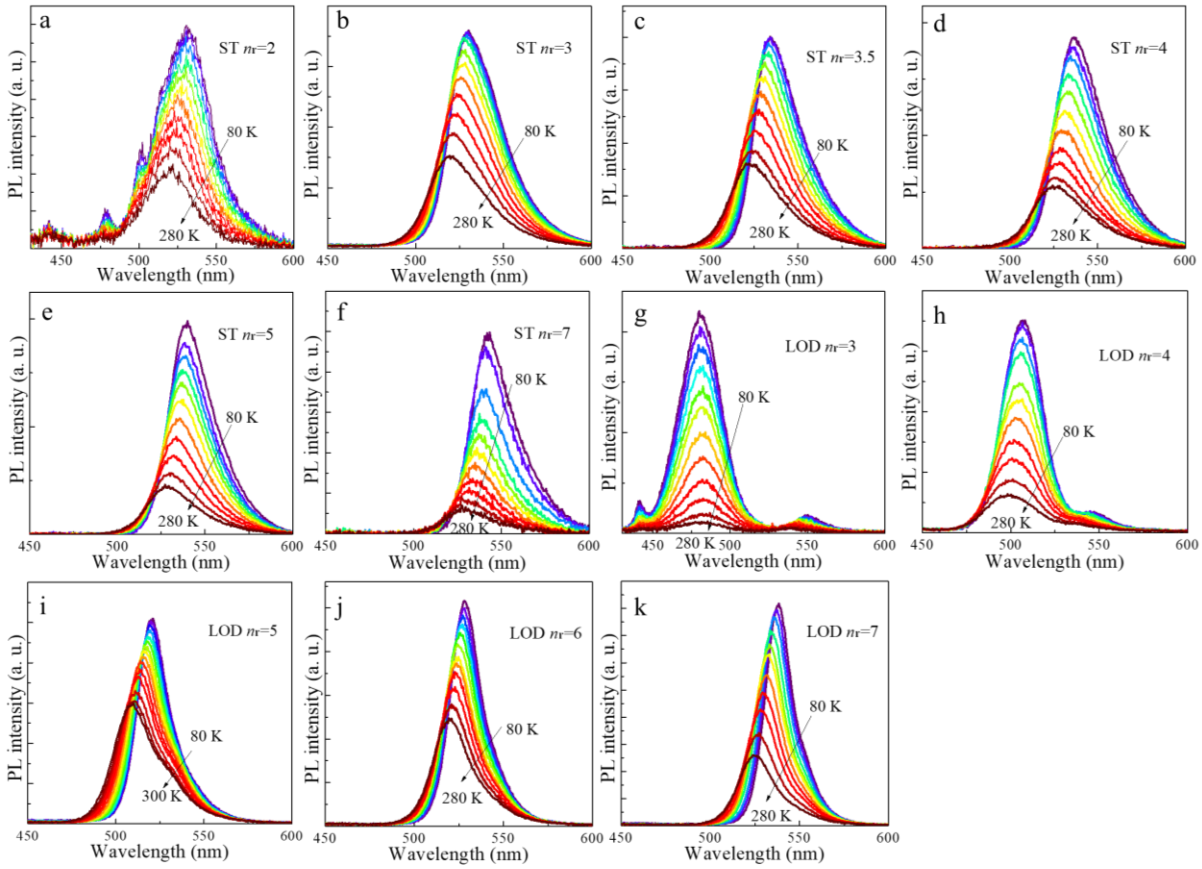

Figure A-3. Temperature-dependent PL spectra of ST and LOD films with various n_r.

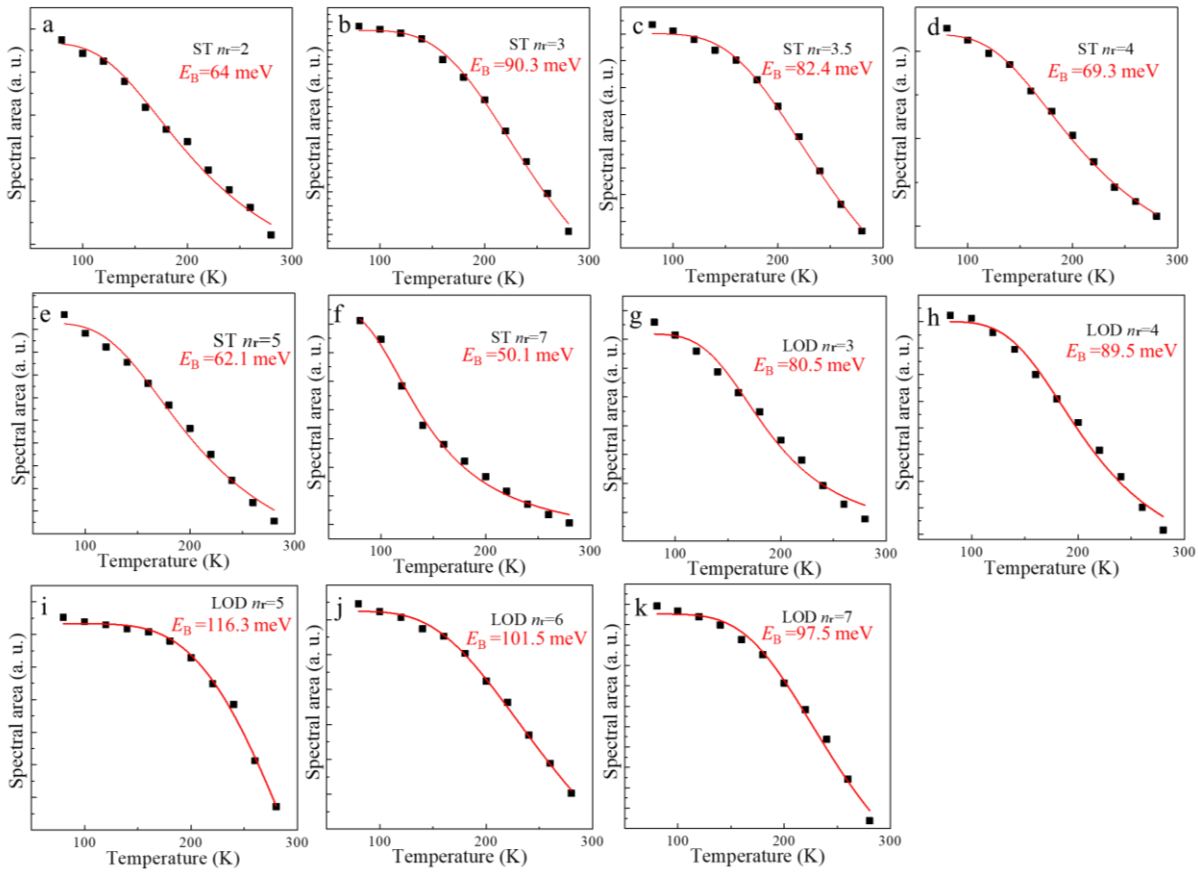

Figure A-4. Plots of areas of PL spectra as a function of temperature for ST and LOD films. The red solid lines represent the results of fitting with Arrhenius equation below. The calculated E_B values can be found in each figure.

Arrhenius equation used above is given by:[1]

$$I(T) = \frac{I_O}{1 + Ae^{(-E_B/k_BT)}} \qquad (A-1)$$

where *I(T)* is the area of the PL spectrum, I_O is *I(T)* at a low temperature of 80 K, and k_B is the Boltzmann's constant.

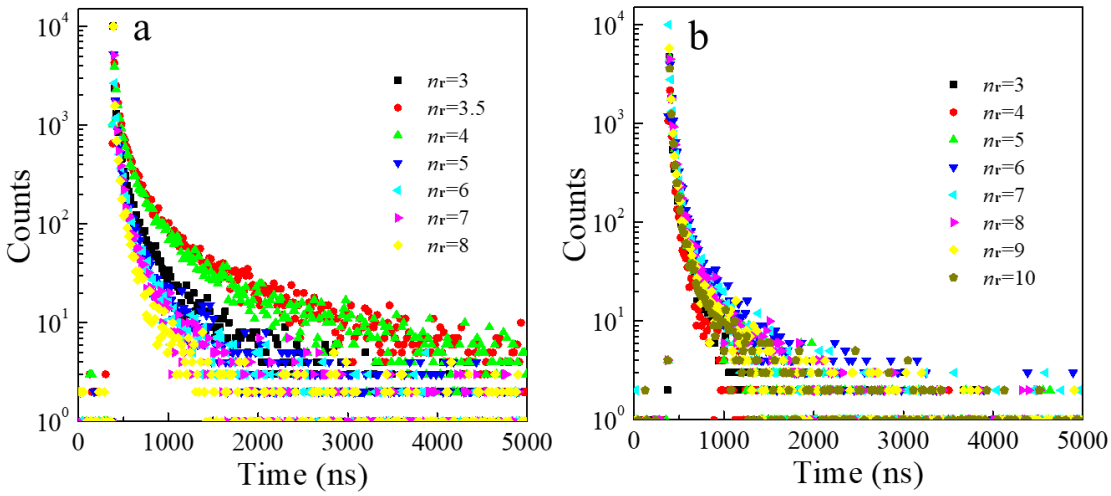

Figure A-5. TRPL results of (a) ST and (b) LOD films.

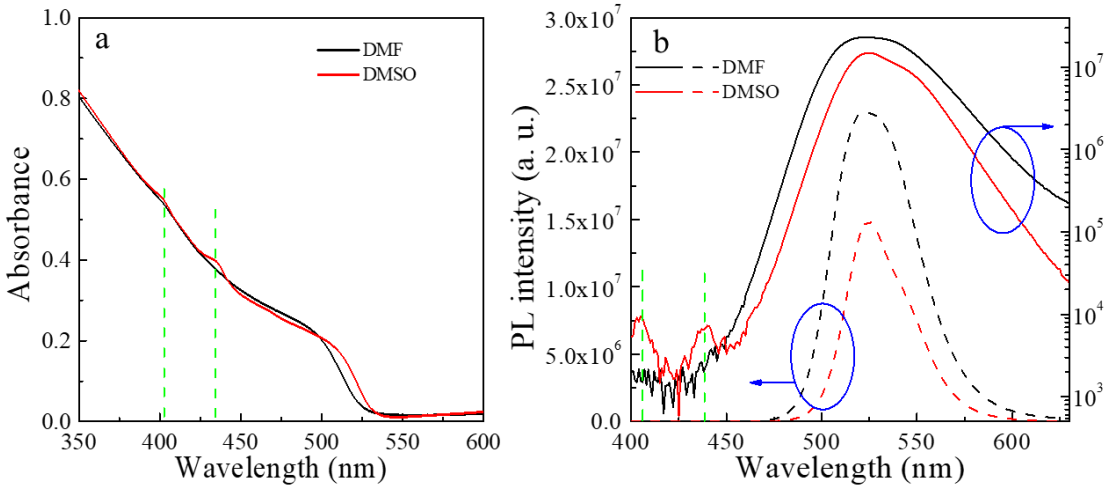

Figure A-6. (a) Absorbance and (b) PL spectra of ST films with an n_r of 5, which were prepared by spin-coating from DMF and DMSO solutions. The *y*-1 and *y*-2 axis scales are respectively linear and logarithmic in (b). The Pb concentration was 0.35 M in a DMF solution and 0.6 M in a DMSO solution. The green dash lines in (b) represent the positions for the n = 1 and n = 2 domains.

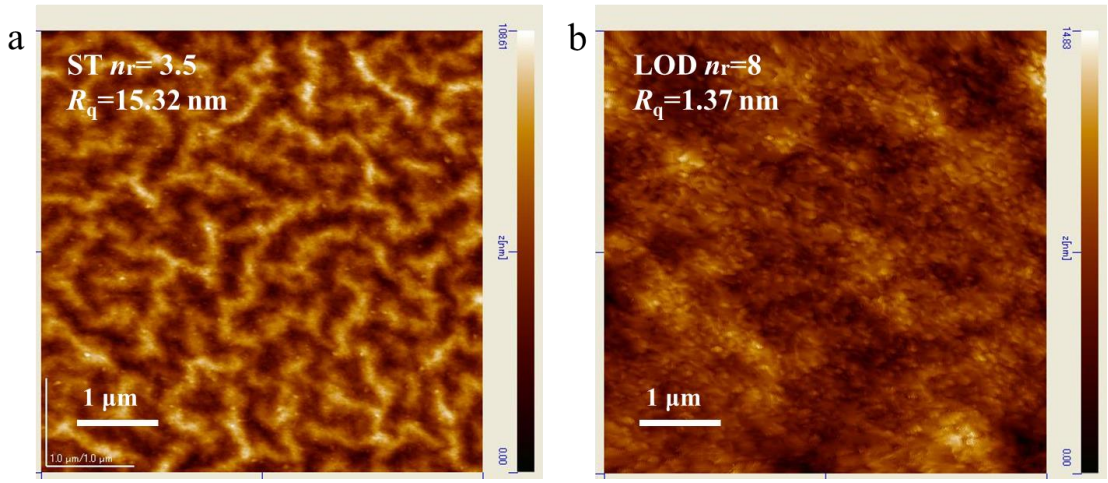

Figure A-7. AFM images of ST and LOD films with n_r = 3.5 and n_r = 8, respectively. R_q stands for the root-mean-square roughness.

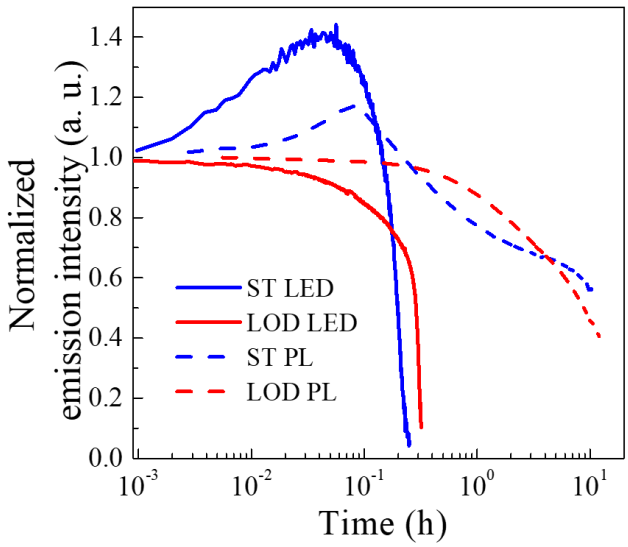

Figure A-8. Evolution of emission intensities of ST and LOD samples with n_r = 3.5 and n_r = 8, respectively. The EL intensities of PeLEDs were recorded under the constant current operation at 0.25 mA cm^{-2}. The PL intensities were recorded under continuous irradiation of excitation light with a wavelength of 365 nm and an intensity of 4.3 mW cm^{-2}.

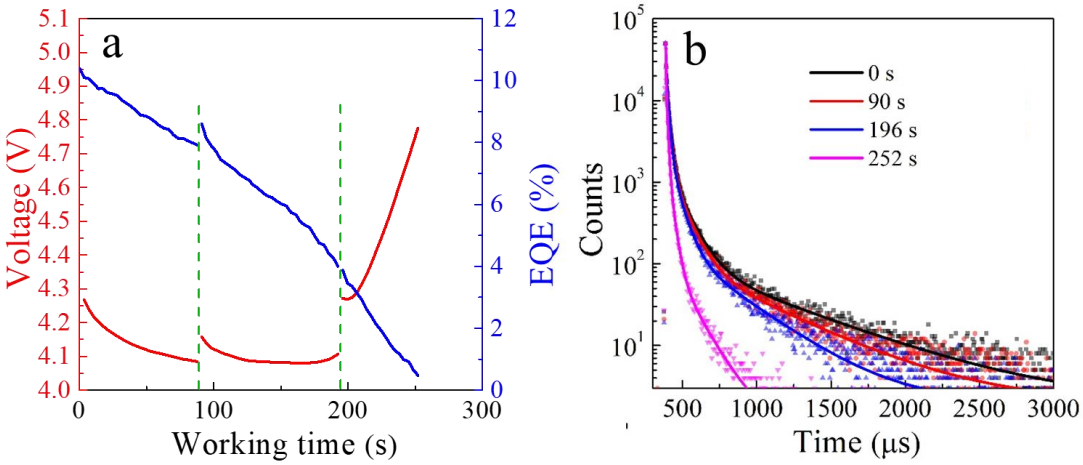

Figure A-9. (a) Voltage and EQE evolutions of an n_r = 6 PeLED under constant-current operation with rests in certain operation times. Each of the rests lasted 10 min. (b) TRPL data (dots) along with fitting curves of an n_r = 6 PeLED measured in the start, end, and rest times in (a).

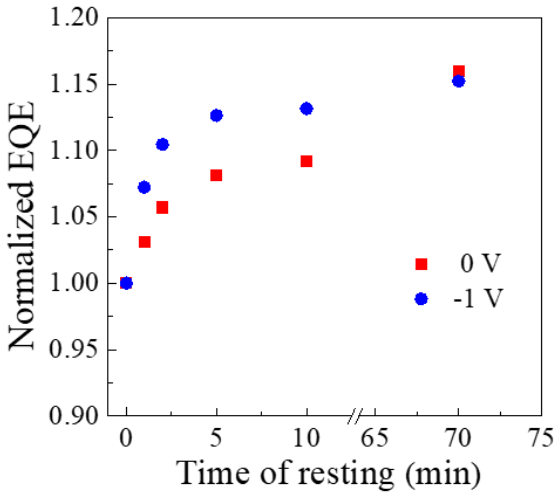

Figure A-10. Discretely collected EQE values of n_r = 9 PeLEDs during a rest at the 300 s of the constant-current operation. During the rest, a voltage of 0 or −1 V were applied to the devices.

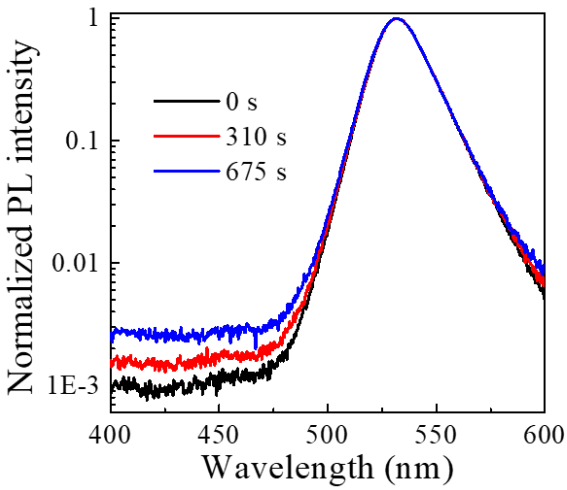

Figure A-11. Normalized PL spectra corresponding to the PLQY measurement points in Figure 2e, in logarithmic scale.

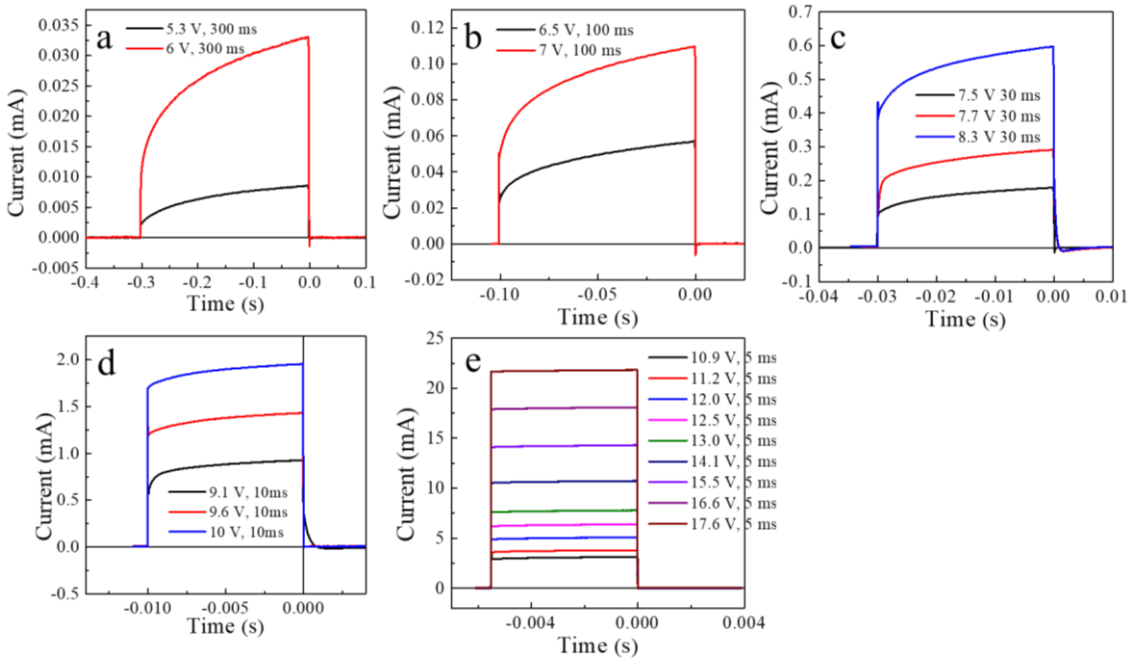

Figure A-12. Current kinetics of an n_r = 9 PeLED under the driving of the voltage pulses for calculating transient EQE. A rising of current during the pulse is observed in all the cases as the voltage increased from 5.3 to 17.6 V, which corresponds to the voltage dropping during the first decay stage in Figure 3-1a. Although the trends of current during the pulses in (e) are hard to recognize, they increase with slopes that are similar to that in (d).

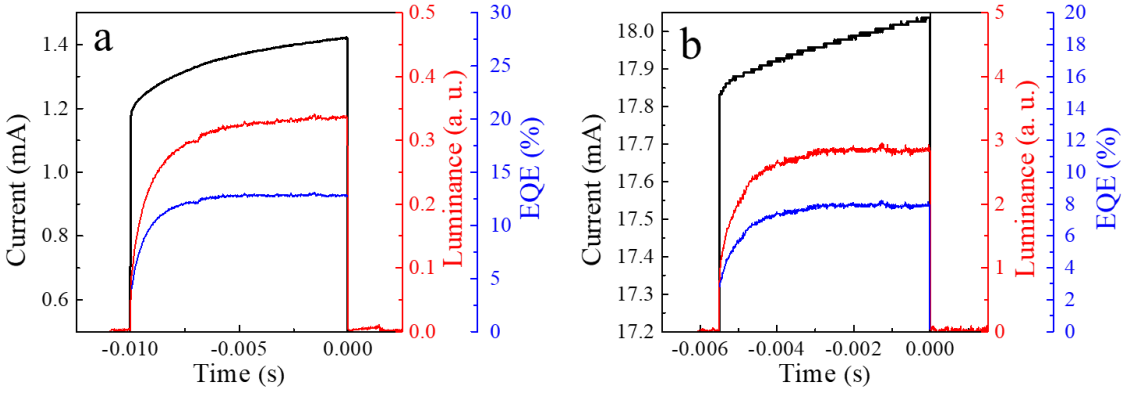

Figure A-13. Current, luminance, and EQE kinetics of an n_r = 9 PeLED during voltage pulses of (a) 9.6 V and (b) 16.6 V.

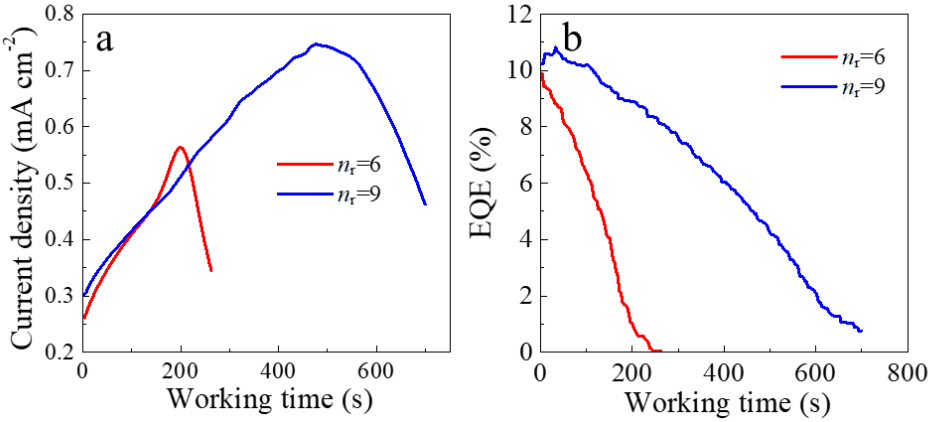

Figure A-14. Evolutions of (a) current density and (b) EQE of n_r = 6 and n_r = 9 PeLEDs under the driving of a constant voltage of 4.5 V. The raising and dropping stages of current density correspond to the dropping and raising stages of the voltage evolution under constant-current driving (Figure 1c).

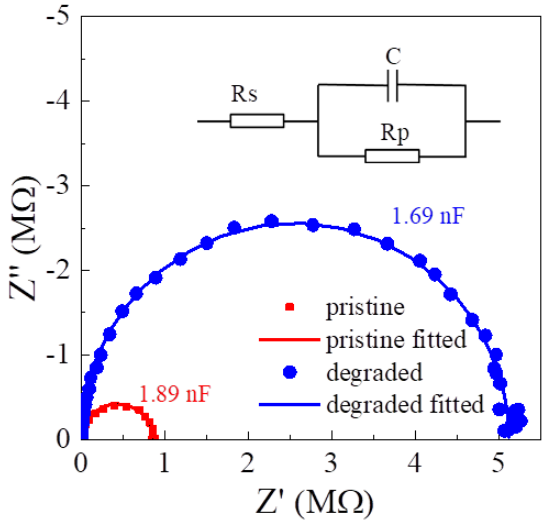

Figure A-15. AC impedance spectra of an n_r = 9 PeLED before and after the constant-current measurement. The solid curves were the fitting results with the equivalent circuit as illustrated in the inset. The calculated R_p values are displayed aside of the curves.

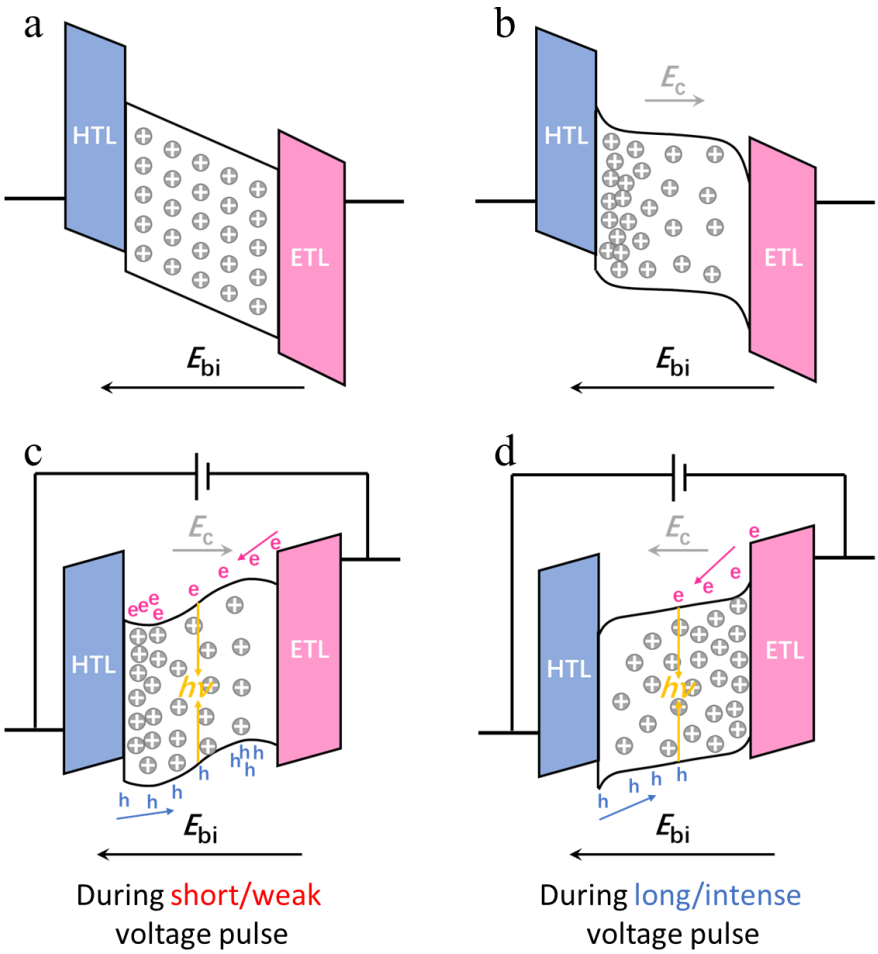

Figure A-16. Energy level diagrams of the pristine PeLED without external voltage applied when the ion migration under E_{bi} is (a) not considered or (b) considered. The diagrams of energy levels and carrier injection during the device operated under (c) a short/weak voltage pulse or (d) a long/intense voltage pulse.

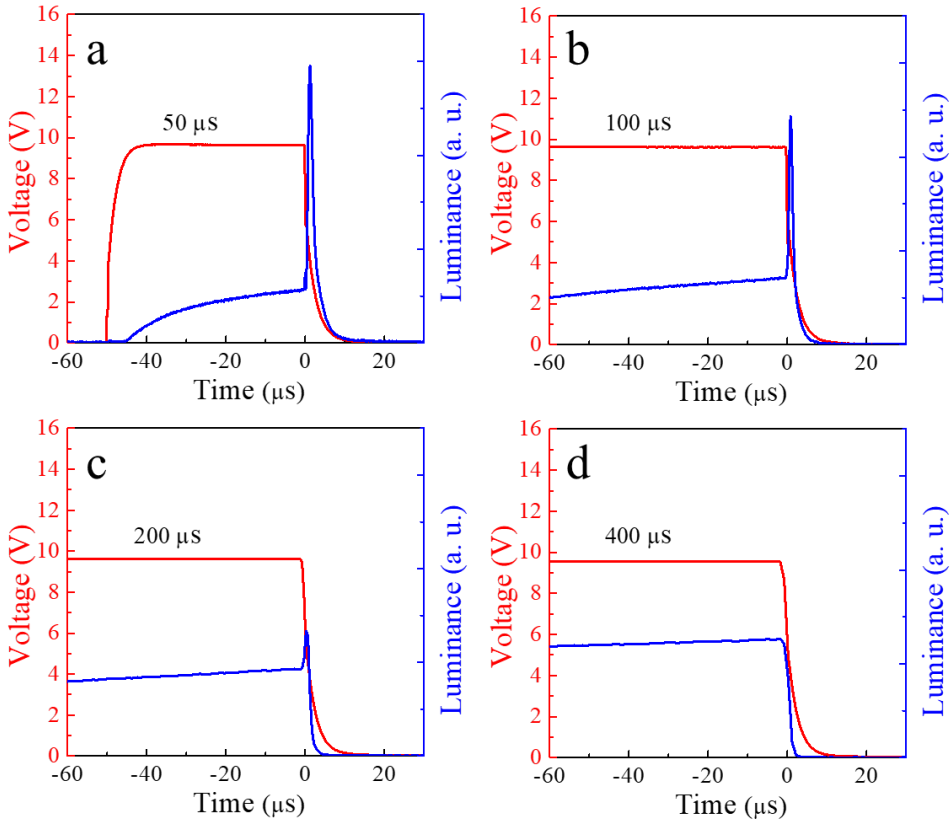

Figure A-17. Luminance evolutions of an n_r = 9 PeLED under voltage pulse durations of (a) 50 μs, (b) 100 μs. (c) 200 μs, and (d) 400 μs.

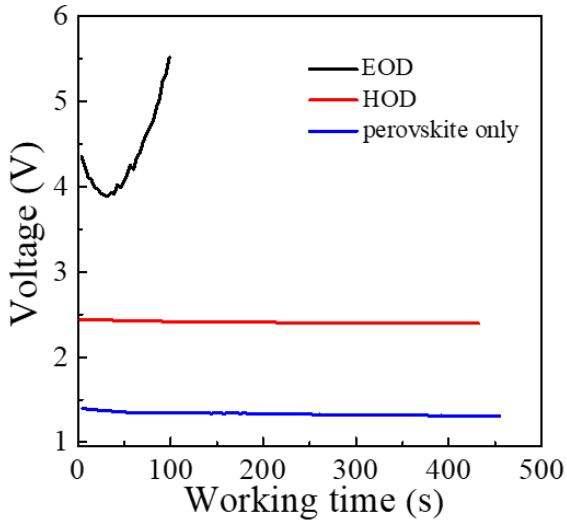

Figure A-18. Voltage evolutions of EODs, HODs and perovskite-only devices.

5.2 Appendix Tables

Table A-1. PL lifetime parameters obtained by fitting the TRPL results of ST films (Figure A-5a) with a tri-exponential decay equation.

n_r	τ_1	τ_2	τ_3	f_1	f_2	f_3
3	7.56	50	303	0.832	0.155	0.014
3.5	14.2	105	661	0.809	0.175	0.0161
4	12.5	93.2	590	0.808	0.175	0.0163
5	6.34	43.6	274	0.84	0.148	0.0117
6	6.02	39.5	229	0.849	0.141	0.0102
7	5.53	33.5	183	0.853	0.137	0.00939
8	4.65	25.4	142	0.858	0.132	0.00987

Table A-2. PL lifetime parameters obtained by fitting the TRPL results of LOD films (Figure A-5b) with a tri-exponential decay equation.

n_r	τ_1	τ_2	τ_3	f_1	f_2	f_3
3	4.65	23.9	126	0.863	0.125	0.0112
4	5.98	25.5	135	0.85	0.142	0.00769
5	9.31	38.5	227	0.773	0.218	0.00908
6	11	44.8	245	0.751	0.236	0.0131
7	9.61	39.9	203	0.769	0.218	0.0128
8	8.51	36.5	205	0.784	0.203	0.0134
9	7.35	33.2	190	0.816	0.175	0.00934
10	7.17	34.6	216	0.839	0.155	0.00619

Table A-3. ST precursor compositions used to prepare precursor solutions.

n_r	PEABr concentration (M)	FABr concentration (M)	$PbBr_2$ concentration (M)
2	0.35	0.175	0.35
3	0.233	0.233	0.35
3.5	0.2	0.25	0.35
4	0.175	0.263	0.35
5	0.14	0.28	0.35
6	0.117	0.292	0.35
7	0.1	0.3	0.35
8	0.088	0.306	0.35
9	0.078	0.311	0.35

Table A-4. LOD precursor compositions used to prepare precursor solutions.

n_r	PEABr concentration (M)	FABr concentration (M)	$PbBr_2$ concentration (M)
2	0.7	0.35	0.35
3	0.35	0.35	0.35
4	0.233	0.35	0.35
5	0.175	0.35	0.35
6	0.14	0.35	0.35
7	0.117	0.35	0.35
8	0.1	0.35	0.35
9	0.088	0.35	0.35
10	0.078	0.35	0.35

5.3 List of Abbreviations

Materials

Methylammonium (**MA**)

Formamidinium (**FA**)

Benzylammonium (**BA**)

Phenylethylammonium (**PEA**)

1-naphthylmethylamine (**NMA**)

Dimethyl sulfoxide (**DMSO**)

Indium tin oxide (**ITO**)

Poly(*N*-vinylcarbazole) (**PVK**)

1,3,5-tris(1-phenyl-1*H*-benzo[d]imidazol-2-yl)benzene (**TPBi**)

N,*N*′-di(1-naphthyl)-*N*,*N*′-diphenyl-(1,1′-biphenyl)-4,4′-diamine (**α-NPD**)

Tris(8-hydroxyquinolinato)aluminium (**Alq_3**)

Keywords

Electroluminescence (**EL**)

Light-emitting diode (**LED**)

Organic light-emitting diode (**OLED**)

Perovskite light emitting diode (**PeLED**)

External quantum efficiency (**EQE**)

Photoluminescence (**PL**)

Multi-quantum well (**MQW**)

X-ray diffraction (**XRD**)

Ruddlesden-Popper (**RP**)

Dion-Jacobson (**DJ**)

Red, green, and blue (**RGB**)

Full width at half maximum (**FWHM**)

Thermally activated delayed fluorescence (**TADF**)

Quantum-dot light-emitting diode (**QLED**)

Near infrared (**NIR**)

Stoichiometric (**ST**)

Large organic cation-doped (**LOD)**

Time-resolved photoluminescence (**TRPL**)

Electron transport layer (**ETL**)

Thermally stimulated current (**TSC**)

Hole transport layer (**HTL**)

Hole-only devices (**HOD**)

Electron-only devices (**EOD**)

Symbols

Photoluminescence quantum yield (**PLQY**)

Exciton binding energy ($\boldsymbol{E_B}$)

The lowest excited triplet state ($\mathbf{T_1}$)

Precursor recipe order ($\boldsymbol{n_r}$)

Current density versus voltage ($\boldsymbol{J-V}$)

Trap energy level depth ($\boldsymbol{E_T}$)

Trap density ($\boldsymbol{N_T}$)

Intrinsic build-in field ($\boldsymbol{E_{bi}}$)

Extra build-in field ($\boldsymbol{E_{ebi}}$)

Units

Arbitrary unit (**a. u.**)

Degree Celsius (**℃**)

Electronvolt (**eV**)

Hour (**h**)

Kelvin (**K**)

Milliliter (**mL**)

Micrometer (**μm)**

Microsecond (**μs**)

Millimeter (**mm**)

Millisecond (**ms**)

Minute (**min**)

Molar (**mol**)

Molar per liter (**M)**

Nanometer (**nm**)

Nanosecond (**ns**)

Second (**s**)

5.4 Reference

(1) Tan, Z. K.; Moghaddam, R. S.; Lai, M. L.; Docampo, P.; Higler, R.; Deschler, F., . . . Friend, R. H., *Nat. Nanotechnol.* **2014,** *9*, 687.

Achievement List

First-authored publication

1) **Tai Cheng**, Chuanjiang Qin, Satoru Watanabe, Toshinori Matsushima, and Chihaya Adachi. *Adv. Func. Mater.* **2020**, *30*(24),2001816.

"Stoichiometry Control for the Tuning of Grain Passivation and Domain Distribution in Green Quasi-2D Metal Halide Perovskite Films and Light-Emitting Diodes."

2) **Tai Cheng**, Ganbaatar Tumen-Ulzii, Dino Klotz, Satoru Watanabe, Toshinori Matsushima, and Chihaya Adachi. *ACS Appl. Mat. & Inter.* Published online. DOI: 10.1021/acsami.0c06737

"Ion Migration-Induced Degradation and Efficiency Roll-off in Quasi-2D Perovskite Light-Emitting Diodes."

Co-authored publication

1) Satoru Watanabe, **Tai Cheng**, Ganbaatar Tumen-Ulzii, Chuanjiang Qin, Toshinori Matsushima, and Chihaya Adachi. *Appl. Phys. Lett.* **2019**, *115*(23), 233502.

"Excited-State Stability of Quasi-Two-Dimensional Metal Halide Perovskite Films Under Optical and Electrical Excitations"

First-authored presentation

1) **Tai Cheng**, Satoru Watanabe, Chuanjiang Qin, Toshinori Matsushima, and Chihaya Adachi. *The 67th JSAP Spring Meeting 2020*, Sophia University, Tokyo, March 12−15, 2020

"Stoichiometry Control for the Tuning of Passivation and Phase Distribution in Green Quasi-2D Metal Halide Perovskite Films and Light-Emitting Diodes"

Acknowledgement

First of all, I would like to express my highest respect and gratitude to Professor Chihaya Adachi, who is my supervisor and the Principle Investigator of the laboratory I work in. I am always appreciative and thankful for receiving the opportunity from Professor Adachi to work for my Ph.D. degree in the Center for Organic Photonics and Electronics Research (OPERA) at Kyushu University. It was his forethoughtful decision that introduced me to the fields of perovskite optoelectronics, which is of great perspective. Also, without his patient supervising and valuable suggestions, this thesis would not be a reality.

I am also deeply grateful to Professor Katsuro Hayashi and Professor Yuji Oki for reviewing my thesis and providing helpful suggestions and critiques of high academic value on my presentation and thesis.

It is my pleasure to acknowledge Associate Professor Toshinori Matsushima for his direct guidance and participation in almost all of the research works introduced in this thesis. His detailed comments and corrections also make this thesis compete. Besides, his diligence and optimism always encourage me in my own work.

I am also grateful for Dr. Chuanjiang Qin and Professor Athula S. D. Sandanayaka for their kind supports during the early time of my doctoral carrier. Discussing with them promoted my deep consider inside this area, and their ideas helped me with determining the mainline of my doctoral research.

My co-workers, Mr. Ganbaatar Tumen-Ulzii and Mr. Satoru Watanabe participated in my research and provided me with a lot of help on accomplishing the research targets. Discussing and working with them on perovskites made my experiments more efficient and deepened my understanding of this field. Also, I would also thank Dr. Dino Klotz from the International Institute for Carbon-Neutral Energy Research (I2CNER) for his technical support, without which my proposal would lack convincing evidence.

Thanks for Associate Professor Hajime Nakanotani for arranging and assisting my study courses during the 3 years. Also, thanks to all the members of OPERA. Their abundant academic backgrounds and opinions greatly broadened my horizon. Their technical expertise and kind assistance helped me to obtain tons of experimental skills. Their responsible managing and administrating keep the laboratory run smoothly. Working and obtaining a Ph.D. degree in such a laboratory with so many sophisticated instruments and talented people is an important asset of my life. My research also involved a lot of valid results collected in I2CNER. It is a pleasant experience to cooperate with I2CNER.

Personally, I would like to thank Dr. Hao Ye, Dr. Zesen Lin, Dr. Chin-Yiu Chan, Dr. Yi-Ting Lee, Dr. Kai Wang, Dr. Yongsheng Hu, Mr. Buddhika Sanjeewa Bandara Karunathilaka, Mr. Shibin Ruan, Mr. Xun Tang, Mr. Zhao Feng, Mr. Xuelong Liu, and etc. Living and studying aboard alone is not an easy task. Their help and suggestions on all aspects helped me to solve a lot of problems.

I acknowledge the Japan Science and Technology Agency (JST), ERATO, Adachi Molecular Exciton Engineering Project for financially supporting the research work in this thesis. I also acknowledge the China Scholarship Council (CSC) for providing me with scholarship and the opportunity to study aboard.

Finally, I am especially grateful to my parents for their selfless love, understanding, and support during my doctoral period, without which I could not make it. I hope I made them proud of their son. In the meanwhile, I owe special thanks to my girlfriend, Miss Shuang Ma, or Dr. Ma in the near future. It is an extremely precious experience for a couple to study for a doctoral degree at the same time and in the same field. Although not fighting physically together, we supported each other academically and spiritually. I believe getting a doctoral degree is just the beginning of our happy ending story.